Department of Precision and Microsystems Engineering

Analysing bending-induced double curvature in metaplates

Pieter Jacob Jager

Report no : 2025.053
Coach : Dr. F. G. J. Broeren
Specialisation : Mechatronic System Design (MSD)
Type of report : Master Thesis
Date : 14 August 2025

TU Delft Delft University of Technology

Analysing bending-induced double curvature in metaplates

by

Pieter Jacob Jager

To obtain the degree of Master of Science at the Delft University of Technology.

Student number:	4861426	
Thesis committee:	Dr. M.J. Mirzaali	TU Delft, chair
	Dr. F. G. J. Broeren	TU Delft, daily supervisor
Project Duration:	June, 2024 - August, 2025	
Faculty:	Faculty of Mechanical Engineering, Delft	
Department:	Department of Precision and Microsystems Engineering	

TU Delft

abstract

Mechanical metamaterial plates (metaplates) can exhibit unique bending properties compared to regular plates. Where regular plates can only have anticlastic (saddle-shaped) or monoclastic (cylinder-shaped) bending-induced double curvature, metaplates can also have synclastic (dome-shaped) bending-induced double curvature. This behaviour can be controlled by altering the geometry of the unit-cell and has been linked to the unit-cell's Poisson's ratio. However, some metaplates exist that do not display the type of bending-induced double curvature that is expected based on their Poisson's ratio. Recent studies have shown how Cosserat or Micropolar theory can be used to more accurately describe the bending-induced double curvature of metaplates.

In this thesis metaplates are compared using different modelling approaches. The metaplates of interest are the star-shaped unit-cell and the anti-tri-chiral unit-cell. As a starting point, the metaplates are homogenised as a Cauchy continuum and through the use of additional load cases a homogenised Cosserat continuum is created. The homogenised Cosserat continuum model is compared to both the bending behaviour of the actual metaplate and the homogenised Cauchy continuum model using Finite Element Analysis. While the developed Cosserat model displays the correct type of bending-induced double curvature, the presence of deformation defects indicate that the Cosserat model requires further refinement. Additional analysis was done in COMSOL Multiphysics to explore the influence of unit-cell parameters and boundary conditions on the bending-induced double curvature of metaplates.

Summary

Mechanical metamaterial plates (metaplates) can exhibit unique bending properties compared to regular plates. Where regular plates can only have anticlastic (saddle-shaped) or monoclastic (cylinder-shaped) bending-induced double curvature, metaplates can also have synclastic (dome-shaped) bending-induced double curvature. This behaviour can be controlled by altering the geometry of the unit-cell and has been linked to the unit-cell's Poisson's ratio. However, some metaplates exist that do not display the type of bending-induced double curvature that is expected based on their Poisson's ratio. Recent studies have shown how Cosserat or Micropolar elasticity can be used to more accurately describe the bending-induced double curvature of metaplates. Using Cosserat elasticity, this inconsistency between in-plane and bending behaviour can be resolved as Poisson's ratio can be split up into two ratios, one regarding in-plane displacement and one regarding out-of-plane bending. However, no commercially available Finite Element Anlysis(FEA) programs exist that include Cosserat Elasticity. FEA programs like COMSOL multiphysics, which is used for this research, use classical or Cauchy elasticity.

In this thesis the bending-induced double curvature of metaplates is researched by comparing different modelling approaches. Two metaplate unit-cells were selected for this analysis, namely the star-shaped unit-cell and the anti-tri-chiral unit-cell. As a starting point, the metaplates were homogenised as a Cauchy continuum using six load cases. From this a homogenised Cauchy continuum model of the metaplate was made, that could be analysed with FEA. Through the use of two additional load cases the metaplate was homogenised as a Cosserat continuum for bending. The two additional load cases applied were cylindrical bending tests. However, the extra information from the additional load cases could not be inserted into a Cauchy continuum model. To analyse the homogenised Cosserat continuum model of the metaplate, the weak form in COMSOL Multiphysics was used. This made it possible to perform FEA on the homogenised Cosserat continuum model of the metaplate. Also the actual metaplate was analysed with FEA.

The bending-induced double curvatures of these three modelling approaches were compared for metaplates of both unit-cells. The type of bending-induced double curvature of the homogenised Cauchy continuum model did not match with that of the actual metaplates. The homogenised Cosserat continuum model did have the same type of bending-induced double curvature as the actual metaplates. However, the presence of deformation defects and a lack of smoothness indicate that the Cosserat model requires further refinement.

For the star-shaped unit-cell, the influence of unit-cell geometry on the bending-induced double curvature was analysed through the cylindrical bending test. The results showed similarities to existing literature regarding the star-shaped metaplate, and additionally variation of the wall thickness was incorporated. Additionally a long metaplate was analysed through FEA to visualise the influence of boundary conditions on the bending-induced double curvature. An unexpected drop in bending-induced double curvature was found for longer metaplates.

Using Cosserat elasticity to model metaplates and mechanical metamaterials in general, is a promising yet complicated method. This research shows a specific application of how Cosserat elasticity could be used in FEA. More research into applying Cosserat elasticity in FEA, could create a more complete and user friendly FEA program that can take Cosserat elasticity into account. This could lower the threshold of research using Cosserat elasticity. This would not only be useful for mechanical metamaterials, but also for a wide range of other materials or structures with significant microstructure.

Contents

Nomenclature

Abbreviations

Abbreviation	Definition
BPR	Bending Poisson's ratio
FEA	Finite Element Analysis
IPR	In-plane Poisson's ratio
MPR	Material Poisson's ratio
RVE	Representative Volume Element

Symbols

symbol	definition	unit
a	microrotation	rad
B	couple matrix entries	Pa
B	surface boundary	m^2
C	elasticity matrix entries	Pa
D	bending elasticity matrix entries	Pa
E	Young's modulus 7 Pa	
D	computational domain	m^3
D_{flex}	flexural rigidity (plate)	J
G	shear modulus	Pa
h	height	m
k	curvature	
l	length	m
M	moment	Nm
P	body forces	N
Q	body moments	Nm
u	displacement	m
V	test function	-
w	width	m
α	first Micropolar constant	N
β	second Micropolar constant	N
γ	third Micropolar constant	N
ϵ	Strain	-
ζ	Mindlin's ratio	-
θ	rotation	rad
θ_{angle}	angle in unit-cell	rad
κ_M	fourth Micropolar constant	N
κ	couple strain	rad/m
λ	first Lame constant	N
μ_L	second Lame constant	N
μ	couple stress	N/m
μ_c	couple modulus	Pa
ν	Poisson's ratio	-
ρ	density	kg/m^3
σ	stress	Pa

symbol	definition	unit
ϕ	load direction	rad
ϕ_M	microrotation, alternative notation	-
σ	stress	Pa
τ	decoupled shear stress	Pa

1

Introduction

Throughout history it can be observed that the amount of available materials for design has constantly been increasing. This allows for more design possibilities and could be critical in sectors like the high-tech industry, to improve machines further. Currently there are thousands of possible engineering materials, spanning a wide range of material properties. However, these engineering materials still have limitations. For instance, if we look at a material property like Poisson's ratio ($\nu = -\epsilon_{22}/\epsilon_{11}$), i.e. the ratio of transversal strain to axial strain, it can be observed that engineering materials almost always have Poisson's ratios between 0 and 0.5. This absence of negative Poisson's ratio materials has led to the research of auxetic structures and more specifically, mechanical metamaterials. Mechanical metamaterials are compliant structures that obtain their generalised material properties from their geometry instead of the material they are made from. Mechanical metamaterials can be designed to have a negative Poisson's ratio. Controlling Poisson's ratio has a lot of practical applications. A famous example from daily life is cork[1], which has a Poisson's ratio of roughly zero and therefore can be pushed into the neck of a wine bottle without getting wider due to the deformation from compression.

Mechanical metamaterials Can be observed at two scales. At the micro scale there is the unit-cell, made out of a material like metal or polymer. The Poisson's ratio of the material does not change. However at the macro scale, the Poisson's ratio of the mechanical metamaterial depends on the geometry of the unit-cell. Here the poisson's ratio is a generalised material property of the mechanical metamaterial. The generalised material properties of mechanical metamaterials can be obtained through homogenisation. Homogenisation is a method that be used to model a heterogeneous material as an equivalent homogeneous material. A small section of the mechanical metamaterial that is representative for the entire mechanical metamaterial, i.e. a Representative Volume Element (RVE), can be used to determine these generalised material properties. The generalised material properties obtained from the RVE can then be extrapolated to the entire material. Different types of homogenisation techniques exist, ranging from analytical models to experimental approaches. For this research it was decided to apply load cases on a RVE through FEA. This enables a single method that can be applied to a wide range of different unit-cells. Once the generalised material properties of a mechanical metamaterial are obtained, then these can be applied to a block of material in a FEA program. Now only a block of material has to analysed instead of a collection of hundreds of unit-cells.

Poisson's ratio also influences the bending behaviour of a material, specifically the bending-induced double curvature[2]. Materials with a positive Poisson's ratio display anticlastic bending-induced double curvature. Poisson's ratio can be described for bending as the ratio of transversal curvature to axial curvature i.e. $BPR = -k_{21}/k_{12}$. Where an initial curvature is applied to k_12 and k_21 is the double curvature induced by curvature k_12.. This behaviour is of particular interest when regarding plates as the out-of-plane bending stiffness is relatively low and plate theory could be applied. Mechanical metamaterial plates (metaplates) can be designed to display anticlastic, monoclastic or synclastic curvature[2][3][4][5][6][7]. Controlling bending-induced double curvature could be applied to get complex spatial geometries from initially flat structures[2]. In the research field of energy harvesting, connecting the piezo-electric elements to a metaplate that bends synclastically can improve the performance

of the energy harvester. More strain is applied to the piezo-electric element for the same amount of axial curvature, compared to the situation where the piezo-electric element was connected to a regular plate[8][9][10].

Soest presented how varying Poisson's ratio in metaplates could be used to obtain complexly curved metaplates[11]. In this research it was assumed that metaplates could be represented as (Cauchy) Love-Kirchhoff plates. However, other research indicates that Poisson's ratio does not determine the bending-induced double curvature of metaplates[5][12][13]. Recent literature has shown that the bending-induced double curvature of metaplates depends on more than just Poisson's ratio[7][14][15]. During bending, the beams or flexures comprising the unit-cell of the metaplate experience both bending and torsion. The interaction between bending and torsion depends on the geometry of the unit-cell, which means that representing a metaplate as a Cauchy continiuum has shortcomings and will not always lead to accurate results[15].

Extensions to the Cauchy continuum are couple stress theory and the Cosserat or Micropolar continuum. Both Cosserat and Micropolar can be used to describe a continuum that has three additional degrees of freedom in the form of microrotations, compared to the three translational degrees of freedom of a Cauchy continuum. For this research it was chosen to use the term Cosserat. Through the use of Cosserat theory, Poisson's ratio can be split up into the in-plane Poisson's ratio (IPR) and the Bending Poisson Ratio (BPR)[15][14]. The BPR can be used to design metaplates with complex double curvature, even for a constant IPR[14]. Based on findings from literature, for (auxetic) honeycomb metaplates the IPR is often close to the desired bending-induced double curvature[2][3][4]. This could be due to the fact that the BPR of these unit-cells quickly converge to the IPR[14]. However, it is still useful to also check the BPR, to make sure the assumption $IPR = BPR$ is valid. For other unit-cells the BPR should be considered instead of the IPR to determine the desired bending-induced double curvature.

Through the use of Cosserat theory, the possible convergence of BPR to IPR could be analysed for different unit-cells. This could be valuable for the application of metaplates in engineering purposes, as around the region of convergence the metaplate could be modelled like a Cauchy plate, which would significantly reduce the complexity of the model and conventional homogenisation techniques would be applicable. It is hypothesised by Eskandari et al. that for all metaplates the BPR will eventually converge to the IPR as the relative thickness, which can be seen as a size dependency, becomes greater[14]. However, from the research of Eskandari et al. this could only be concluded for the (auxetic) honeycomb unit-cells[14].

Cosserat theory is not only applicable to metaplates, but has a wide variety of applications for materials/structures containing a significant microstructure[16][17]. Rezaei et al. presented how Cosserat theory can be used to more accurately model perforated plates and bone, for dentistry applications[18][19]. Masiani et al. presented how Cosserat theory can be applied to the modelling of brick walls[20]. For all these applications a more standardised modelling method would be beneficial. As of the time of writing, a homogenisation application in COMSOL exists that is able to homogenise a heterogeneous medium as a Cauchy continuum, but not as a Cosserat continuum. As of the time of writing, there are no commercial Finite Element Analysis) FEA programs available that include Cosserat theory. This was also stated by Rezaei et al. in 2024[18]. In COMSOL Multiphysics the weak form can be used to model a Cosserat continuum. Jeong et al. modelled torsion in a Cosserat rod[21], which Rezaei et al. did as well[18]. Additionally, Rezaei et al. made a two Dimensional Cosserat model for concentrated loads and shear loads[18][19]. Using the weak form in COMSOL Multiphysics to model bending-induced double curvature for a Cosserat continuum has not been found in literature.

In this thesis a method is presented to create a Cosserat continuum model for the bending of metaplates, using the weak form in COMSOL Multiphysics. While, research has been done to apply Cosserat elasticity to the weak form in COMSOL Multiphysics, this has only been done to model torsion in a cylinder[21][18] and deformation in a 2D plate[18][19]. Modelling bending-induced double curvature is a novel application of using the weak form in COMSOL Multiphysics. This method will be applied to two metaplates, namely one with a star-shaped unit-cell and one with an anti-tri-chiral unit-cell. As a starting point, the metaplates are homogenised as a Cauchy continuum and through the use of additional load cases a homogenised Cosserat continuum is created. Validation is performed by analysing different mesh sizes and different RVE's. The homogenised Cosserat continuum model is compared

to both the bending behaviour of the actual metaplate and the homogenised Cauchy continuum model through FEA. While the developed Cosserat model displays the correct type of bending-induced double curvature, the presence of deformation defects indicate that the Cosserat model requires further refinement. Additionally, the influence of unit-cell geometry on the BPR is analysed, which could provide novel insights into the required modelling approach. Also possibilities for experimental testing are explored through a FEA of the bending-induced double curvature for an increasingly long metaplate.

2

Methodology

The methodology is divided into four major sections. First, the unit-cells of interest for this research are introduced and Representative Volume Elements (RVE's) for these unit-cells are chosen. Second, the metaplate is modelled as a Cauchy continuum through homogenisation and a Cauchy continuum model is setup. Third, the metaplate is modelled as a Cosserat continuum and a Cosserat continuum model is set up. Fourth, validation of the parts of the methodology is performed and additional validation models are setup. From the methodology three metaplate models are made, a detailed metaplate consisting out of tesselated unit-cells, a homogenised Cauchy continuum model and a homogenised Cosserat continuum model. These models can be compared to evaluate how the modelling method influences the observed bending-induced double curvature.

2.1. Unit-cells and RVE

A representative Volume Element (RVE) is a small section of the structure, that is representative for the entire structure. This is similar to how unit-cells can be tesselated to create the metamaterial. The unit-cell is an often used as the RVE. However, if there are planes of symmetry in the unit-cell it is possible to reduce the RVE to a section of the unit-cell, where that section can create the entire unit-cell via mirroring operations. This has been done for honeycombs[22][23]. Reducing the size of the RVE is desirable as the analysis will require less computation power. However, there is a risk that if the RVE is too small, that information about the global behaviour is lost. For this research two different RVE's were selected for each unit-cell, to evaluate if the size of the RVE influences the behaviour. If the behaviour of the smaller RVE does not significantly differ from the larger RVE, it can be validated that the smaller RVE is an effective choice of RVE.

The first unit-cell of interest is the star-shaped unit-cell, which can be seen in Figure 2.1. This unit-cell is present in two recent studies that investigated the BPR of this unit-cell[15][14]. In this research it was shown that the star-shaped unit-cell can have a positive IPR, while having a negative BPR. The star-shaped unit-cell has a tetragonal crystal class and belongs to the $4/mmm$ symmetry group[14]. Four mirror planes are present in the unit-cell. The first RVE was chosen as the unit-cell itself, while for the alternative RVE a section of three by three unit-cells was chosen. The alternative RVE can be seen in Figure 2.1. For the star-shaped unit-cell the relevant geometry and material parameters are given in Table 2.1a.

The second unit-cell of interest is the anti-tri-chiral unit-cell, which can be seen in Figure 2.2. In a study about multiple chiral and anti-chiral metaplates, the anticlastic bending-induced double curvature of this unit-cell was unexpected as it has a negative IPR[5]. The anti-tri-chiral unit-cell is a hexagonal unit-cell like the honeycomb unit-cell, meaning that every unit-cell connects to six other unit-cells. However, the anti-tri-chiral unit-cell has a trigonal crystal class and belongs to the $3m$ symmetry group. Three mirror planes are present in the unit-cell, where every symmetry element is a small tri-chiral structure. The anti-tri-chiral unit-cell can be converted into a orthorhombic unit-cell by adding or removing a section of the unit-cell. These two variants were chosen as the two RVE's, which can be seen in Figure 2.2. For

the anti-tri-chiral unit-cell the relevant geometry and material parameters are given in Table 2.1b.

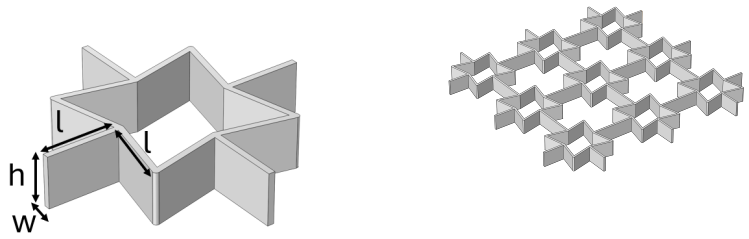

Figure 2.1: star-shaped unit-cell and alternative RVE

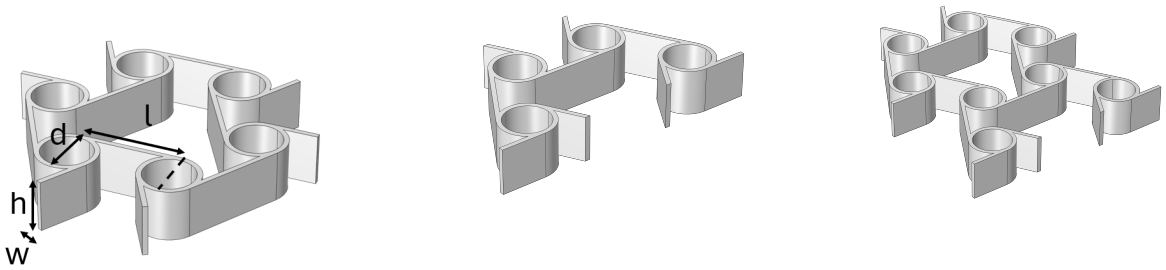

(a) Unit-cell **(b)** RVE **(c)** Alternative RVE

Figure 2.2: Anti-tri-chiral unit-cell and RVE's

Length flexure	$l = 6mm$
Height flexure	$h = 4mm$
Width flexure	$w = 0.5mm$
Angle between flexures	$\theta_{angle} = 77°$
Young's modulus	$E_{nylon} = 2GPa$
Material Poisson's ratio	$\nu_{nylon} = 0.4$

(a) Relevant parameters of star-shaped unit-cell

Length flexure	$l = 10mm$
Height flexure	$h = 5mm$
Cylinder diameter	$h = 5mm$
Width flexure	$w = 0.5mm$
Angle between flexures	$\theta_{angle} = 120°$
Young's modulus	$E_{nylon} = 2GPa$
Material Poisson's ratio	$\nu_{nylon} = 0.4$

(b) Relevant parameters of anti-tri-chiral unit-cell

Table 2.1: Unit-cell parameters

2.2. Cauchy model

2.2.1. Cauchy continuum

In an isotropic Cauchy continuum only two elastic constants are required to model the behaviour of the continuum. This means that the elasticity tensor can be constructed from these two parameters, for instance the Young's modulus and Poisson's ratio. Other parameters are also possible, namely: [Bulk modulus and shear modulus], [the lamé parameters] and [pressure wave speed and shear wave speed]. These parameters can be expressed as function of the other parameters. For instance, the shear modulus can be written as a function of the Young's modulus and Poisson's ratio:

$$G = \frac{E}{2(1+\nu)} \tag{2.1}$$

If the continuum is anisotropic, then additional parameters are required to model the behaviour, as one material parameter can have different values depending on the direction along which it is measured. If the material is transversely isotropic i.e. isotropic in-plane, then an additional Young's modulus, Poisson's ratio and an independent shear modulus are required, as the shear modulus perpendicular to the plane of isotropy can no longer be calculated using Equation 2.1. So five material parameters are required in this case[24]. If the continuum is orthotropic i.e. different in three orthogonal directions, then nine material parameters are required. Here we need three Young's moduli, three Poisson's ratios and three shear moduli[24]. In the book "Theory of Plates and Shells" by Mittelstedt[24] a general introduction is given into material symmetries, which can be looked at for further information. For the purpose of this research a few relevant material symmetries and simplifications for plate theory are presented starting from the fully anisotropic case.

For a fully anisotropic Cauchy continuum, there are 21 elastic constants that have to be determined. For a fully anisotropic material Hooke's law states:

$$\begin{pmatrix}\sigma_{11}\\ \sigma_{22}\\ \sigma_{33}\\ \sigma_{23}\\ \sigma_{13}\\ \sigma_{12}\end{pmatrix} = \begin{bmatrix}C_{11} & C_{12} & C_{13} & C_{14} & C_{15} & C_{16}\\ C_{12} & C_{22} & C_{23} & C_{24} & C_{25} & C_{26}\\ C_{13} & C_{23} & C_{33} & C_{34} & C_{35} & C_{36}\\ C_{14} & C_{24} & C_{34} & C_{44} & C_{45} & C_{46}\\ C_{15} & C_{25} & C_{35} & C_{45} & C_{55} & C_{56}\\ C_{16} & C_{26} & C_{36} & C_{46} & C_{56} & C_{66}\end{bmatrix} \begin{pmatrix}\epsilon_{11}\\ \epsilon_{22}\\ \epsilon_{33}\\ 2\epsilon_{23}\\ 2\epsilon_{13}\\ 2\epsilon_{12}\end{pmatrix} \tag{2.2}$$

The C_{ij} components in the stiffness matrix still relate to the previously mentioned material properties. Terms C_{11}, C_{22} and C_{33} contain Young's moduli, C_{44}, C_{55} and C_{66} are shear moduli and the off-diagonal terms are coupling terms between these. For instance, the terms C_{12}, C_{13} and C_{23} couple the principal strains via Poisson's ratio. If the the material is orthotropic, Equation 2.2 reduces to Equation 2.3. For achiral and anti-chiral unit-cells, no couplings between principal stains and shear stresses are expected.

$$\begin{pmatrix}\sigma_{11}\\ \sigma_{22}\\ \sigma_{33}\\ \sigma_{23}\\ \sigma_{13}\\ \sigma_{12}\end{pmatrix} = \begin{bmatrix}C_{11} & C_{12} & C_{13} & 0 & 0 & 0\\ C_{12} & C_{22} & C_{23} & 0 & 0 & 0\\ C_{13} & C_{23} & C_{33} & 0 & 0 & 0\\ 0 & 0 & 0 & C_{44} & 0 & 0\\ 0 & 0 & 0 & 0 & C_{55} & 0\\ 0 & 0 & 0 & 0 & 0 & C_{66}\end{bmatrix} \begin{pmatrix}\epsilon_{11}\\ \epsilon_{22}\\ \epsilon_{33}\\ 2\epsilon_{23}\\ 2\epsilon_{13}\\ 2\epsilon_{12}\end{pmatrix} \tag{2.3}$$

Because plates are of interest, where the height is a lot smaller than the length and width, not all terms are of interest. Two well established plate theories are Love-Kirchhoff and Reissner-Mindlin. Based on which of these plate theories are used, simplifications can be made that reduce the size of the stiffness matrix. Assumptions of Love-Kirchhoff plate theory are that the top and bottom plane remain equally far apart, the stress σ_{33} should be negligable[25][24]. Also the shear strain components ϵ_{23} and ϵ_{13} are not part of the constituitive equations[25][24].

$$\begin{pmatrix}\sigma_{11}\\ \sigma_{22}\\ \sigma_{12}\end{pmatrix} = \begin{bmatrix}C_{11} & C_{12} & C_{16}\\ C_{12} & C_{22} & C_{26}\\ C_{16} & C_{36} & C_{66}\end{bmatrix} \begin{pmatrix}\epsilon_{11}\\ \epsilon_{22}\\ 2\epsilon_{12}\end{pmatrix} \tag{2.4}$$

Again, if the unit-cell of interest is achiral or anti-chiral, then no couplings between prinicipal strains and shear tresses are expected, which results in:

$$\begin{pmatrix}\sigma_{11}\\ \sigma_{22}\\ \sigma_{12}\end{pmatrix} = \begin{bmatrix}C_{11} & C_{12} & 0\\ C_{12} & C_{22} & 0\\ 0 & 0 & C_{66}\end{bmatrix} \begin{pmatrix}\epsilon_{11}\\ \epsilon_{22}\\ 2\epsilon_{12}\end{pmatrix} \tag{2.5}$$

This can be further simplified based on the symmetries in the unit-cell. The anti-tri-chiral unit-cell is expected to look like Equation 2.5. The star shaped unit-cell has four-fold rotational symmetry, which

can be seen in Figure 2.1. Due to this additional symmetry, the axial responses are identical for both in-plane directions, so $C_{22} = C_{11}$.

In a Cauchy continuum, the bending and torsion response can be determined using the elastic constants from Hooke's law and the thickness. This means that measuring the bending or torsion response is not required to characterise a Cauchy continuum. For an isotropic plate the bending behaviour is as presented by Timoshenko and Woinowsky-Krieger[25]:

$$\begin{pmatrix} M_x \\ M_y \\ M_{xy} \end{pmatrix} = \begin{bmatrix} D & \nu D & 0 \\ \nu D & D & 0 \\ 0 & 0 & D(1-\nu) \end{bmatrix} \begin{pmatrix} k_x \\ k_y \\ k_{xy} \end{pmatrix} \tag{2.6}$$

where k_x and k_y represent curvatures, k_{xy} represents twist and M_{xy} represents torsion. D is the flexural rigidity and ν is Poisson's ratio. For Reissner-Mindlin plates, out of plane shear forces also have to be considered[25].

2.2.2. Cauchy homogenisation

To obtain the elastic constant of the elasticity tensor, load cases can be used. A load case is a specific loading condition that can be applied to obtain information about the material or structure. For instance, a load case to obtain the axial elastic constant C_{11} is to apply a principal strain in the x-direction and evaluating the resulting stress in the x-direction. These load cases can be applied to the RVE.

To determine the elasticity tensors, COMSOL Multiphysics was used. Specifically, the cell-periodicity feature, in which a Respective Volume Element (RVE) can be analysed to obtain the elasticity tensor. In COMSOL Multiphysics, periodic boundary conditions are handled through so called source and destination planes, where these planes are fixed in alignment. For an orthotropic RVE in 3D, six load cases are applied, namely three in tension and three in pure shear. These load cases are visualised in Figure 2.3. The source and destination planes have to be manually applied, but from this COMSOL returns the homogenised elasticity tensor. With the cell-periodicity feature it is not possible to use a reduced RVE based on symmetry, as both the source and destination plane have to applied to the RVE. To validate the accuracy of the homogenisation procedure, mesh convergence was tested by using two different mesh sizes. Also as mentioned previously, two different RVE sizes were used.

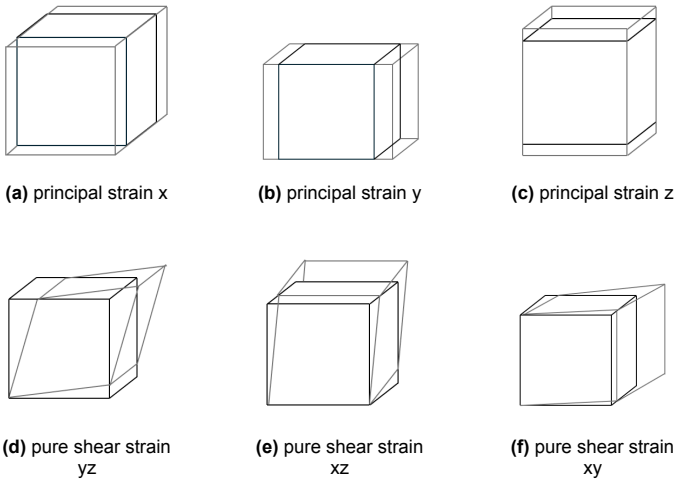

(a) principal strain x **(b)** principal strain y **(c)** principal strain z

(d) pure shear strain yz **(e)** pure shear strain xz **(f)** pure shear strain xy

Figure 2.3: six load cases

To evaluate the bending-induced double curvature of the homogenised Cauchy continuum model, the homogenised Cauchy elasticity tensor was inserted as the material into a rectangular block in COMSOL Multiphysics. The rectangular block contains the homogenised Cauchy properties of the metaplate. Pure bending along two opposing sides was applied. Due to symmetry of the loading condition, only a quarter of the rectangular block had to be modelled. In Figure 2.4 it can be seen how mirroring the block

outlined in red can form the entire rectangular block. In Figure 2.5 the modelled part of the rectangular block can be seen. At boundaries one and three symmetry planes are applied. A fixed constraint is applied to edge two and the moment is applied at boundary four.

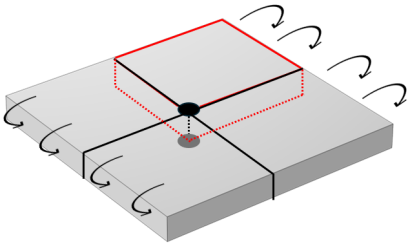

Figure 2.4: Pure bending applied to rectangular block, red section is modelled

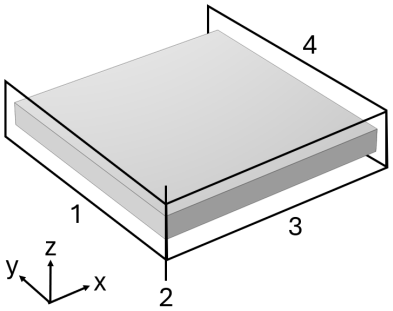

Figure 2.5: modelled part of the rectangular block, with relevant boundary planes and edges numbered

2.3. Cosserat model

2.3.1. Cosserat continuum

An extension to the previously mentioned Cauchy continuum is the Cosserat or Micropolar continuum. In an isotropic Cosserat continuum six elastic constants are required, namely: λ, μ, κ, γ, β and α. The term couple-stress theory is also closely related, with the difference being that couple-stress theory has four elastic constants, namely: λ, μ, γ and β[17]. Here it can be seen that Cosserat theory can be reduced to couple-stress theory and even to Cauchy theory, where only λ and μ remain[17]. In a Cosserat continuum couple stresses are introduced in addition to the stresses present in a Cauchy continuum. The stresses in a Cauchy continuum and the stresses and couple stresses present in a Cosserat continuum can be seen in Figure 2.6 and Figure 2.7 respectively.

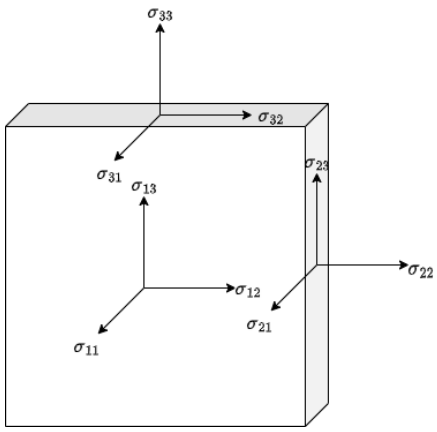

Figure 2.6: Stresses in Cauchy continuum

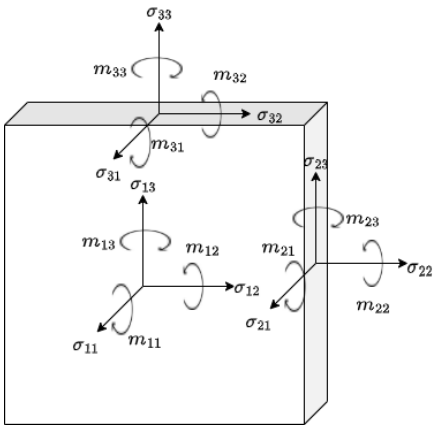

Figure 2.7: stresses and couple stress in Cosserat continuum

As mentioned previously, a Cauchy continuum has three translational degrees of freedom, which can be denoted as the vector **u**. A Cosserat continuum has three additional microrotational degrees of freedom, which can be denoted as the vector **a**. To visualise how these degrees of freedom are used Figure 2.8 was made. In the top of Figure 2.8 u and a can be found. The contents of Figure 2.8 will be further explained in this section. In a Cauchy Continuum the strain is the gradient of **u**. Due to the microrotations the strain in a Cosserat continuum becomes

$$\epsilon_{ij} = \frac{\partial u_j}{\partial x_i} - e_{ijk} a_k \tag{2.7}$$

where e_{ijk} is the permutation tensor. The permutation tensor turns the microrotations into a skew symmetric tensor, which means that for the principal strains there is no microrotation component.

In a Cosserat continuum there is also couple strain, which depends on the microrotations. The couple strain is

$$\kappa_{ij} = \frac{\partial a_j}{\partial x_i} \tag{2.8}$$

where axial couple strains represent torsion and off-diagonal couple strains represent bending. The constitutive equations for a Cosserat continuum are

$$\begin{aligned} \sigma_{ij} &= C_{ijkl}\epsilon_{kl} + B_{ijkl}\kappa_{kl} \\ m_{ij} &= B_{klij}\epsilon_{kl} + D_{ijkl}\kappa_{kl} \end{aligned} \tag{2.9}$$

where σ_{ij} is the asymmetric stress tensor, m_{ij} is the couple stress tensor. **C**, **B** and **D** are elasticity tensors, where **B** couples strain to couple stress and couple strain to stress. For the scope of this research only centrosymmetric unit-cells are of interest, so B is assumed to be zero[14]. This means that the stress only depends on the strain and the couple stress only depends on the couple strain. In Figure 2.8, the relation between (couple) stress and (couple) strain are displayed, linked by the corresponding elasticity tensor. The couplings due to **B** are displayed as striped blue lines. The constitutive equations from Equation 2.9 can be alternatively written as:

$$\begin{pmatrix} \sigma_{11} \\ \sigma_{22} \\ \sigma_{33} \\ \sigma_{23} \\ \sigma_{13} \\ \sigma_{12} \\ \sigma_{32} \\ \sigma_{31} \\ \sigma_{21} \end{pmatrix} = \begin{bmatrix} C_{11} & C_{12} & C_{13} & C_{14} & C_{15} & C_{16} & C_{17} & C_{18} & C_{19} \\ & C_{22} & C_{23} & C_{24} & C_{25} & C_{26} & C_{27} & C_{28} & C_{29} \\ & & C_{33} & C_{34} & C_{35} & C_{36} & C_{37} & C_{38} & C_{39} \\ & & & C_{44} & C_{45} & C_{46} & C_{47} & C_{48} & C_{49} \\ & & & & C_{55} & C_{56} & C_{57} & C_{58} & C_{59} \\ & & & & & C_{66} & C_{67} & C_{68} & C_{69} \\ & & sym & & & & C_{77} & C_{78} & C_{79} \\ & & & & & & & C_{88} & C_{89} \\ & & & & & & & & C_{99} \end{bmatrix} \begin{pmatrix} \epsilon_{11} \\ \epsilon_{22} \\ \epsilon_{33} \\ \epsilon_{23} \\ \epsilon_{13} \\ \epsilon_{12} \\ \epsilon_{32} \\ \epsilon_{31} \\ \epsilon_{21} \end{pmatrix} \tag{2.10}$$

$$\begin{pmatrix} m_{11} \\ m_{22} \\ m_{33} \\ m_{23} \\ m_{13} \\ m_{12} \\ m_{32} \\ m_{31} \\ m_{21} \end{pmatrix} = \begin{bmatrix} D_{11} & D_{12} & D_{13} & D_{14} & D_{15} & D_{16} & D_{17} & D_{18} & D_{19} \\ & D_{22} & D_{23} & D_{24} & D_{25} & D_{26} & D_{27} & D_{28} & D_{29} \\ & & D_{33} & D_{34} & D_{35} & D_{36} & D_{37} & D_{38} & D_{39} \\ & & & D_{44} & D_{45} & D_{46} & D_{47} & D_{48} & D_{49} \\ & & & & D_{55} & D_{56} & D_{57} & D_{58} & D_{59} \\ & & & & & D_{66} & D_{67} & D_{68} & D_{69} \\ & & sym & & & & D_{77} & D_{78} & D_{79} \\ & & & & & & & D_{88} & D_{89} \\ & & & & & & & & D_{99} \end{bmatrix} \begin{pmatrix} \kappa_{11} \\ \kappa_{22} \\ \kappa_{33} \\ \kappa_{23} \\ \kappa_{13} \\ \kappa_{12} \\ \kappa_{32} \\ \kappa_{31} \\ \kappa_{21} \end{pmatrix} \tag{2.11}$$

where there are nine stresses and nine strains, as the stress and strain tensor are no longer symmetric, which was the case for a Cauchy continuum. For this research the interest lies in achiral and anti-chiral unit-cells. It is assumed there are no axial-shear couplings. Also it is also assumed that there are no torsion-bending couplings.The constitutive equations then become:

$$\begin{pmatrix}\sigma_{11}\\ \sigma_{22}\\ \sigma_{33}\\ \sigma_{23}\\ \sigma_{13}\\ \sigma_{12}\\ \sigma_{32}\\ \sigma_{31}\\ \sigma_{21}\end{pmatrix} = \begin{bmatrix} C_{11} & C_{12} & C_{13} & 0 & 0 & 0 & 0 & 0 & 0 \\ & C_{22} & C_{23} & 0 & 0 & 0 & 0 & 0 & 0 \\ & & C_{33} & 0 & 0 & 0 & 0 & 0 & 0 \\ & & & C_{44} & 0 & 0 & C_{47} & 0 & 0 \\ & & & & C_{55} & 0 & 0 & C_{58} & 0 \\ & & & & & C_{66} & 0 & 0 & C_{69} \\ & & sym & & & & C_{77} & 0 & 0 \\ & & & & & & & C_{88} & 0 \\ & & & & & & & & C_{99} \end{bmatrix} \begin{pmatrix}\epsilon_{11}\\ \epsilon_{22}\\ \epsilon_{33}\\ \epsilon_{23}\\ \epsilon_{13}\\ \epsilon_{12}\\ \epsilon_{32}\\ \epsilon_{31}\\ \epsilon_{21}\end{pmatrix} \tag{2.12}$$

$$\begin{pmatrix}m_{11}\\ m_{22}\\ m_{33}\\ m_{23}\\ m_{13}\\ m_{12}\\ m_{32}\\ m_{31}\\ m_{21}\end{pmatrix} = \begin{bmatrix} D_{11} & D_{12} & D_{13} & 0 & 0 & 0 & 0 & 0 & 0 \\ & D_{22} & D_{23} & 0 & 0 & 0 & 0 & 0 & 0 \\ & & D_{33} & 0 & 0 & 0 & 0 & 0 & 0 \\ & & & D_{44} & 0 & 0 & D_{47} & 0 & 0 \\ & & & & D_{55} & 0 & 0 & D_{58} & 0 \\ & & & & & D_{66} & 0 & 0 & D_{69} \\ & & sym & & & & D_{77} & 0 & 0 \\ & & & & & & & D_{88} & 0 \\ & & & & & & & & D_{99} \end{bmatrix} \begin{pmatrix}\kappa_{11}\\ \kappa_{22}\\ \kappa_{33}\\ \kappa_{23}\\ \kappa_{13}\\ \kappa_{12}\\ \kappa_{32}\\ \kappa_{31}\\ \kappa_{21}\end{pmatrix} \tag{2.13}$$

For the application of Cosserat theory on plates, the constitutive equations can be further simplified. The constitutive equations for Love-Kirchhoff plates become:

$$\begin{pmatrix}\sigma_{11}\\ \sigma_{22}\\ \sigma_{12}\\ \sigma_{21}\end{pmatrix} = \begin{bmatrix} C_{11} & C_{12} & 0 & 0 \\ & C_{22} & 0 & 0 \\ & & C_{66} & C_{69} \\ & sym & & C_{99} \end{bmatrix} \begin{pmatrix}\epsilon_{11}\\ \epsilon_{22}\\ \epsilon_{12}\\ \epsilon_{21}\end{pmatrix} \tag{2.14}$$

$$\begin{pmatrix}m_{11}\\ m_{22}\\ m_{12}\\ m_{21}\end{pmatrix} = \begin{bmatrix} D_{11} & D_{12} & 0 & 0 \\ & D_{22} & 0 & 0 \\ & & D_{66} & D_{69} \\ & sym & & D_{99} \end{bmatrix} \begin{pmatrix}\kappa_{11}\\ \kappa_{22}\\ \kappa_{12}\\ \kappa_{21}\end{pmatrix} \tag{2.15}$$

where the relevant stresses are identical to a Cosserat continuum in 2D, as presented by Cui et al.[26]. For the couple stresses, torsional couple stresses and out-of-plane bending couple stresses are of interest[15]. The in-plane bending couple stresses, which are a part of the constitutive equations in 2d can be disregarded for Love-Kirchoff plate theory[14]. Due to time constraints, the Cosserat continuum model has not been converted to be applicable on thin plates.

In the research by Jeong et al. macrorotations were computed from **u**, which can also be turned into a skew symmetric tensor using the permutation tensor[21]. This allows for the decoupling of the shear stress into a Cauchy symmetric shear stress and a Cosserat shear stress, which is similar to the decoupling described by Cui et al.[26][27]. In the research by Jeong et al. this decoupling was done through using the couple modulus μ_c. This made it possible to utilise a seperate Cauchy stess tensor and have an addition for the Cosserat part. The resulting formula for the asymmetric stress tensor becomes[21]:

$$\sigma_{Cosserat} = \sigma_{Cauchy} + 2\mu_c(e_{jik}w_k - e_{jik}a_k) \tag{2.16}$$

where the permutation tensors are transposed compared to Equation 2.7. As the couple modulus becomes increasingly small, the stress tensor reduces to the Cauchy stress tensor. For this research the couple modulus of the unit-cells of interest were not determined, so Equation 2.9 was used instead. However, in future research where the couple modulus is known, this could be a promising approach. In Figure 2.8 the potential usage of macrorotations to determine the off-diagonal strain components is indicated by a striped line.

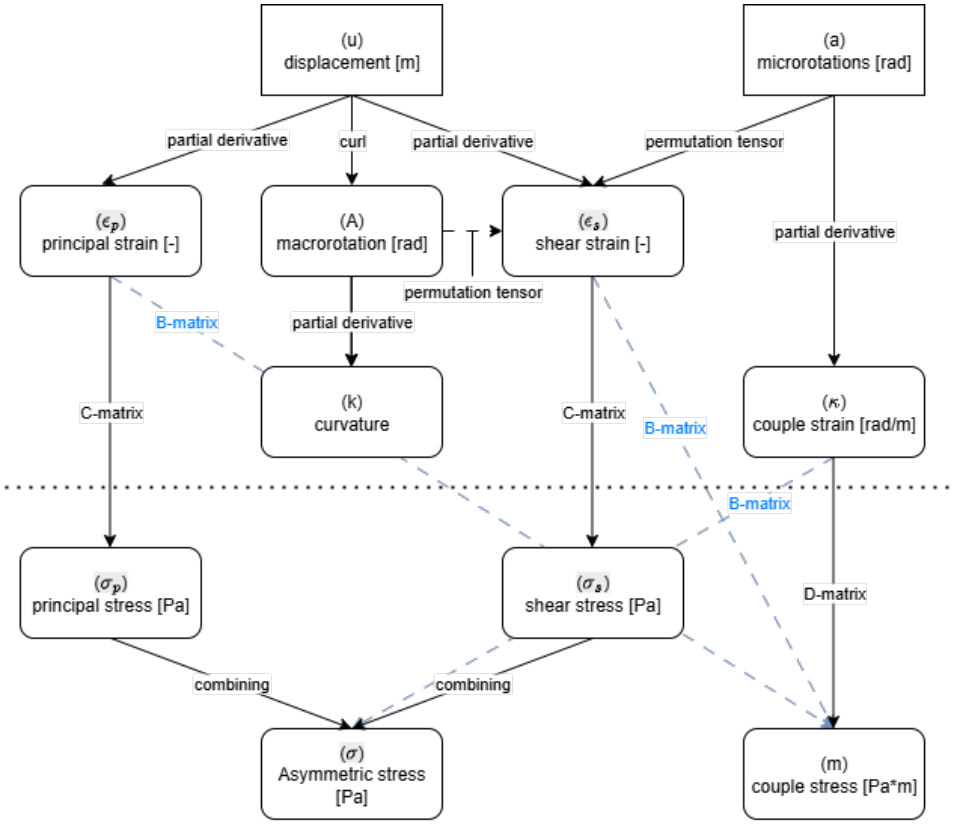

Figure 2.8: visualisation of how the global variables (translations and microrotations) are related to the derived variables

2.3.2. Additional load cases

In addition to the axial and shear load cases used for Cauchy, additional shear, torsion and bending load cases are required to completely characterise a Cosserat continuum. Also more load cases could be required if additional couplings due to chirality are present. This would require extensive testing and validation. For the scope of this research the interest lies in the bending-induced double curvature, which relates to the bending-bending coupling. Therefore it was decided to focus on two additional load cases to observe the out-of-plane bending in both principal directions. From Equation 2.13 these are:

$$\begin{aligned} m_{12} &= D_{66}\kappa_{12} + D_{69}\kappa_{21} \\ m_{21} &= D_{69}\kappa_{12} + D_{99}\kappa_{21} \end{aligned} \tag{2.17}$$

where D_{99} is equal to D_{99} in the case of the star-shaped unit-cell due to its symmetry. This is not the case for the anti-tri-chiral unit-cell.

A commonly used principle for the bending of plates is cylindrical bending, which can be seen in Figure 2.9. This is a case of pure bending where two opposing moments bend the plate and two perpendicular moments are used to obtain zero double curvature i.e. cylindrical bending. This method can be found in books about plate theory[25] and was also proposed by Gauthier et al. as a method to obtain Cosserat elastic constants[28]. The cylindrical bending test was selected as the method of the additional load cases. The same RVE that the Cauchy load cases were applied to can be used for these additional load cases.

To obtain the BPR from this test, two opposing bending moments M_x were applied and the reaction moments M_y that kept the plate cylindrical were evaluated. Gauthier et al.[28] proposed the following formula for this:

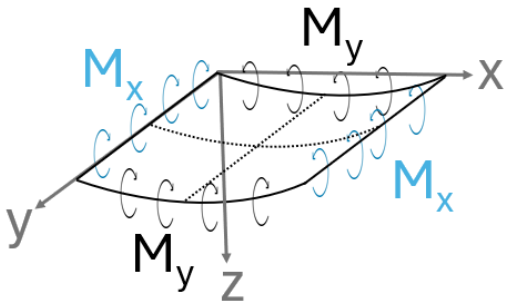

Figure 2.9: Pure bending loading conditions to achieve cylindrical bending[28][25]

$$M_y = \frac{D\nu_m - \beta h}{D + \gamma h} M_x \tag{2.18}$$

where it can be seen that when the Cosserat elastic constants β and γ become zero, the formula reduces to Cauchy. The BPR can then be defined as:

$$\frac{D\nu_m - \beta h}{D + \gamma h} = BPR \tag{2.19}$$

and this also implies that the BPR should converge to the IPR when the Cosserat constants approach zero. This relation shows how the BPR dependends on two Cosserat parameters, where as h approaches zero γ dominates the behaviour and β drops out[28]. So for thin plates γ seems to be the Cosserat constant that should mostly influence the bending-induced double curvature. This seems interesting for further research into the Cosserat elastic constants, but for this research the BPR is used as a whole. This turns Equation 2.18 and Equation 2.19 into Equation 2.20.

$$BPR = \frac{M_y}{M_x} \tag{2.20}$$

For the cylindrical bending test, due to the zero double curvature, Equation 2.17 reduces to one unknown term per equation. Using the applied curvature, the resulting moments due to this curvature and the RVE dimensions, D_{66} and D_{99} can be calculated. Using the reaction moment that is required to keep the cylindrical shape, the applied curvature and the RVE dimensions, D_{69} can be calculated.

These bending load cases were performed in COMSOL Multiphysics for the Star-shaped unit-cell and the anti-tri-chiral unit-cell. Rigid connectors were used to either prescribe a rotation, or to constrain a rotation. The reaction moments on these rigid connectors could then be evaluated. For the alternative RVE of the star-shaped unit-cell and the RVE of the anti-tri-chiral unit-cell, periodic boundary conditions were used to maintain allignment. Due to the symmetry of the star-shaped unit-cell, the bending load cases are identical and therefore only one load case was performed. For the anti-tri-chiral unit-cell this was not the case and therefore both load cases were performed. This does allow for extra validation as D_{69} can be computed from both load cases and compared. The bending test was performed for two different mesh sizes. For the star-shaped unit-cell the bending test was performed for two different RVE's. Due to time constraints this was not done for the anti-tri-chiral unit-cell. The BPR of the star-shaped unit-cell was determined using Equation 2.20. For the anti-tri-chiral unit-cell the BPR was calculated using $BPR = D_{69}/D_{66}$ to account for the orthorhombic size of the RVE.

To get more insight into the influence of the unit-cell geometry on the BPR, the cylindrical bending test was analysed for different parameters using parametric sweeps in COMSOL Multiphysics. Three relations were of interest regarding the flexures that the unit-cell consists of, namely h/l, h/w and w/l. Here h is the height flexure, l is the flexure length and w is the flexure width (see Figure 2.1). The ratio h/l relates the in-plane size of the unit-cell with the out-of plane size. Eskandari et al. showed how

this relation is influential for the BPR[14]. The ratio h/w desribes the cross-section of the flexure. This ratio describes if the flexure is shaped like a flexure or more like a beam. This relation is of interest as it could provide insight into the situation where the flexure can be approximated as an actual flexure or as a beam. The ratio w/l desribes the relative wall thickness. From this ratio it could be determined if thin-walled approximations are valid. For the anti-tri-chiral unit-cell another parameter, namely the diameter of the cylinder d is relevant. The ratio d/l is of particular interest, because it determines if the IPR is positive or negative, which was also observed by Alderson et al.[5]. For increasingly smaller values of d/l, the anti-tri-chiral unit-cell becomes more similar to a traditional honeycomb unit-cell. Here the rotation of the cylinders becomes less significant for the behaviour of the unit-cell. However it is still largely unknown how this influences the BPR. Alderson et al. presented one geometry for the anti-tri-chiral unit-cell, where the observed bending-induced double curvature was anticlastic[5]. By varying over d/l it can be analysed wether regions of negative BPR can be found.

2.3.3. Weak form

The weak form is a powerful tool in COMSOL Multiphysics. The weak form was used to add the additional degrees of freedom, in the form of microrotations to create a Cosserat continuum model, specifically for out-of-plane bending. Just like the homogenised Cauchy continuum model, a rectangular block is used to model the homogenised Cosserat continuum model and only a quarter of the rectangular block has to be modelled. The rectangular block has the same geometry but for the homogenised Cosserat continuum model, the extra bending load cases can be taken into account. To solve the weak form, the linear and angular momentum balances had to be satisfied, with the constitutive equations i.e. the asymmetric stress tensor (σ written as s in COMSOL Multiphysics) and the couple stress tensor m.

Based on the constitutive equations from Equation 2.9 and the work of Jeong et al.[21] and Rezaei et al.[18], a weak form model in COMSOL Multiphysics was constructed. Jeong et al.[18] used a Solid Mechanics physics node, which uses a Cauchy continuum, and added one weak form to insert the angular momentum balance. Rezaei et al.[18] used two weak forms, one for the linear momentum balance and one for the angular momentum balance. For this research, two weak forms were used. Both the linear momentum balance and the angular momentum balance have three dependent variables namely: u_1, u_2 and u_3 and a_1, a_2 and a_3 respectively. The weak form equations for the linear momentum balance and angular momentum balance respectively are as defined by Rezaei et al.[18]:

$$\begin{aligned} &-\int_D \sigma_{ij} V_{u_{j,i}} + \int_B \sigma_{ij} V_{u_j} n_i + \int_D P_j V_{u_j} = 0 \\ &-\int_D m_{ij} V_{a_{j,i}} + \int_B m_{ij} V_{a_j} n_i - \int_D e_{ijk}\sigma_{ik} V_{a_j} + \int_D Q_j V_{a_j} = 0 \end{aligned} \tag{2.21}$$

where the test function is denoted as V, D is the computational domain and B is the surface boundary around the domain. Body forces P and body couples Q are assumed to be zero as no force or couple is applied at the domain level. The linear momentum balance contains the test functions regarding the translations to determine the translations u_1, u_2 and u_3. The translations influence the stresses through strains, which can be seen in Figure 2.8. The angular momentum balance contains the test functions regarding the microrotations to determine the microrotations a_1, a_2 and a_3. The microrotations influence the couple stress through curvature, but also the shear stress which can be seen in Figure 2.8.

Applying the linear momentum balance from Equation 2.21, the weak expressions are given in Equation 2.22. Here it can be seen that every line corresponds to one of the dependent variables u_1, u_2 and u_3. Setting up the boundary conditions in the weak form is different than for other physics nodes. For the linear momentum balance three Dirichlet boundary conditions were used. One to prescribe zero displacement on the edge number two in Figure 2.5 and the other two to act as symmetry boundary conditions. Here only the movement out-of-plane is fixed, which were applied to boundary planes two and three in Figure 2.5. The boundary conditions are not a part of the weak expressions of Equation 2.22.

$$
\begin{aligned}
&- (s11 * test(u1X) + s12 * test(u1Y) + s13 * test(u1Z)) \\
&- (s21 * test(u2X) + s22 * test(u2Y) + s23 * test(u2Z)) \\
&- (s31 * test(u3X) + s32 * test(u3Y) + s33 * test(u3Z))
\end{aligned} \tag{2.22}
$$

In the weak form of the angular momentum balance, the weak expressions are given in Equation 2.23. Here it can be seen that every line corresponds to one of the dependent variables a_1, a_2 and a_3. For the angular momententum balance three Dirichlet boundary conditions were used as wel. One to prescribe zero microrotations on edge number two in Figure 2.5 and the other two to act as symmetry boundary conditions. Here both microrotations in-plane are fixed, which were applied to boundary planes two and three in Figure 2.5. Also through a weak contribution an external moment was applied on boundary plane four.

$$
\begin{aligned}
&- m11 * test(a1X) - m12 * test(a1Y) - m13 * test(a1Z) - (s23 - s32) * test(a1) \\
&- m21 * test(a2X) - m22 * test(a2Y) - m23 * test(a2Z) - (s31 - s13) * test(a2) \\
&- m31 * test(a3X) - m32 * test(a3Y) - m33 * test(a3Z) - (s12 - s21) * test(a3)
\end{aligned} \tag{2.23}
$$

2.4. Validation

In this section, the results from the Cauchy homogenisation and the bending tests are presented. The validity of these results are analysed by calculating the Mean Average Percentage Error (MAPE), for both the different mesh sizes and the different RVE sizes. The MAPE can be used to determine how changing the mesh size or RVE size changes the resulting elasticity tensor. If the MAPE is low, it can be assumed that the respective results have converged. Also the functionality of the Cosserat continuum weak form model is evaluated.

Three comparisons were formulated to apply the MAPE to. The effect of mesh refinement can be determined for both RVE's by comparing the elasticity tensors at different mesh sizes. Also the effect of the RVE can be determined by comparing the elasticity tensors of the two different RVE's, which was done for the fine mesh. The formula for MAPE is:

$$
\text{MAPE} = \frac{100\%}{n} \sum_{i=1}^{n} \left| \frac{a_i - p_i}{a_i} \right| \tag{2.24}
$$

where, a_i represents the more accurate result i.e. smaller mesh size or larger RVE. p_i represents the less accurate result. n is the number of elastic constants that are taken into account. For the comparison of the Cauchy homogenisation, the in-plane elastic constants C_{11}, C_{22}, C_{12} and C_{66} (indicated with blue color) of each respective elasticity tensor were used. For the comparison of the cylindrical bending test, D_{11}, D_{22}, D_{12}, and D_{21} were used. Identical numbers due to symmetry of the tensor were excluded.

2.4.1. Cauchy Homogensiation star-shaped unit-cell

The Cauchy elasticity tensor of the star-shaped unit-cell (in Voigt notation) was determined for average axial strains of 0.1 and average shear strains of 0.05. The results using the first RVE with normal mesh size, first RVE with fine mesh size, alternative RVE with normal mesh size and alternative RVE with fine mesh size are respectively given in Equation 2.25, Equation 2.26, Equation 2.27 and Equation 2.28. It can be seen that C_{12} and C_{21} ,the two off-diagonal numbers marked with blue, are positive. This indicates a positive Poisson's ratio in-plane. The elasticity tensor displays couplings not expected for an orthotropic material, defined in Equation 2.3. The expected elastic constants for an orthotropic material are marked with blue and yellow. However, most unexpected couplings are at least a factor ten smaller than the expected couplings and are assumed to be insignificant. A significant out-of-plane axial to shear coupling is present. Axial out-of-plane deformation is assumed to be insignificant in the case of bending and for plate theory it can be assumed that σ_{33} is zero i.e. no change in thickness of the plate occurs. The unexpected couplings might be an effect of the thin-walled nature of the unit-cell.

In Table 2.2, the resulting MAPE values can be seen. Mesh refinement of the alternative RVE has a greater MAPE value than mesh refinement for the first RVE. This difference seems to indicate that the first RVE is better converged than the alternative RVE. This could be due to the larger size of the alternative RVE, where small inaccuracies of the mesh are present at more locations compared to the first RVE. The MAPE for the RVE size is relatively low compared to the other MAPE values. So changing from the first RVE to the alternative RVE at a fine mesh, has less influence on the results that canging from a normal mesh to a fine mesh for a fixed RVE. This seems to indicate that both RVE's represent the same overall behaviour. This demonstrates how the size of the RVE should be independent from the homogenisation results.

MAPE mesh refinement first RVE	0.82%
MAPE mesh refinement alternative RVE	2.05%
MAPE RVE size	0.72%

Table 2.2: Star-shaped unit-cell MAPE results

In Figure 2.10 and Figure 2.11 the load cases applied to the two choices of RVE are visualised. Due to the symmetry of the star-shaped unit-cell, the principal strain in the x and y direction show the same behaviour. This is also the case for the out-of plane shear strain for yz and xz. For principal strain in the x and y direction, the shape of the star changes, while for shear strain in the xy direction, the star-shape remains unchanged and the surrounding flexures bend. The behaviour of the two RVE's seems identical, further confirming that the choice RVE is valid.

$$\begin{pmatrix}\sigma_{11}\\ \sigma_{22}\\ \sigma_{33}\\ \sigma_{23}\\ \sigma_{13}\\ \sigma_{12}\end{pmatrix} = \begin{bmatrix} 91198 & 32897 & 50885 & 1190.7 & 638.26 & 3377.6 \\ 32897 & 91149 & 50870 & 631.18 & 1208.0 & 3379.0 \\ 50885 & 50870 & 1.6986E7 & 2.0074E5 & 2.0076E5 & 2705.9 \\ 1190.7 & 631.18 & 2.0074E5 & 1.5697E6 & -93.872 & 2.9886 \\ 638.26 & 1208.0 & 2.0076E5 & -93.872 & 1.5697E6 & -1.5567 \\ 3377.6 & 3379.0 & 2705.9 & 2.9886 & -1.5567 & 7198.1 \end{bmatrix} \begin{pmatrix}\epsilon_{11}\\ \epsilon_{22}\\ \epsilon_{33}\\ 2\epsilon_{23}\\ 2\epsilon_{13}\\ 2\epsilon_{12}\end{pmatrix} \tag{2.25}$$

$$\begin{pmatrix}\sigma_{11}\\ \sigma_{22}\\ \sigma_{33}\\ \sigma_{23}\\ \sigma_{13}\\ \sigma_{12}\end{pmatrix} = \begin{bmatrix} 90648 & 32578 & 50507 & 1201.1 & 653.5 & 3346.5 \\ 32578 & 90480 & 50440 & 660.38 & 1195.9 & 3337.4 \\ 50507 & 50440 & 1.6988E7 & 2.0078E5 & 2.0079E5 & 2674.8 \\ 1201.1 & 660.38 & 2.0079E5 & 1.5682E6 & 5.4377 & -2.1778 \\ 653.50 & 1195.9 & 2.0079E5 & 5.4377 & 1.5685E6 & -3.8182 \\ 3346.5 & 3337.4 & 2674.8 & -2.1778 & -3.8182 & 7131.4 \end{bmatrix} \begin{pmatrix}\epsilon_{11}\\ \epsilon_{22}\\ \epsilon_{33}\\ 2\epsilon_{23}\\ 2\epsilon_{13}\\ 2\epsilon_{12}\end{pmatrix} \tag{2.26}$$

$$\begin{pmatrix}\sigma_{11}\\ \sigma_{22}\\ \sigma_{33}\\ \sigma_{23}\\ \sigma_{13}\\ \sigma_{12}\end{pmatrix} = \begin{bmatrix} 92720 & 34113 & 51887 & 1184.4 & 636.59 & 3452.0 \\ 34113 & 92769 & 51906 & 623.54 & 1225.2 & 3454.5 \\ 51887 & 51906 & 1.6985E7 & 2.0070E5 & 2.0072E5 & 2764.5 \\ 1184.4 & 623.54 & 2.0070E5 & 1.5701E6 & -24.915 & 10.331 \\ 636.59 & 1225.2 & 2.0072E5 & -24.915 & 1.5700E6 & -0.0056690 \\ 3452.0 & 3454.5 & 2764.5 & 10.331 & -0.0056690 & 7211.6 \end{bmatrix} \begin{pmatrix}\epsilon_{11}\\ \epsilon_{22}\\ \epsilon_{33}\\ 2\epsilon_{23}\\ 2\epsilon_{13}\\ 2\epsilon_{12}\end{pmatrix} \tag{2.27}$$

$$\begin{pmatrix}\sigma_{11}\\ \sigma_{22}\\ \sigma_{33}\\ \sigma_{23}\\ \sigma_{13}\\ \sigma_{12}\end{pmatrix} = \begin{bmatrix} 91105 & 33047 & 50872 & 1207.0 & 650.17 & 3361.3 \\ 33047 & 91119 & 50875 & 656.36 & 1198.4 & 3364.7 \\ 50872 & 50875 & 1.6984E7 & 2.0071E5 & 2.0078E5 & 2692.6 \\ 1207.0 & 656.36 & 2.0071E5 & 1.5687E6 & 5.3606 & 2.1589 \\ 650.17 & 1198.4 & 2.0078E5 & 5.3606 & 1.5687E6 & 1.8443 \\ 3361.3 & 3364.7 & 2692.6 & 2.1589 & 1.8443 & 7112.8 \end{bmatrix} \begin{pmatrix}\epsilon_{11}\\ \epsilon_{22}\\ \epsilon_{33}\\ 2\epsilon_{23}\\ 2\epsilon_{13}\\ 2\epsilon_{12}\end{pmatrix} \tag{2.28}$$

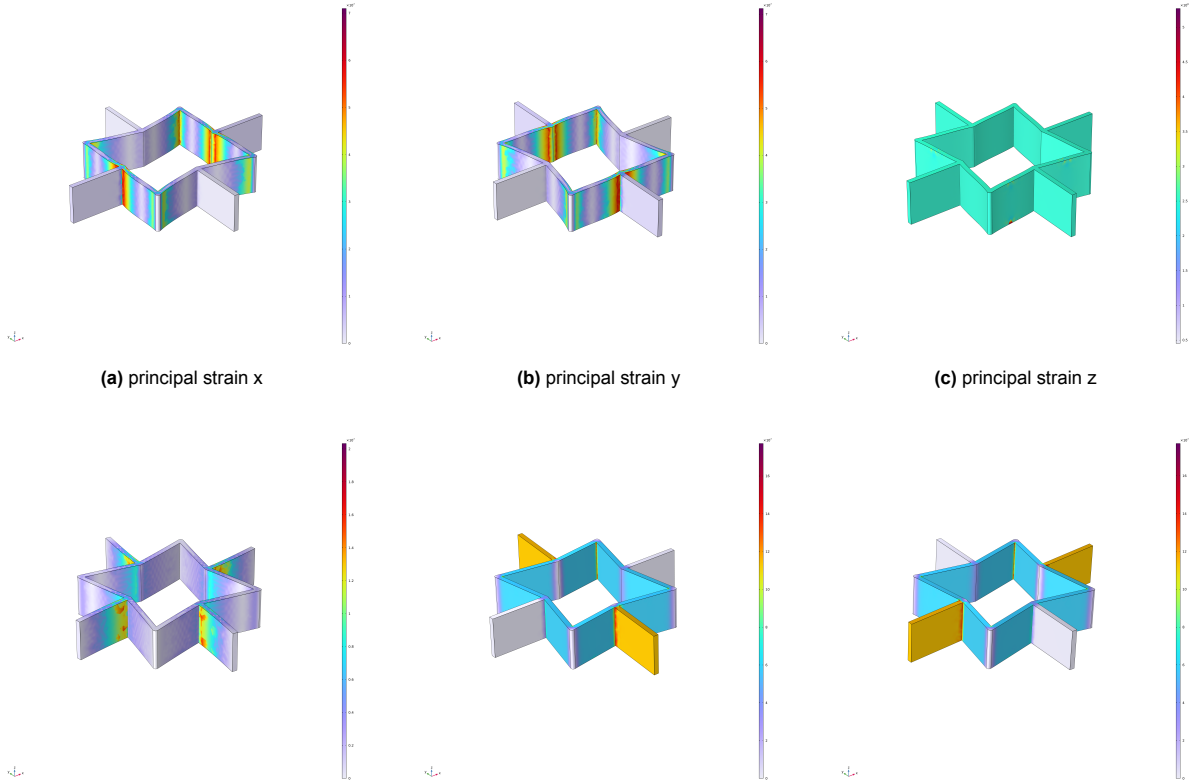

(a) principal strain x **(b)** principal strain y **(c)** principal strain z

(d) shear strain xy **(e)** shear strain yz **(f)** shear strain xz

Figure 2.10: six load cases applied to the star-shaped unit-cell (fine mesh)

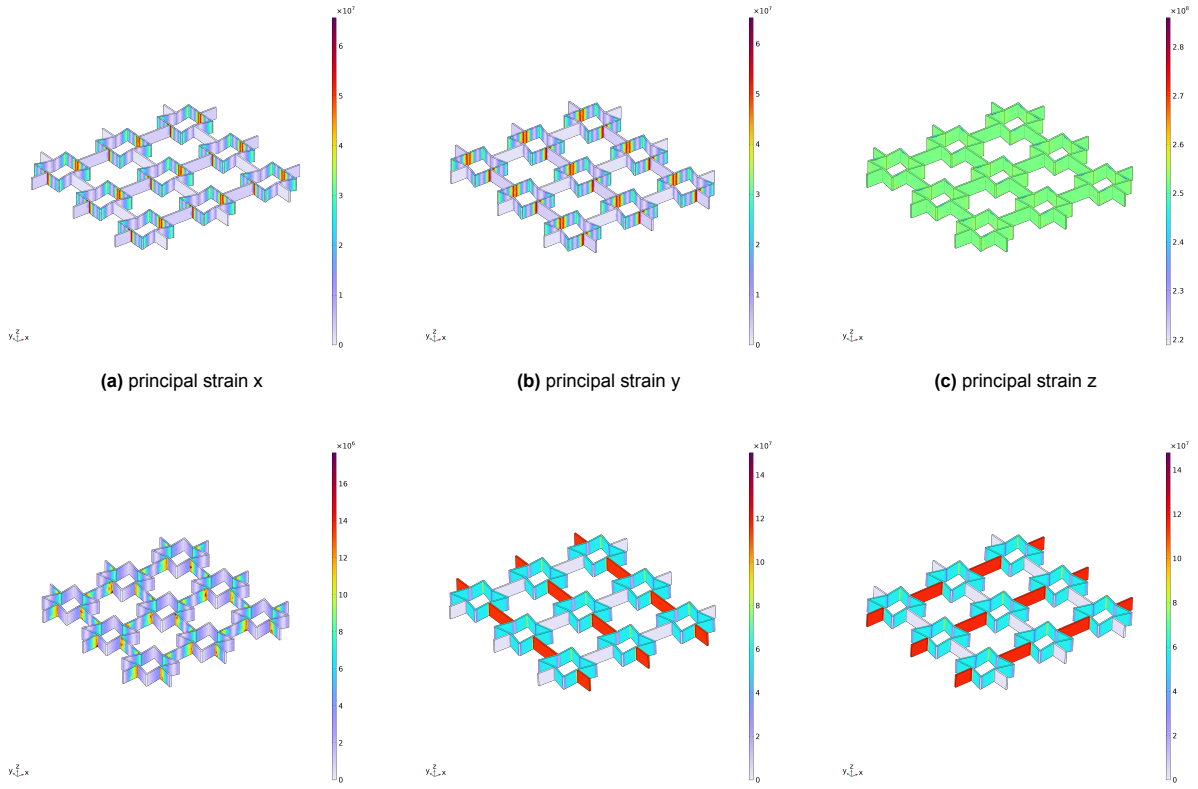

(a) principal strain x **(b)** principal strain y **(c)** principal strain z

(d) shear strain xy **(e)** shear strain yz **(f)** shear strain xz

Figure 2.11: six load cases applied to the alternative RVE of the star-shaped unit-cell (fine mesh)

2.4.2. Cauchy homogenisation anti-Tri-Chiral unit-cell

The Cauchy elasticity tensor of the anti-tri-chiral unit-cell (in Voigt notation) was determined for average axial strains of 0.1 and average shear strains of 0.05. The results of the first RVE with normal mesh size, first RVE with fine mesh size, the alternative RVE with normal mesh size, and alternative RVE with fine mesh size are respectively given in Equation 2.29, Equation 2.30, Equation 2.31 and Equation 2.32. It can be seen that the off-diagonal components marked in blue at C_{12} and C_{21} are negative, indicating a negative Poisson's ratio. Similarly to the star-shaped unit-cell, unexpected couplings are present with the largest being the out-of-plane axial to shear coupling. Another unexpected coupling that is present is the coupling between in-plane axial to shear. This coupling might be attributed to the anti-chiral nature of the unit-cell, as chiral unit-cells display a significant axial to shear coupling.

in Table 2.3, the resulting MAPE values can be seen. Both mesh refinements have a similar MAPE value. The difference in size between the different RVE's is smaller than that of the star-shaped unit-cells, which could explain the difference. The MAPE values of the mesh refinement are higher than that of the star-shaped unit-cell, which indicate that the star-shaped unit-cell is better converged that the anti-tri-chiral unit-cell. This is likely the result of the small cylinders present in the anti-tri-chiral unit-cell, as circular shapes require a finer mesh to accurately represent than rectangular shapes. The MAPE of the RVE size is low, indicating that both RVE's represent the same overall behaviour. This demonstrates that not only the size, but also the shape of the RVE should be independent from the homogenisation results.

MAPE mesh refinement first RVE	2.84%
MAPE mesh refinement alternative RVE	2.76%
MAPE RVE size	0.24%

Table 2.3: Star-shaped unit-cell MAPE results Cauchy homogenisation

In Figure 2.12 and Figure 2.13 the load cases applied to the RVE are visualised. The response of the

different RVE's for an identical load case can be compared. It can be seen that the amount of stress and location of the stress is similar. For Figure 2.12 (c) and Figure 2.13 (c) the colours are different, but this can be attributed to the automatic scaling of the colour gradient. From the colour table it can be seen that the different colours both represent roughly the same value. For principal strain in the x and y directions, it can be seen that the applied tension rotates the cylinders. This movement pushes the other flexures around the cylinder outwards, creating the auxetic behaviour. The behaviour of the two RVE's seems identical, further confirming that the choice of RVE is valid.

$$\begin{pmatrix}\sigma_{11}\\ \sigma_{22}\\ \sigma_{33}\\ \sigma_{23}\\ \sigma_{13}\\ \sigma_{12}\end{pmatrix} = \begin{bmatrix} 5981.0 & -3309.4 & 1470.3 & 109.70 & -4.6075 & 527.82 \\ -3309.4 & 7078.2 & 1481.3 & -4.4499 & 112.78 & -514.42 \\ 1470.3 & 1481.3 & 3.1233E6 & 36920 & 36922 & 8.6166 \\ 109.70 & -4.4499 & 36920 & 2.5659E5 & -7.4526 & 1.1408 \\ -4.6075 & 112.78 & 36922 & -7.4526 & 2.5657E5 & 0.97944 \\ 527.82 & -514.42 & 8.6616 & 1.1408 & 0.97944 & 4699.7 \end{bmatrix} \begin{pmatrix}\epsilon_{11}\\ \epsilon_{22}\\ \epsilon_{33}\\ 2\epsilon_{23}\\ 2\epsilon_{13}\\ \epsilon_{12}\end{pmatrix} \tag{2.29}$$

$$\begin{pmatrix}\sigma_{11}\\ \sigma_{22}\\ \sigma_{33}\\ \sigma_{23}\\ \sigma_{13}\\ \sigma_{12}\end{pmatrix} = \begin{bmatrix} 5863.8 & -3190.1 & 1459.8 & 105.97 & -0.59642 & 509.87 \\ -3190.1 & 6886.8 & 1456.4 & -0.83498 & 108.39 & -486.26 \\ 1459.8 & 1456.4 & 3.1233E6 & 36919 & 36920 & 11.994 \\ 105.97 & -0.83498 & 36919 & 2.5589E5 & -24.436 & -0.053944 \\ -0.59642 & 108.39 & 36920 & -24.436 & 2.5596E5 & 0.20203 \\ 509.87 & -486.26 & 11.994 & -0.053944 & 0.20203 & 4570.3 \end{bmatrix} \begin{pmatrix}\epsilon_{11}\\ \epsilon_{22}\\ \epsilon_{33}\\ 2\epsilon_{23}\\ 2\epsilon_{13}\\ 2\epsilon_{12}\end{pmatrix} \tag{2.30}$$

$$\begin{pmatrix}\sigma_{11}\\ \sigma_{22}\\ \sigma_{33}\\ \sigma_{23}\\ \sigma_{13}\\ \sigma_{12}\end{pmatrix} = \begin{bmatrix} 5992.1 & -3308.8 & 1475.5 & 11.23 & -2.5292 & 535.08 \\ -3308.8 & 7065.5 & 1477.5 & -5.6467 & 114.46 & -509.13 \\ 1475.5 & 1477.5 & 3.1233E6 & 36919 & 36926 & 13.944 \\ 111.23 & -5.6467 & 36919 & 2.5658E5 & 10.771 & 1.8492 \\ -2.5292 & 114.46 & 36926 & 10.771 & 2.5662E5 & 3.3356 \\ 535.08 & -509.13 & 13.944 & 1.8492 & 3.3356 & 4712.7 \end{bmatrix} \begin{pmatrix}\epsilon_{11}\\ \epsilon_{22}\\ \epsilon_{33}\\ 2\epsilon_{23}\\ 2\epsilon_{13}\\ 2\epsilon_{12}\end{pmatrix} \tag{2.31}$$

$$\begin{pmatrix}\sigma_{11}\\ \sigma_{22}\\ \sigma_{33}\\ \sigma_{23}\\ \sigma_{13}\\ \sigma_{12}\end{pmatrix} = \begin{bmatrix} 5876.1 & -3202.7 & 1461.3 & 107.53 & -3.1667 & 514.23 \\ -3202.7 & 6897.2 & 1455.4 & -3.9490 & 107.66 & -493.58 \\ 1461.3 & 1455.4 & 3.1233E6 & 36917 & 36917 & 10.640 \\ 107.53 & -3.9490 & 36917 & 2.5594E5 & 3.6376 & -0.041435 \\ -3.1667 & 107.66 & 36917 & 3.6376 & 2.5594E5 & -0.71605 \\ 514.3 & -493.58 & 10.640 & -0.041435 & -0.71605 & 4560.8 \end{bmatrix} \begin{pmatrix}\epsilon_{11}\\ \epsilon_{22}\\ \epsilon_{33}\\ 2\epsilon_{23}\\ 2\epsilon_{13}\\ 2\epsilon_{12}\end{pmatrix} \tag{2.32}$$

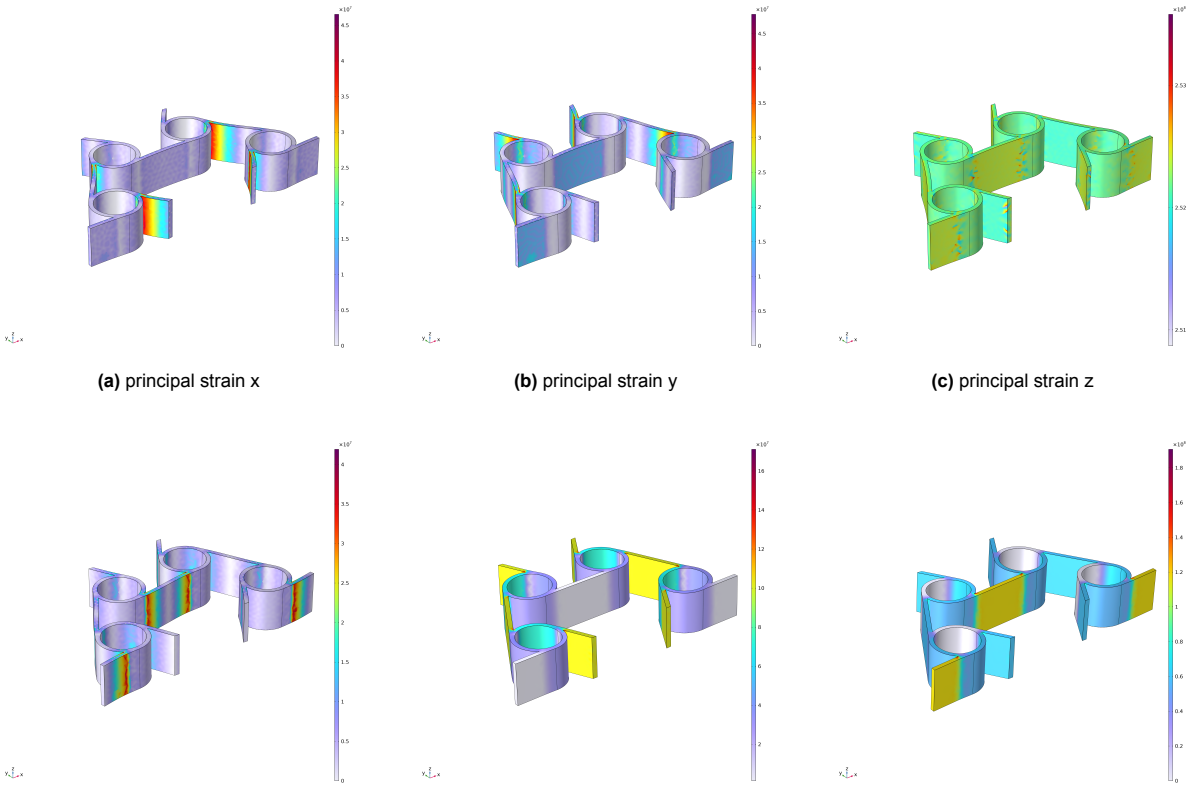

(a) principal strain x **(b)** principal strain y **(c)** principal strain z

(d) shear strain xy **(e)** shear strain yz **(f)** shear strain xz

Figure 2.12: six load cases applied to the first RVE of the anti-tri-chiral unit-cell with finer mesh

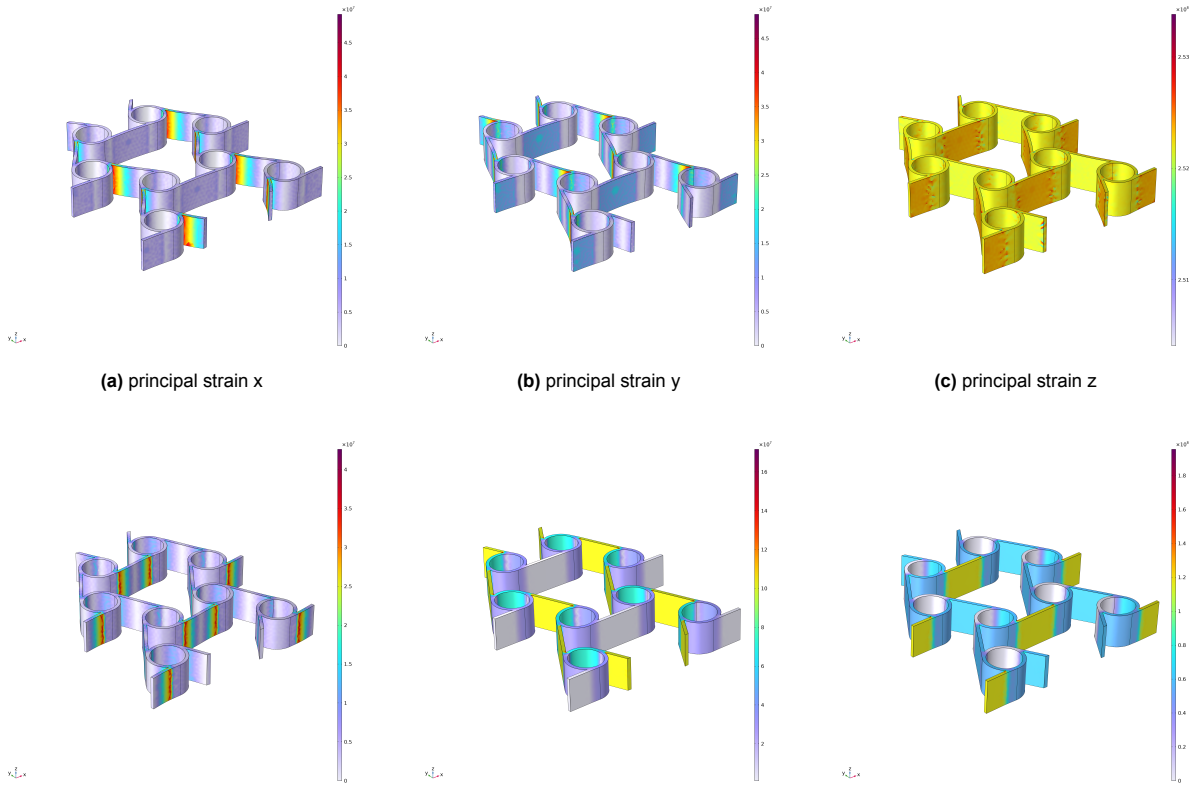

(a) principal strain x **(b)** principal strain y **(c)** principal strain z

(d) shear strain xy **(e)** shear strain yz **(f)** shear strain xz

Figure 2.13: six load cases applied to an alternative RVE of the anti-tri-chiral unit-cell with finer mesh

2.4.3. Cylindrical Bending test star-shaped unit-cell

In Figure 2.14 the cylindrical bending of the star-shaped unit-cell can be seen. For the star-shaped unit-cell, the out-of-plane bending section of the D-matrix was determined for a curvature of $6.35 rad/m$. The results of the first RVE with fine mesh size, the first RVE with finer mesh size, the alternative RVE with fine mesh size, and alternative RVE with finer mesh size are presented in Equation 2.33, Equation 2.34, Equation 2.35 and Equation 2.36 respectively. The off-diagonal components are negative indicating a negative BPR. As stated in the methodology, due to the symmetry of the star-shaped unit-cell $\mu_{12} = \mu_{21}$.

In Table 2.4, the resulting MAPE values can be seen. The MAPE values are low, especially the MAPE of the RVE size, indicating that that both RVE's represent the same behaviour. The size of the RVE does not seem to influence the resulting bending section of the D-matrix. In Figure 2.14, the cylindrical bending test applied to both RVE sizes are visualised.

MAPE first RVE mesh refinement	1.16%
MAPE alternative RVE mesh refinement	0.51%
MAPE RVE size	0.07%

Table 2.4: Star-shaped unit-cell MAPE results cylindrical bending

$$\begin{pmatrix} \mu_{12} \\ \mu_{21} \end{pmatrix} = \begin{bmatrix} 7.21475 & -1.97063 \\ -1.97063 & 7.21475 \end{bmatrix} \begin{pmatrix} \kappa_{12} \\ \kappa_{21} \end{pmatrix} \tag{2.33}$$

$$\begin{pmatrix} \mu_{12} \\ \mu_{21} \end{pmatrix} = \begin{bmatrix} 7.1175 & -1.95188 \\ -1.95188 & 7.1175 \end{bmatrix} \begin{pmatrix} \kappa_{12} \\ \kappa_{21} \end{pmatrix} \tag{2.34}$$

$$\begin{pmatrix} \mu_{12} \\ \mu_{21} \end{pmatrix} = \begin{bmatrix} 7.19113 & -1.97974 \\ -1.97974 & 7.19113 \end{bmatrix} \begin{pmatrix} \kappa_{12} \\ \kappa_{21} \end{pmatrix} \tag{2.35}$$

$$\begin{pmatrix} \mu_{12} \\ \mu_{21} \end{pmatrix} = \begin{bmatrix} 7.1183 & -1.95436 \\ -1.95436 & 7.1183 \end{bmatrix} \begin{pmatrix} \kappa_{12} \\ \kappa_{21} \end{pmatrix} \tag{2.36}$$

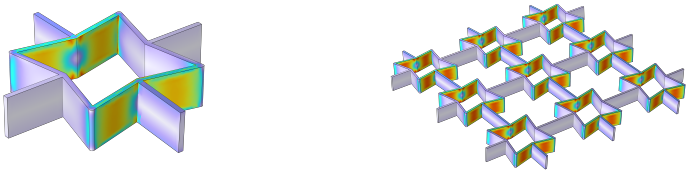

(a) bending first RVE **(b)** bending alternative RVE

Figure 2.14: Cylindrical bending test star-shaped unit-cell

2.4.4. Cylindrical bending test anti-tri-chiral unit-cell

In Figure 2.15, the cylindrical bending of the anti-tri-chiral unit-cell can be seen. For the anti-tri-chiral unit-cell, the out-of-plane bending section of the D-matrix was determined for a curvature of $13.3 rad/m$. Due to the orthorhombic symmetry of the anti-tri-chiral unit-cell, the bending test was done in two directions, which can be seen in Figure 2.15. The results of the first RVE with fine mesh size and the first RVE with finer mesh size are presented in Equation 2.37 and Equation 2.38 respectively. Due to time constraints, the cylindrical bending test could not be repeated for the alternative RVE.

In Table 2.5, the resulting MAPE values can be seen. Mesh refinement of the first RVE has a small MAPE value, indicating that convergence of the mesh can be assumed. The mesh refinement for the cylindrical bending tests was done from a fine mesh size to a finer mesh size, compared to the normal mesh size to fine mesh size of the homogenisation. So it seems that the fine mesh size is small enough to accurately model the cylindrical features of the anti-tri-chiral unit-cell.

The MAPE values for the off-diagonal components are quite high for both mesh sizes. The off-diagonal components were assumed to be symmetric based on Cui et al.[27], Eskandari et al.[14] and Yao et al.[15]. However, based on the obtained values this cannot be validated. It might be possible that additional couplings like bending to torsion are present for the anti-tri-chiral RVE. The symmetry group of the orthorhombic RVE of the anti-tri-chiral unit-cell was not found. However, the possible coupling of the $3m$ symmetry group of the anti-tri-chiral unit-cell itself were described by Cui et al.[27]. These include possible axial to bending, shear to bending, rotation to bending and torsion to bending couplings[27]. The presence of additional couplings would make Equation 2.17 invalid, as additional coupling terms would have to be added. The cylindrical bending test itself should remain a valid load case, where one out-of-plane couple strain is applied and the resulting couple stresses can be observed. However, it should be carefully evaluated that no unexpected strains or couple strains are present during the cylindrical bending test, as this would add additional variables to the equation.

MAPE first RVE mesh refinement	0.60%
MAPE first RVE off-diagonal components fine mesh	37.41%
MAPE first RVE off-diagonal components finer mesh	39.51%

Table 2.5: anti-tri-chiral unit-cell MAPE results cylindrical bending

$$\begin{pmatrix} \mu_{12} \\ \mu_{21} \end{pmatrix} = \begin{bmatrix} 26.0664 & 12.1377 \\ 8.8329 & 52.5390 \end{bmatrix} \begin{pmatrix} \kappa_{12} \\ \kappa_{21} \end{pmatrix} \tag{2.37}$$

$$\begin{pmatrix} \mu_{12} \\ \mu_{21} \end{pmatrix} = \begin{bmatrix} 25.9538 & 12.1437 \\ 8.7046 & 52.3510 \end{bmatrix} \begin{pmatrix} \kappa_{12} \\ \kappa_{21} \end{pmatrix} \tag{2.38}$$

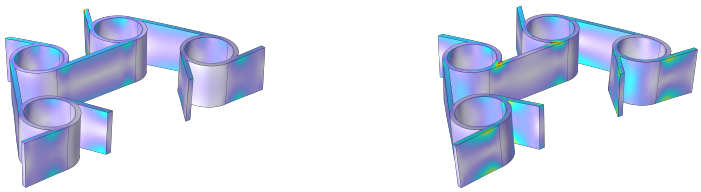

(a) bending over x-axis **(b)** bending over y-axis

Figure 2.15: Cylindrical bending test anti-tri-chiral unit-cell in both directions

2.4.5. Cosserat model

The Cosserat model should be able to display different types of bending-induced double curvature independently from its IPR. To validate the performance of the Cosserat model, the model was tested in tension and bending for different values of IPR and BPR. The results of this can be found in Figure 2.16 and Figure 2.17. Identical symmetry conditions as depicted in Figure 2.4 were used. The IPR determines the deformation perpendicular to the applied tension, which can be seen in Figure 2.16. At an IPR value of zero, there is no displacement perpendicular to the applied tension. It can be observed that varying the BPR does not influence the results. Also it can be observed that the displacements, indicated by the colour gradient, seem gradual and smooth.

The BPR determines the double curvature, which can be seen in Figure 2.17. This can be most easily seen by observing the angle of the color gradient, which moves from the heighest value (red) to the lowest point (dark blue). While varying the IPR does not significantly change the double curvature, it does affect the smoothness of the model. The IPR should not influence the bending behaviour at all, so this is an indication that something is not working correctly. Additionally, applying a moment using a weak contribution did not work as expected. In the weak contribution a moment was multiplied by a test function of the microrotation in the direction of bending. This is similar to how Rezaei et al.[18] used body couples on the domain level, but applied at the boundary level instead. However, the resulting weak contribution seems not to depend on the unit of the applied moment and instead just seems to use the numerical value to scale the microrotations at the boundary of the weak contribution. The result is not the same as the application of a rotation to a boundary, as applying a rotation suppresses double curvature at that boundary, which the applied weak contribution did not. The weak contribution does apply an initial curvature and the BPR does determine the induced double curvature, so the overall behaviour does seem similar to that of a moment.

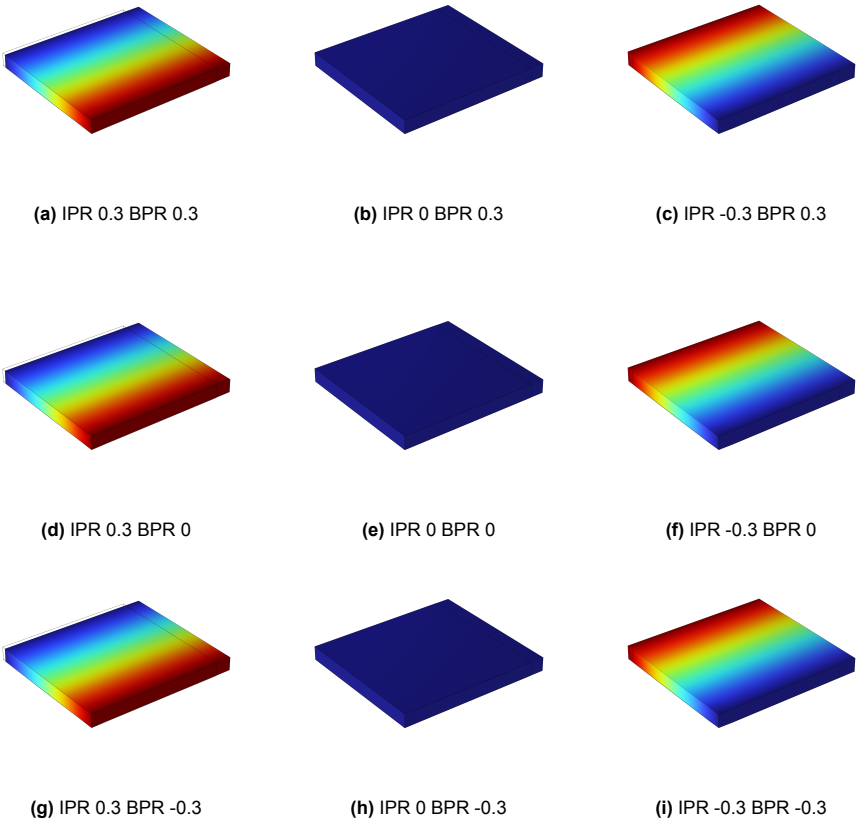

(a) IPR 0.3 BPR 0.3 **(b)** IPR 0 BPR 0.3 **(c)** IPR -0.3 BPR 0.3

(d) IPR 0.3 BPR 0 **(e)** IPR 0 BPR 0 **(f)** IPR -0.3 BPR 0

(g) IPR 0.3 BPR -0.3 **(h)** IPR 0 BPR -0.3 **(i)** IPR -0.3 BPR -0.3

Figure 2.16: Weak form model loaded in pure tension for varied IPR and BPR, the color indicates the displacement perpendicular to the applied tension

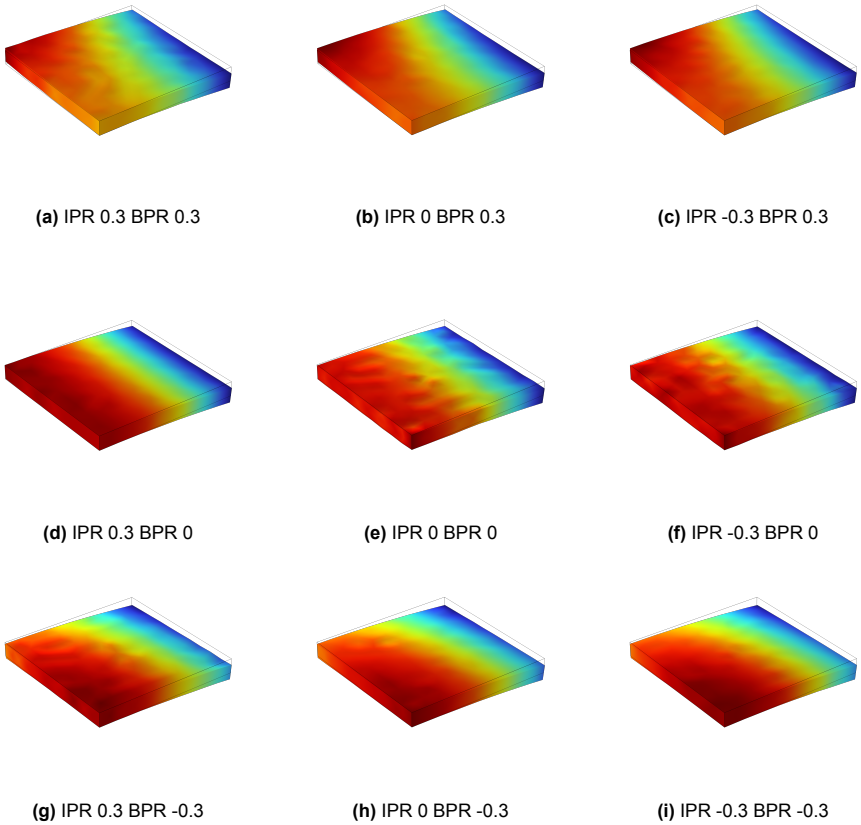

(a) IPR 0.3 BPR 0.3 **(b)** IPR 0 BPR 0.3 **(c)** IPR -0.3 BPR 0.3

(d) IPR 0.3 BPR 0 **(e)** IPR 0 BPR 0 **(f)** IPR -0.3 BPR 0

(g) IPR 0.3 BPR -0.3 **(h)** IPR 0 BPR -0.3 **(i)** IPR -0.3 BPR -0.3

Figure 2.17: Weak form model loaded in pure bending for varied IPR and BPR, the color indicates the displacement in the out-of-plane direction u_3

2.4.6. Validation models

For comparison purposes, detailed metaplates consisting of tesselated unit-cells were modelled in Solidworks and analysed with COMSOL Multiphysics. This was done for both the star-shaped unit-cell and the anti-tri-chiral unit-cell. The same general setup of applying bending on a quarter of the unit-cell, asshown in Figure 2.4 was used. Symmetry boundary conditions were applied with one fixed constraint to keep the model properly constrained. The bending moment was applied through multiple seperate moment boundary loads applied at the endpoints of the unit-cell flexures, as not to supress double curvature. The bending-induced double curvature of the detailed metaplates were determined by applying 2 rigid connectors along both symmetry planes. Through the use of the curl operator in the bending-induced double curvature of these metaplate models was be evaluated in terms of BPR.

In Solidworks, a long metaplate consisting of star-shaped unit-cells was made to observe the development of BPR for an increasingly long metaplate. This long metaplate was analysed in COMSOL Multiphysics. Mirroring was used so only half of the metaplate had to be modelled. The non mirrored end has a rigid bar onto which an out-of-plane moment is applied. This rigid bar supresses the double curvature. The theory behind this is that the influence of the rigid bar on double curvature, should becomes less influential at greater distances from the rigid bar. The star-shaped unit-cell was chosen for this with the same dimensions used for the homogenisation, mentioned in Figure 2.1. The total length of the metaplate varies from two to 16 unit-cells, where one to eight unit-cells are modelled. The metaplate is kept at a constant width of five unit-cells. A constant moment is applied along a rigid connector. An identical test was performed for another star-shaped unit-cell with an alternative geometry of $l = 4mm$, $h = 3mm$, $w = 0.5mm$.

The bending test of the long metaplate can be used to see if the BPR converges to the BPR determined through the cylindrical bending test. Here it is important to recognise the differences between these two methods, namely the fact that the bending test has a rigid bar at the ends where the moments are

applied. This means that the double curvature at the endpoints is zero and that the double curvature around the middle of the long metaplate is at its maximum. This is different from the cylindrical bending load case where the double curvature is equal throughout the metaplate.

2.4.7. Verdict validation

For the Cauchy homogenisation of both types of unit-cell, the type of in-plane Poisson's ratios were as expected. It can be confirmed that the RVE size does not have a significant impact on the homogenisation results. In further research the first i.e. smaller RVE could be used, as the resulting elasticity tensor loses no significant information compared to the alternative RVE. Also, further mesh refinement could be done for the anti-tri-chiral unit-cell to account for the cylindrical geometry. For the results, the Cauchy elasticity tensor of the alternative RVE with the fine mesh size was used for both the star-shaped unit-cell as the anti-tri-chiral unit-cell. The unexpected elastic constants in the Cauchy elasticity tensor will not be taken into account for the Cosserat elasticity tensor, as these couplings were not added to the Cosserat continuum model. For the homogenised Cauchy continuum model the unexpected elastic constants were taken into account.

For the cylindrical bending test of both types of unit-cell, the signs of the BPR ratios were as expected. For the star-shaped unit-cell it can be confirmed that both mesh size and RVE size do not have a significant effect on the resulting bending section of the D-matrix. For further research the first i.e. smaller RVE can be used. The bending section of the D-matrix of the anti-chiral unit-cell is not symmetric, while symmetry was expected based on literature. This indicates that the resulting bending section of the D-matrix might not be accurate. Further research is required to determine the couplings present for the anti-tri-chiral unit-cell RVE, to improve the application of the cylindrical bending test. For the star-shaped unit-cell, the bending part of the D-matrix of the altenative RVE with the finer mesh size was used for the Cosserat elasticity tensor. For the anti-tri-chiral unit-cell, the bending part of the D-matrix of the first RVE with the finer mesh size was used for the Cosserat elasticity tensor.

The Cosserat model is able to display different types of double curvature independently from the IPR. However, further refinement of the model is required to remove the deformation defects, i.e. increase the smoothnes, and to apply the moment more properly. It could be possible that the deformation defects are caused by the flawed application of the moment.

3

Results

The complete Cosserat elasticity tensors used for the star-shaped unit-cell are presented in Equation 3.1 and Equation 3.2. The complete Cosserat elasticity tensors used for the anti-tri-chiral unit-cell are presented in Equation 3.3 and Equation 3.4. For Equation 3.4 it can be seen that the the Cosserat elasticity tensor is not symmetric.

$$\begin{pmatrix}\sigma_{11}\\ \sigma_{22}\\ \sigma_{33}\\ \sigma_{23}\\ \sigma_{13}\\ \sigma_{12}\\ \sigma_{32}\\ \sigma_{31}\\ \sigma_{21}\end{pmatrix} = \begin{bmatrix} 91105 & 33047 & 50872 & 0 & 0 & 0 & 0 & 0 & 0 \\ & 91119 & 50875 & 0 & 0 & 0 & 0 & 0 & 0 \\ & & 1.6984E7 & 0 & 0 & 0 & 0 & 0 & 0 \\ & & & 1.5687E6 & 0 & 0 & 0 & 0 & 0 \\ & & & & 1.5687E6 & 0 & 0 & 0 & 0 \\ & & & & & 7112.8 & 0 & 0 & 0 \\ & & sym & & & & 1.5687E6 & 0 & 0 \\ & & & & & & & 1.5687E6 & 0 \\ & & & & & & & & 7112.8 \end{bmatrix} \begin{pmatrix}\epsilon_{11}\\ \epsilon_{22}\\ \epsilon_{33}\\ \epsilon_{23}\\ \epsilon_{13}\\ \epsilon_{12}\\ \epsilon_{32}\\ \epsilon_{31}\\ \epsilon_{21}\end{pmatrix} \tag{3.1}$$

$$\begin{pmatrix}m_{11}\\ m_{22}\\ m_{33}\\ m_{23}\\ m_{13}\\ m_{12}\\ m_{32}\\ m_{31}\\ m_{21}\end{pmatrix} = \begin{bmatrix} 0 & 0 & 0 & 0 & 0 & 0 & 0 & 0 & 0 \\ & 0 & 0 & 0 & 0 & 0 & 0 & 0 & 0 \\ & & 0 & 0 & 0 & 0 & 0 & 0 & 0 \\ & & & 0 & 0 & 0 & 0 & 0 & 0 \\ & & & & 0 & 0 & 0 & 0 & 0 \\ & & & & & 7.1175 & 0 & 0 & -1.95188 \\ & & sym & & & & 0 & 0 & 0 \\ & & & & & & & 0 & 0 \\ & & & & & & & & 7.1175 \end{bmatrix} \begin{pmatrix}\kappa_{11}\\ \kappa_{22}\\ \kappa_{33}\\ \kappa_{23}\\ \kappa_{13}\\ \kappa_{12}\\ \kappa_{32}\\ \kappa_{31}\\ \kappa_{21}\end{pmatrix} \tag{3.2}$$

$$\begin{pmatrix}\sigma_{11}\\ \sigma_{22}\\ \sigma_{33}\\ \sigma_{23}\\ \sigma_{13}\\ \sigma_{12}\\ \sigma_{32}\\ \sigma_{31}\\ \sigma_{21}\end{pmatrix} = \begin{bmatrix} 91105 & 33047 & 50872 & 0 & 0 & 0 & 0 & 0 & 0 \\ & 91119 & 50875 & 0 & 0 & 0 & 0 & 0 & 0 \\ & & 1.6984E7 & 0 & 0 & 0 & 0 & 0 & 0 \\ & & & 1.5687E6 & 0 & 0 & 0 & 0 & 0 \\ & & & & 1.5687E6 & 0 & 0 & 0 & 0 \\ & & & & & 7112.8 & 0 & 0 & 0 \\ & & sym & & & & 1.5687E6 & 0 & 0 \\ & & & & & & & 1.5687E6 & 0 \\ & & & & & & & & 7112.8 \end{bmatrix} \begin{pmatrix}\epsilon_{11}\\ \epsilon_{22}\\ \epsilon_{33}\\ \epsilon_{23}\\ \epsilon_{13}\\ \epsilon_{12}\\ \epsilon_{32}\\ \epsilon_{31}\\ \epsilon_{21}\end{pmatrix} \tag{3.3}$$

$$\begin{pmatrix} m_{11} \\ m_{22} \\ m_{33} \\ m_{23} \\ m_{13} \\ m_{12} \\ m_{32} \\ m_{31} \\ m_{21} \end{pmatrix} = \begin{bmatrix} 0 & 0 & 0 & 0 & 0 & 0 & 0 & 0 & 0 \\ 0 & 0 & 0 & 0 & 0 & 0 & 0 & 0 & 0 \\ 0 & 0 & 0 & 0 & 0 & 0 & 0 & 0 & 0 \\ 0 & 0 & 0 & 0 & 0 & 0 & 0 & 0 & 0 \\ 0 & 0 & 0 & 0 & 0 & 0 & 0 & 0 & 0 \\ 0 & 0 & 0 & 0 & 0 & 25.9538 & 0 & 0 & 12.1437 \\ 0 & 0 & 0 & 0 & 0 & 0 & 0 & 0 & 0 \\ 0 & 0 & 0 & 0 & 0 & 0 & 0 & 0 & 0 \\ 0 & 0 & 0 & 0 & 0 & 8.7046 & 0 & 0 & 52.3510 \end{bmatrix} \begin{pmatrix} \kappa_{11} \\ \kappa_{22} \\ \kappa_{33} \\ \kappa_{23} \\ \kappa_{13} \\ \kappa_{12} \\ \kappa_{32} \\ \kappa_{31} \\ \kappa_{21} \end{pmatrix} \tag{3.4}$$

3.1. Comparison metaplates

The FEA results of the actual metaplate, i.e. detailed metaplate, can be compared to the FEA results of the homogenised Cauchy and Cosserat continuum metaplates. For the star-shaped unit-cell, this can be seen in Figure 3.1. For the anti-tri-chiral unit-cell this can be seen in Figure 3.2. Additionally, a top view of the Cosserat continuum metaplates is presented in Figure 3.3. Similarly to Figure 2.17, it can be seen that deformation defects are present in the homogenised Cosserat continuum model for both the star-shaped unit-cell metaplate and the anti-tri-chiral unit-cell metaplate. Due to the symmetry of the anti-tri-chiral unit-cell, mirroring the metaplate in two directions is technically incorrect. Therefore, half the metaplate was modelled for the detailed metaplate. Due to time constraints, it was not possible to create a new models for the homogenised Cauchy and Cosserat metaplates, where half the plate was modelled. This oversight reduces the value of the comparison of the anti-tri-chiral unit-cell significantly. However, the type of bending-induced curvature can still be evaluated.

No BPR values were determined for the homogenised Cosserat metaplates, as the deformation defects would have likely influenced the result. Application of an identical moment for the detailed metaplate and the Cauchy metaplate resulted in different curvatures for both types of unit-cells. The bending stiffness of the homogenised Cauchy metaplate is determined through the flexural rigidity, which does not accurately describe the bending stiffness for metaplates. This was also concluded by Chen[12][13]. To determine the bending-induced double curvature, moments were applied that achieved a similar amount of principal curvature for both the detailed metaplate, the homogenised Cauchy continuum metaplate and the homogenised Cosserat continuum metaplate. Due to the pure bending loading condition applied, the resulting bending-induced double curvature should be independent of the amount of principal curvature applied in the linear elastic region. More principal curvature should translate to more double curvature, as $BPR = -k_{21}/k_{12}$.

The bending-induced double curvatures of these metaplate models were determined in terms of BPR. From the cylindrical bending test, the BPR values were determined as well. This is presented in Table 3.1.

Detailed metaplate	$BPR = -0.254$
Homogenised Cauchy continuum metaplate	$BPR = 0.313$
Cylindrical bending test	$BPR = -0.275$

(a) star-shaped unit-cell

Detailed metaplate half	$BPR = 0.837$
Homogenised Cauchy continuum metaplate	$BPR = -0.468$
Cylindrical bending test	$BPR = 0.335$

(b) anti-tri-chiral unit-cell

Table 3.1: BPR determined through different methods

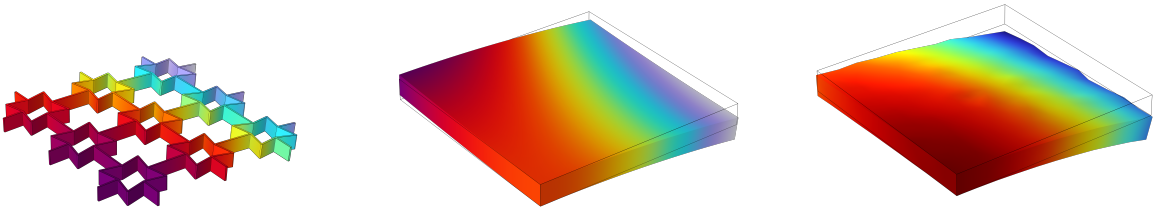

(a) star-shaped unit-cell, detailed metaplate

(b) star-shaped unit-cell, Cauchy continuum metaplate

(c) star-shaped unit-cell, Cosserat continuum metaplate

Figure 3.1: Comparison between the detailed, Cauchy continuum and Cosserat continuum metaplate for the star-shaped unit-cell

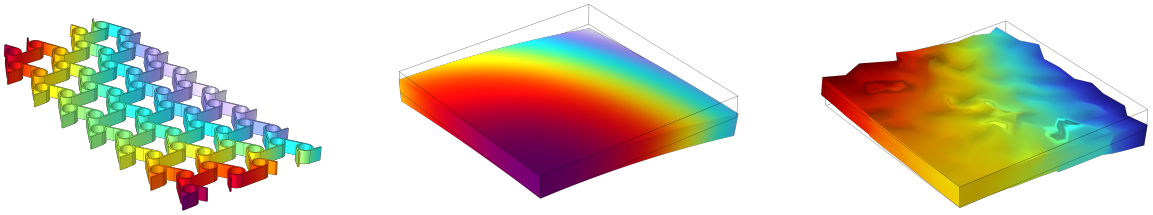

(a) Anti-tri-chiral unit-cell, half the metaplate is modelled

(b) Anti-tri-chiral unit-cell, Cauchy continuum metaplate

(c) Anti-tri-chiral unit-cell, Cosserat continuum metaplate

Figure 3.2: Comparison between the detailed, Cauchy continuum and Cosserat continuum metaplate for the anti-tri-chiral unit-cell

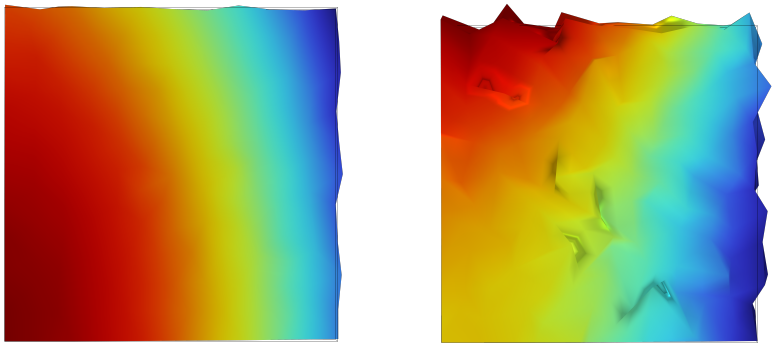

(a) Top view star-shaped unit-cell

(b) Top view anti-tri-chiral unit-cell

Figure 3.3: Top views of the Cosserat continuum models

3.2. Influence of geometry on IPR and BPR

In Figure 3.4, the relation between the BPR and the ratios h/l and h/w can be seen for the star-shaped unit-cell, as determined from the cylindrical bending test. For the parametric sweep w was kept constant at $0.5mm$. This means that every colored line represents a specific height, and that moving along a line from left to right makes the unit-cell smaller in-plane as l is reduced. Because the wall thickness

is kept constant, moving along a line from left to right also makes the unit-cell less thin-walled. It is important to note that moving straight down from line to line changes both the height h and the length l of the unit-cell to keep the relative height constant. w/l can be calculated at each point from h/l and h/w, but no convenient visualisation method was found for this ratio. In Figure 3.6 the extremes of w/l are visualised, where the most thin-walled unit-cell is located at left end of the bottom line, and the most thick walled unit-cell is located at the right end of the top line and the line below that. The top line is broken off at $h/l = 1.5$ as beyond that point the star-shaped unit-cell is no longer recognisable as a star-shaped unit-cell.

In Figure 3.5, the relation between the IPR and the ratios h/l and h/w can be seen for the star-shaped unit-cell. While the IPR of the star-shaped unit-cell remains positive, there is fluctuation in the magnitude of the IPR. For the $h/w = 2$ and $h/w = 4$ lines a decrease in IPR can be observed, as the unit-cells become more thick walled and start to look like Figure 3.6 (b).

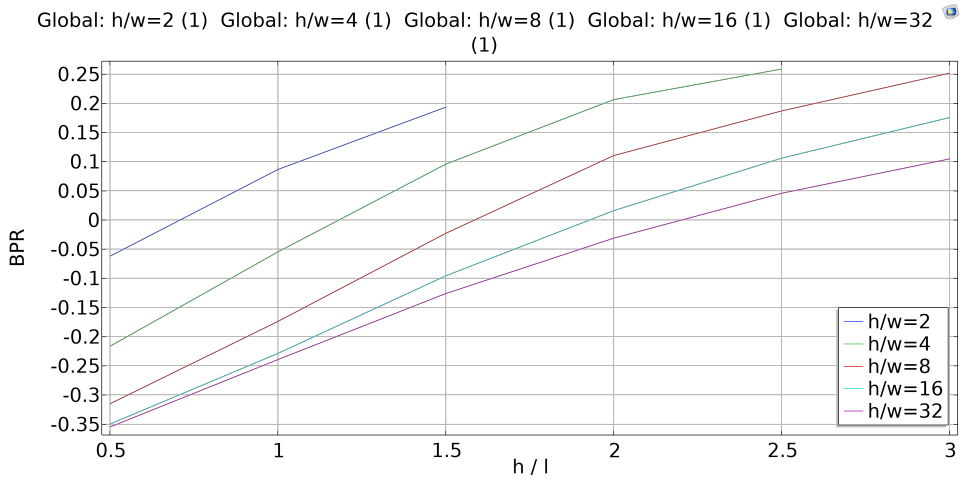

Figure 3.4: BPR values from cylindrical bending test of the star-shaped unit-cell

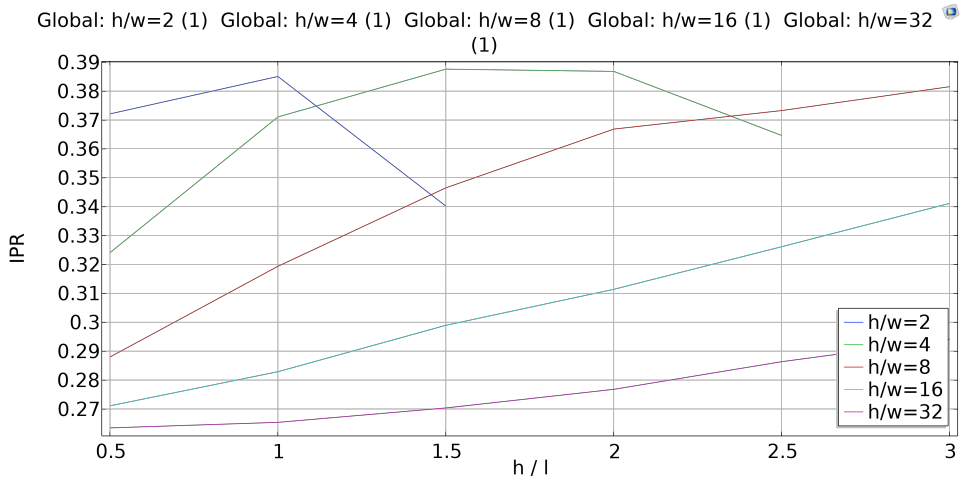

Figure 3.5: IPR values from axial strain test of the star-shaped unit-cell

3.3. Bending of a long metaplate

In Figure 3.7 the observed BPR can be seen, for an increasingly long metaplate. The observed BPR for the alternative geometry of $l = 4mm$, $h = 3mm$, $w = 0.5mm$ can be seen in Figure 3.8. A visualisation of the different metaplate lengths can be seen in Figure 3.9. The double curvature at the symmetry axis of three different lengths can be observed in Figure 3.10. It can be seen that the stress distribution inside the metaplate varies at different lengths of metaplate.

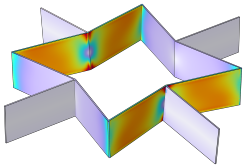

(a) Most thin-walled unit-cell used in Figure 3.4

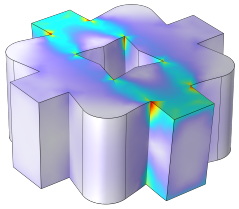

(b) Most thick-walled unit-cell used in Figure 3.4

Figure 3.6: Visualisation of the extremes with respect to relative wall thickness w/l

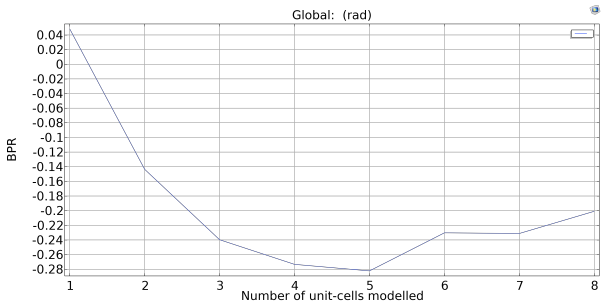

Figure 3.7: BPR development for an increasingly long metaplate, with an expected BPR of -0.275 from cylindrical bending test

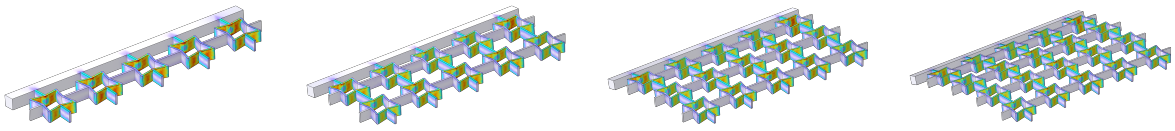

(a) one unit-cell **(b)** **(c)** **(d)**

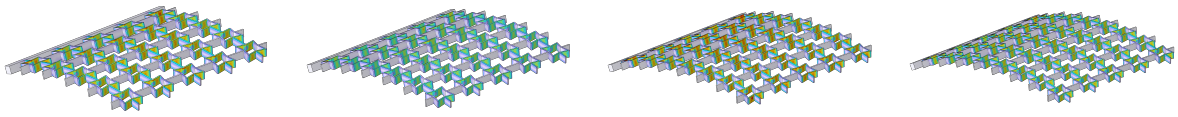

(e) **(f)** **(g)** **(h)**

Figure 3.9: Long metaplate image

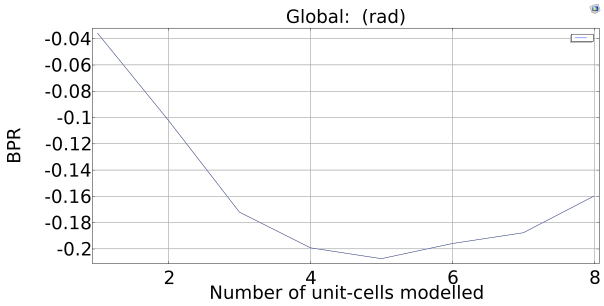

Figure 3.8: BPR development for an increasingly long metaplate (alternative geometry), with an expected BPR of -0.221 from the cylindrical bending test

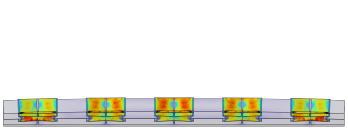

(a) Double curvature at two unit-cells length

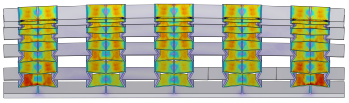

(b) Double curvature at five unit-cells length

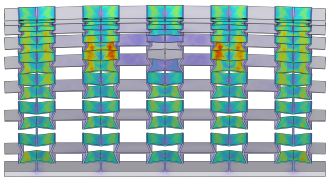

(c) Double curvature at eight unit-cells length

Figure 3.10: Development of double curvature as seen from the symmetry plane

4

Discussion

This study aims to analyse the bending-induced double curvature in metaplates, using multiple modelling approaches in FEA. Modelling the actual detailed metaplates leads to accurate results. However, the modelling of detailed metaplates is computationally heavy and inefficient, as the metaplates are constructed out of tessselated i.e. repeating unit-cells. Homogenisation of metaplates can be used to obtain generalised material properties that describe the overall behaviour of the metaplate using information from a RVE. Homogenisation of a metaplate as a Cauchy continuum only uses six load cases to determine these generalised material properties and this can lead to inaccuracies regarding the bending-induced double curvature of metaplates. By using additional load cases specifically for out-of-plane bending, and homogenising and modelling the metaplate as a Cosserat continuum, these inaccuracies could be resolved. The detailed metaplate can be compared to the homogenised Cauchy continuum metaplate and the homogenised Cosserat continuum metaplate to evaluate if these models can accurately describe the bending-induced double curvature of the detailed metaplate.

4.1. Comparison metaplates

In Figure 3.5 and Equation 2.25 it was shown that the star-shaped unit-cell has a positive IPR. The detailed metaplate and the cylindrical bending test have shown that the star-shaped unit-cell has a negative BPR, as can be seen in Table 3.1. In a Cauchy continuum this is not possible, as Poisson's ratio, measured as IPR through load cases, determines both the in-plane response and the out-of-plane bending response of the homogenised continuum. In Figure 3.1 it can therefore be seen that the corresponding homogenised Cauchy continuum model bends anticlastically instead of synclastically like the detailed metaplate. The corresponding Cosserat model is able to have different values for IPR and BPR, which was shown in Figure 2.16 and Figure 2.17. The homogenised Cosserat continuum model bends synclastically just like the detailed metaplate. The BPR value of the detailed metaplate is similar to the BPR obtained from the cylindrical bending test, for the star-shaped unit-cell. This seems to indicate that the cylindrical bending test could be used as a method to evaluate the bending-induced double curvature for star-shaped metaplates.

The anti-tri-chiral unit-cell was shown to have a negative IPR through Figure 2.12. Through the detailed metaplate it was shown that the BPR of the anti-tri-chiral unit-cell is positive. the corresponding homogenised Cauchy continuum model displays synclastic double curvature due to the negative IPR, while the corresponding homogenised Cosserat continuum model has anticlastic double curvature like the detailed metaplate. The orthorhombic RVE of the anti-tri-chiral unit-cell has only one symmetry plane, so modelling the metaplate using two symmetry planes is not correct. This oversight, does highlight the effect that the type of unit-cell has on the required modelling approach. The BPR of the detailed metaplate of the anti-tri-chiral unit-cell is 0.837, which is a lot higher than the result of the cylindrical bending test of the anti-tri-chiral unit-cell. The bending section of the D-matrix is not symmetric indicates that the cylindrical bending tests did not properly work for the anti-tri-chiral unit-cell, to derive the the bending part of the D-matrix and the BPR. The observed BPR of 0.837 for the detailed metaplate is similar to the BPR of honeycomb metaplates. This can be explained by the fact that the cylindrical sec-

tions of the anti-tri-chiral unit-cell are a lot stiffer in bending, than the connecting flexures. This results in the fact that the bending behaviour of the anti-tri-chiral metaplate reduces to the bending behaviour of a standard honeycomb metaplate. This effect was also described by Alderson et al.[5].

For both the star-shaped unit-cell and the anti-tri-chiral unit-cell, the homogenised Cauchy continuum model is smoother than the homogenised Cosserat continuum model, while both models have an identical mesh size. The deformation defects and lack of smoothness are an indication that something in the model is not working correctly. From Figure 2.17, it was also observed that the smoothness of the model was influenced by the IPR, which should not be the case. This lack of smoothness could be a result of the flawed method of applying a moment. Also it could be a result of the fact that the Cosserat continuum is not fully characterised. The homogenised Cosserat continuum model of the anti-tri-chiral unit-cell has more deformation defects than the homogenised Cosserat continuum model of the star-shaped unit-cell. This is likely because the Cosserat elasticity tensor of the anti-tri-chiral unit-cell is not symmetric, while the Cosserat elasticity tensor of the star-shaped unit-cell is symmetric. As mentioned previously, literature states that the Cosserat elasticity tensor should be symmetric[27][14][15]. The observation that the homogenised Cosserat continuum model with a symmetric elasticity tensor has less deformation defects, than the homogenised Cosserat continuum model with an asymmetric elasticity tensor seems to confirm this. The Cosserat continuum model requires further refinement before it can be actually applied in a more meaningful way. This research could act as stepping stone for further research to build upon.

4.2. Influence of geometry on IPR and BPR

In Figure 3.4, the influence of h/l and h/w on the BPR, from the cylindrical bending test can be seen. For this research, it was decided to focus on a range of h/l between 0.5 and 3. Below 0.5 the unit-cells have a low bending stiffnes compared to higher values of h/l and the applicability to engineering problems might be limited. For h/l above 3 it becomes difficult to have a low enough height h so that the the metaplate remains plate shaped, while having a wall thickness that is thick enough to be produced. The resulting h/l can be compared to Eskandari et al.[14] as the star-shaped unit-cell was included in this research. In the research of Yao et al.[15] the star-shaped unit-cell was also considered. However, the ratio h/l is varied between 0.0025 and 0.1, where w/l is kept constant at 0.025 as to keep the thin-walled assumptions of Euler-Bernoulli beam theory valid[15]. For this research the interest lies in higher values of h/l, as mentioned earlier. Eskandari et al.[14] varied h/l from approximately 0.7 to 7. In the respective graph from Eskandari et al.[14] the values 0.2 to 2 are used, due to a different definition of the length elements. Eskandari et al.[14] kept the IPR of the unit-cell constant, with the star-shaped unit-cell having an IPR of 0.28. The point where the BPR is zero is at roughly $h/l = 2.1$ in the graph of Eskandari et al. In Figure 3.5 it can be seen that $h/w = 32$ has an IPR of roughly 0.28. In Figure 3.4 it can be seen that $h/w = 32$ goes through zero at around $h/l = 2.1$. This seems to match with the results of Eskandari et al.[14]. However, no information about flexure width is provided in the research of eskandari et al.[14], so it cannot be evaluated of the exact same relations are used.

From Figure 3.4 and Figure 3.5, it can be observed that different combinations of IPR and BPR are possible. In previous research the effects of flexure width w were not explored. However, one could argue that this is an important parameter, as it has a great influence on the reproducibility of the metaplate. For standard FDM 3D printers the width of one line is $0.5mm$. If for a certain size of unit-cell the flexure width is $0.5mm$, then the only way to scale that unit-cell down further is by keeping the width constant and therefore making the unit-cell less thin-walled. As the unit-cell becomes less thin-walled, the allowable strain decreases. This is because otherwise the yield stress is exceeded. For metaplates and metamaterials in general miniaturisation is a critical aspect, as this makes it possible for metamaterials to eventually be used like standard engineering materials. Through the application of load cases of this research, thin-walled approximations often made in literature were circumvented.

4.3. Cosserat continuum

Cosserat elasticity is an expansive and complex subject. The application of Cosserat theory to metaplates has obvious benefits, but fully characterising the Cosserat elasticity tensor is a significant challenge. For this research the scope was limited to focus specifically on how Cosserat elasticity can be used regarding the bending-induced double curvature of metaplates. Assumptions were made and

errors in the method were observed. Careful evaluation of these might help guide further research.

To correctly model the anti-tri-chiral unit-cell as a Cosserat continuum, the possible additional couplings have to be determined. The resulting couplings would have to be added to the Cosserat elasticity tensor. If axial to bending, shear to bending or rotation to bending couplings are present for the anti-tri-chiral unit-cell, then the B-matrix can no longer be assumed to be zero. In Figure 2.8 the influence of the B-matrix can be seen. The asymmetric stress tensor becomes influenced by couple strains and the couple stress tensor becomes influenced by the strains.

Due to the scope of this research, the Cosserat continuum model was made specifically for the modelling of bending behaviour. The complete Cosserat elasticity tensor was not characterised. For instance, the torsional response of the metaplate has not been taken into consideration. This means that if a torque is applied, the Cosserat continuum model will not be able to accurately model this. In-plane bending has also not been taken into account. Also the Cauchy symmetric shear constants were assumed to be equal to the asymmetric shear constants. To take these additional responses into account would require additional load cases in combination with a method to extract the elastic constants from these load cases. For this research it was decided to focus on specifically out-of-plane bending, as from these load cases the BPR can be obtained. In addition, this model is made for achiral and anti-chiral unit-cells. For other symmetry groups and chiral unit-cells additional couplings are present, which would require even more additional load cases to characterise the Cosserat elasticity tensor. The full characterisation of a Cosserat continuum is difficult and has only been done for a small number of materials[17].

In COMSOL Multiphysics plates can be modelled in the 2D environment with the plate physics node. Originally it was intended to uses the plate physics node in combination with the weak form. Plate theory is often used in research of metaplates, so its application in this research would align this research more closely with previous works like that of Soest[11]. The reasoning behind why this has not been done is related to the application of the weak form and how the plate physics node works. The plate physics node is based on a Linear Elastic Material node, which assumes a Cauchy continuum. To convert this into a Cosserat continuum would require an approach similar to Jeong et al.[21], where the Cauchy stress tensor is turned into an asymmetric stress tensor through a Cosserat couple modulus μ_c. However for this research the couple modulus was not determined. A different approach was used using two weak forms more similar to the method proposed by Rezaei et al.[18]. This approach cannot be applied to the plate physics node in COMSOL Multiphysics.

In process of determining the Cosserat elasticity tensor, an oversight was made regarding the shear elastic constants obtained from the Cauchy homogenisation. In a Cauchy continuum the shear strain is only related to the partial derivative of displacement, while in a Cosserat continuum the shear strain is also a function of the microrotations. This is depicted in Figure 2.8, where it can be seen that both u and a have an arrow towards shear strain. It was wrongly assumed that the shear elastic constants obtained from the Cauchy homogenisation could be used for the homogenised Cosserat elasticity tensor. To obtain the actual shear elastic constants, load cases for shear should be added where both the strain due to displacement and strain due to microrotations can be obtained. In research by Rezaei et al.[18] a FEA method was proposed to obtain these shear elastic constants. Also in recent research by Bets[29], experimental testing of the Cosserat elastic constants in-plane was performed, which included shear tests.

From these shear tests it might be possible to obtain the couple modulus μ_c. If the couple modulus is known, then a weak form model more similar to Jeong et al. could be made[21]. Here only one weak form physics node has to be added for the microrotations, as the displacements could be handled through a Linear Elastic Material, which is present for most physics nodes. This includes the Plates physics node. In the research by Jeong et al.[21] material isotropy is assumed, which cannot be assumed for metaplates. In further research, these shear tests could be used as starting points to obtain Cosserat elastic constants for shear. From this it might be possible to create a Cosserat continuum that can be added to a Plate physics node in COMSOL Multiphysics. These steps could make it possible to make a homogenised Cosserat plate model.

4.4. Bending of a long metaplate

In Figure 3.7 and Figure 3.8 an interesting pattern can be observed. Initally the observable BPR increases as the metaplate length increases, which is expected as the distance to the rigid boundary condition increases. This allows for the development of double curvature. However, after five unit-cells the observed Poisson's ratio decreases again. The COMSOL Multiphysics model uses symmetry so the total size of the metaplate in this case would be ten unit-cells by five unit-cells. This behaviour happens for both unit-cell geometries that were tested. The displayed behaviour might be linked to the total metaplate proportions, where as the metaplate becomes longer, the relative width to length becomes smaller. The influence of metaplate width on double curvature has been analysed by Mirzaai et al.[7]. Further research is recommended where both the length and width of the metaplate are varied.

4.5. Further recommendations for future research

The homogenised Cosserat continuum model is able to seperate the IPR and BPR of metaplates unlike, the homogenised Cauchy continuum model. However the Cosserat continuum requires further refinement before it can be actually applied in a meaningful way. This research could act as stepping stone for further research

Experimental validation of the bending-induced curvature of metaplates was not in the scope of this research. Applying pure bending to a (meta)plate is challenging as it requires applying a moment along an edge, without restricting the double curvature along this edge. Specifically experimentally validating the exact double curvature is difficult. Further research can be done, regarding the influence of loading conditions on the presence of bending-induced double curvature in metaplates. The cylindrical shaped bending test of an RVE, performed in COMSOL Multiphysics for this research, might be feasible to experimentally validate. Specifically, if a convenient RVE size like a single star-shaped unit-cell is chosen. In this case four connection points can be used to apply moments. Here it does not matter that the application of a bending moment also clamps the unit-cell, as for a single unit-cell this does not influence the double curvature.

In Figure 3.4 it was presented how the geometry of the unit-cell flexure influenced the BPR obtained from the cylindrical bending test. Yao et al. stated that the BPR depends on the "competitive interaction between axial torision and out-of-plane bending"[15]. In future research unit-cells could be designed to have an increased torsional stiffness compared to the bending stiffness. The bending-induced double curvature of the unit-cells could be analysed, to see how the bending-induced double curvature changes. The torsional stiffness can be increased by for instance adding triangular reinforcements to the flexures.

5

Conclusion

In this research, steps were taken to create and compare modelling methods of metaplates for two types of unit-cell. Principles of a Cauchy continuum regarding symmetry and bending were handled. Also an introduction of Cosserat elasticity was given. Two metaplates of interest, namely the star-shaped unit-cell and the anti-tri-chiral unit-cell were selceted as these display an interesting combination of in-plane Poisson's ratio and bending-induced double curvature. For both unit-cells, two sizes of Representative Volume Elements (RVE's) were chosen to see if this would affect the results.

Using Cell periodicity in COMSOL Multiphysics, homogenised Cauchy elasticity matrices were determined for both unit-cells, for different mesh and RVE sizes. The Cauchy elasticity tensor included unexpected couplings. However most of these couplings were insignificant. A significant axial to shear out-of-plane coupling was found for the star-shaped unit-cell and the anti-tri-chiral-unit-cell. Additionally, for the anti-tri-chiral unit-cell a significant axial to shear coupling in-plane was found. The resulting elasticity matrices were validated by calculating the Mean Average Percentage Error (MAPE) of the mesh convergence and the RVE size. The mesh size could be further increased to improve the MAPE value. It was observed that RVE size had no significant effect on the Cauchy elasticity tensor, conforming that the smaller RVE's were actual Representative Volume Elements.

To extend the homogenised Cauchy continuum model to a homogenised Cosserat continuum model, additional load cases were applied in the form of cylindrical bending tests through COMSOL Multiphysics. From these cylindrical bending tests the estimated bending-induced double curvature and the bending part of the D-matrix were determined. Due to the symmetry of the star-shaped unit-cell, the cylindrical bending test only had to be performed in one direction. The cylindrical bending test of the star-shaped unit-cell was performed for different RVE and mesh sizes. For the anti-tri-chiral unit-cell, the cylindrical bending test was performed in two perpendicular directions for different mesh sizes. The bending parts of the D-matrix were validated by calculating the MAPE of the mesh convergence and the RVE size. For the star-shaped unit-cell, all MAPE values were low indicating mesh convergence and that the mesh size had no significant effect on the bending part of the D-matrix. The bending-induced double curvature value obtained from the cylindrical bending test of the star-shaped unit-cell was similar to the bending-induced curvature value of the actual detailed star-shaped unit-cell metaplate. For the anti-tri-chiral unit-cell the resulting bending part of the D-matrix became asymmetric. This indicates that additional couplings might be present, or that the RVE was not properly constrained.

A Cosserat continuum model for bending was created throught the weak form of COMSOL Multiphysics. It was validated that the Cosserat continuum model could display different types of bending-induced double curvature, independently from the in-plane Poisson's ratio. However, a lack of smoothness was observed in the Cosserat continuum model.

The bending-induced double curvature of the actual detailed metaplate was compared to the homogenised Cauchy continuum metaplate and the homogenised Cosserat continuum metaplate. This was done for both the star-shaped unit-cell and the anti-tri-chiral unit-cell. The homogenised Cauchy and Cosserat continuum models were not properly setup to account for the symmetry of the anti-tri-chiral unit-cell.

The homogenised Cosserat continuum model did determine the correct amount of bending-induced double curvature for both unit-cells, unlike the homogenised Cauchy continuum model. However, surface defects and a lack of smoothness indicate that further refinement of the cosserat continuum model is required to accurately model the bending-induced double curvature of metaplates.

Using the cylindrical bending test, a parametric sweep was performed in COMSOL Multiphysics for the star-shaped unit-cell, where the influence of the flexure geometry was related to the estimated bending-induced double cuvature. This revealed how specific values of bending-induced double curvature can be obtained using different flexure geometries. Also a parametric sweep was performed in COMSOL Multiphysics to evaluate the development of bending-induced double curvature for an increasingly long metaplate with rigid ends. While the bending-induced double curvature initially increased, from a certain length the bending-induced double curvature started to decrease. Experimentally validating the results of the long metaplate could be interesting for future research. Additionally other experimental ideas for future research were proposed.

This Research combined the bending-induced double curvature of metaplates with the continuum mechanics of Cauchy and Cosserat elasticity. Cosserat elasticity is a promising tool for metaplates to more accurately model bending-induced double curvature. However, its application remains challenging.

References

[1] K. Bertoldi, V. Vitelli, J. Christensen, and M. V. Hecke, "Flexible mechanical metamaterials," *Nature Reviews Materials 2017 2:11*, vol. 2, pp. 1–11, 11 Oct. 2017, ISSN: 2058-8437. DOI: 10.1038/natrevmats.2017.66. [Online]. Available: https://www.nature.com/articles/natrevmats201766.

[2] R. L. Magna and J. Knippers, "Tailoring the bending behaviour of material patterns for the induction of double curvature," *Humanizing Digital Reality*, pp. 441–452, 2018. DOI: 10.1007/978-981-10-6611-5_38.

[3] K. E. Evans, "The design of doubly curved sandwich panels with honeycomb cores," *Composite Structures*, vol. 17, pp. 95–111, 2 Jan. 1991, ISSN: 0263-8223. DOI: 10.1016/0263-8223(91)90064-6.

[4] Y. Sakai and M. Ohsaki, "Optimization method for shape design of auxetic bending-active gridshells using discrete differential geometry," *Structures*, vol. 34, pp. 1589–1602, Dec. 2021, ISSN: 2352-0124. DOI: 10.1016/J.ISTRUC.2021.08.067.

[5] A. Alderson, K. L. Alderson, G. Chirima, N. Ravirala, and K. M. Zied, "The in-plane linear elastic constants and out-of-plane bending of 3-coordinated ligament and cylinder-ligament honeycombs," *Composites Science and Technology*, vol. 70, pp. 1034–1041, 7 Jul. 2010, ISSN: 0266-3538. DOI: 10.1016/J.COMPSCITECH.2009.07.010.

[6] J. Huang, Q. Zhang, F. Scarpa, Y. Liu, and J. Leng, "Bending and benchmark of zero poisson's ratio cellular structures," *Composite Structures*, vol. 152, pp. 729–736, Sep. 2016, ISSN: 0263-8223. DOI: 10.1016/J.COMPSTRUCT.2016.05.078.

[7] M. J. Mirzaali, A. Ghorbani, K. Nakatani, *et al.*, "Curvature induced by deflection in thick metaplates," *Advanced Materials*, vol. 33, 30 Jul. 2021, ISSN: 15214095. DOI: 10.1002/adma.202008082.

[8] A. Tabak, B. Safaei, A. Memarzadeh, S. Arman, and C. Kizilors, "An extensive review of piezoelectric energy-harvesting structures utilizing auxetic materials," *Journal of Vibration Engineering & Technologies 2023 12:3*, vol. 12, pp. 3155–3192, 3 Jun. 2023, ISSN: 2523-3939. DOI: 10.1007/S42417-023-01038-9. [Online]. Available: https://link.springer.com/article/10.1007/s42417-023-01038-9.

[9] W. J. Ferguson, Y. Kuang, K. E. Evans, C. W. Smith, and M. Zhu, "Auxetic structure for increased power output of strain vibration energy harvester," *Sensors and Actuators A: Physical*, vol. 282, pp. 90–96, Oct. 2018, ISSN: 0924-4247. DOI: 10.1016/J.SNA.2018.09.019. [Online]. Available: https://www.sciencedirect.com/science/article/pii/S0924424718311105.

[10] F. Ebrahimian, Z. Kabirian, D. Younesian, and P. Eghbali, "Auxetic clamped-clamped resonators for high-efficiency vibration energy harvesting at low-frequency excitation," *Applied Energy*, vol. 295, p. 117 010, Aug. 2021, ISSN: 0306-2619. DOI: 10.1016/J.APENERGY.2021.117010. [Online]. Available: https://www.sciencedirect.com/science/article/pii/S0306261921004773.

[11] A. M. J. V. Soest, "Analyzing out-of-plane deformations caused by varying poisson ratio distributions in a metamaterial," M.S. thesis, Delft University of Technology, 2023. [Online]. Available: http://repository.tudelft.nl/..

[12] D. H. Chen, "Bending deformation of honeycomb consisting of regular hexagonal cells," *Composite Structures*, vol. 93, pp. 736–746, 2 Jan. 2011, ISSN: 0263-8223. DOI: 10.1016/J.COMPSTRUCT.2010.08.006.

[13] D. H. Chen, "Equivalent flexural and torsional rigidity of hexagonal honeycomb," *Composite Structures*, vol. 93, pp. 1910–1917, 7 Jun. 2011, ISSN: 0263-8223. DOI: 10.1016/J.COMPSTRUCT.2011.02.009.

[14] S. Eskandari, B. shahryari, and A. Akbarzadeh, “Unravelling size-dependent and coupled properties in mechanical metamaterials: A couple-stress theory perspective,” *Advanced Science*, vol. 11, p. 2 305 113, 13 Apr. 2024, ISSN: 2198-3844. DOI: 10.1002/ADVS.202305113. [Online]. Available: https://onlinelibrary.wiley.com/doi/full/10.1002/advs.202305113%20https://onlinelibrary.wiley.com/doi/abs/10.1002/advs.202305113%20https://onlinelibrary.wiley.com/doi/10.1002/advs.202305113.

[15] Y. Yao, Y. Ni, and L. He, “Unexpected bending behavior of architected 2d lattice materials,” *Science Advances*, vol. 9, 25 2023, ISSN: 23752548. DOI: 10.1126/SCIADV.ADG3499/SUPPL_FILE/SCIADV.ADG3499_SM.PDF. [Online]. Available: https://www.science.org/doi/10.1126/sciadv.adg3499.

[16] L. Steinberg and R. Kvasov, *Cosserat Plate Theory*. CRC Press, 2023.

[17] S. Hassanpour and G. R. Heppler, *Micropolar elasticity theory: A survey of linear isotropic equations, representative notations, and experimental investigations*, Feb. 2017. DOI: 10.1177/1081286515581183.

[18] A. Rezaei, R. Izadi, and N. Fantuzzi, “Equivalent micropolar model for porous guided bone regeneration mesh: Optimum design for desired mechanical properties,” *Applied Mathematical Modelling*, vol. 131, pp. 737–763, Jul. 2024, ISSN: 0307-904X. DOI: 10.1016/J.APM.2024.04.008.

[19] A. Rezaei, R. Izadi, and N. Fantuzzi, “Equivalent micropolar model for porous guided bone regeneration mesh: Optimum design for desired mechanical properties,” *Applied Mathematical Modelling*, vol. 131, pp. 737–763, Jul. 2024, ISSN: 0307-904X. DOI: 10.1016/J.APM.2024.04.008.

[20] R. Masiani and P. Trovalusci, “Cosserat and cauchy materials as continuum models of brick masonry,” *Meccanica*, vol. 31, pp. 421–432, 4 1996, ISSN: 00256455. DOI: 10.1007/BF00429930.

[21] J. Jeong, H. Ramezani, and E. Spéciale, *Implementation of the finite isotropic linear cosserat models based on the weak form*, 2008. [Online]. Available: http://www.ce.berkeley.edu/.

[22] S. Sorohan, D. M. Constantinescu, M. Sandu, and A. G. Sandu, “On the homogenization of hexagonal honeycombs under axial and shear loading. part i: Analytical formulation for free skin effect,” *Mechanics of Materials*, vol. 119, pp. 74–91, Apr. 2018, ISSN: 0167-6636. DOI: 10.1016/J.MECHMAT.2017.09.003.

[23] A. Catapano and M. Montemurro, “A multi-scale approach for the optimum design of sandwich plates with honeycomb core. part i: Homogenisation of core properties,” *Composite Structures*, vol. 118, pp. 664–676, 1 Dec. 2014, ISSN: 0263-8223. DOI: 10.1016/J.COMPSTRUCT.2014.07.057.

[24] C. Mittelstedt, *Theory of Plates and Shells*. Springer, 2023.

[25] S.Timoshenko and S. Woinowsky-Krieger, *Theory of Plates and Shells*. McGRAW-HILL BOOK COMPANY, INC., 1959.

[26] Z. Cui and J. Ju, “Mechanical coupling effects of 2d lattices uncovered by decoupled micropolar elasticity tensor and symmetry operation,” *Journal of the Mechanics and Physics of Solids*, vol. 167, p. 105 012, Oct. 2022, ISSN: 0022-5096. DOI: 10.1016/J.JMPS.2022.105012.

[27] Z. Cui, Z. Yuan, and J. Ju, *Mechanical couplings of 3d lattice materials discovered by micropolar elasticity and geometric symmetry*, 2022.

[28] R. D. Gauthier and W. E. Jahsman, *A quest for micropolar elastic constants 1*, 1975. [Online]. Available: http://asme.org/terms.

[29] B. Bets, “Experimental validation of micropolar elastic constants for two-dimensional chiral mechanical metamaterials,” M.S. thesis, Delft University of Technology, 2025. [Online]. Available: https://resolver.tudelft.nl/uuid:e73ddddf-b31f-4e68-8ca0-6b0da45e67f6.

A

Additional results

Additional images of the load cases with normal mesh size.

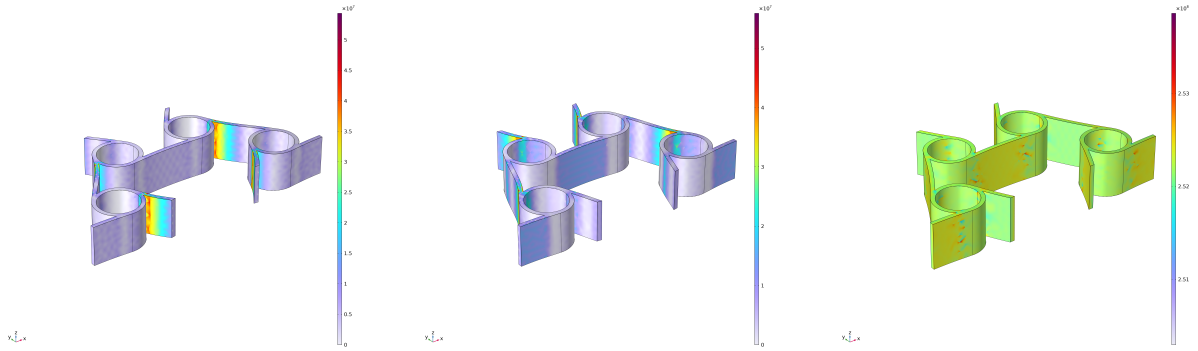

(a) principal strain x **(b)** principal strain y **(c)** principal strain z

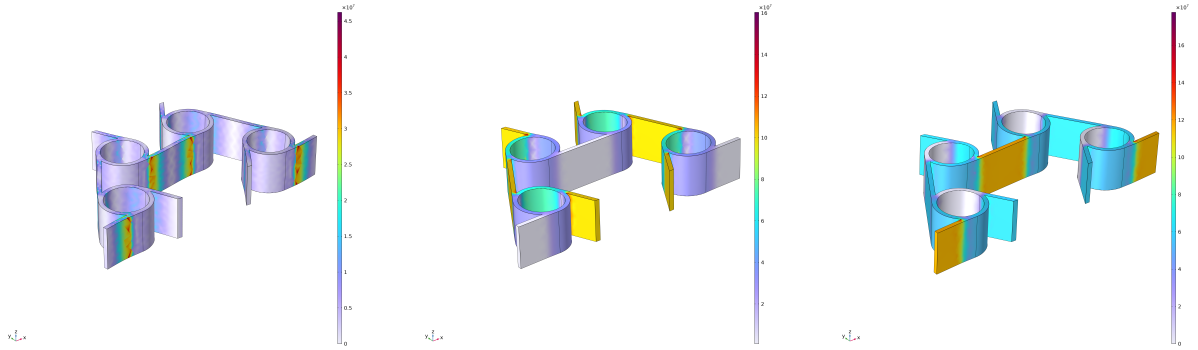

(d) shear strain xy **(e)** shear strain yz **(f)** shear strain xz

Figure A.1: six load cases applied to RVE of the anti-tri-chiral unit-cell with normal mesh

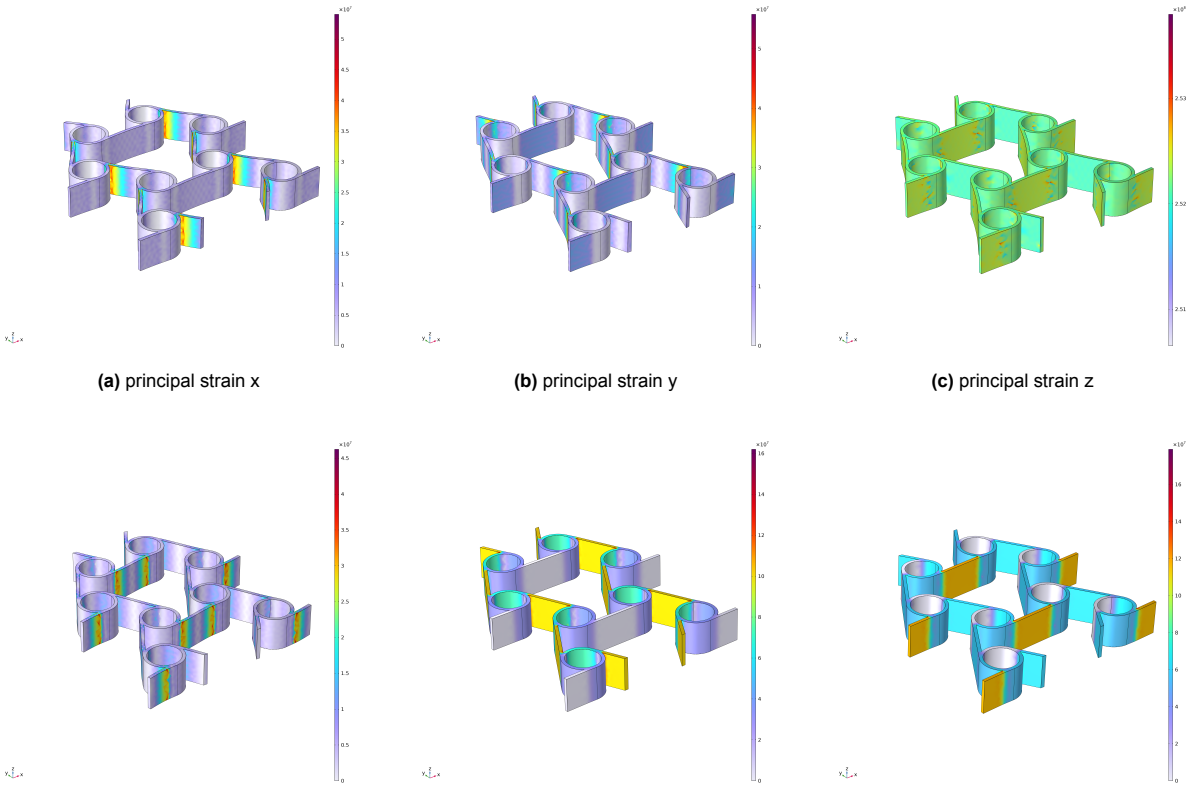

(a) principal strain x **(b)** principal strain y **(c)** principal strain z

(d) shear strain xy **(e)** shear strain yz **(f)** shear strain xz

Figure A.2: six load cases applied to alternative RVE of the anti-tri-chiral unit-cell with normal mesh

Bending-induced double curvature in metaplates; bridging the gap between model and experiment

A literature review regarding the bending of metaplates

by

Pieter Jager

Abstract:

For a long time, it was assumed that the bending-induced double curvature of metamaterial plates (metaplates) could be tailored by adjusting their Poisson's ratio, with the assumption that these structures could be accurately modelled as continuous (Cauchy) plates. However, recent studies have challenged this view, revealing that such assumptions remain valid only under specific conditions. In this literature review, state of the art modelling approaches for the bending-induced double curvature of metaplates are analyzed, as well as how these approaches could be implemented for future research.

Thesis Committee:	Freek Broeren, TU Delft, daily supervisor
Project Duration:	June, 2024 - August, 2025
Faculty:	Mechanical Engineering, High-Tech, Delft

TU Delft

Contents

Nomenclature

Here abbreviations and symbols are stated to prevent possible confusion during reading.

Abbreviations

Abbreviation	Definition
AAH	Augmented Asymptotic Homogenisation
BPR	Bending Poisson's Ratio (or Mindlin's ratio)
CSPT	Couple-Stress Plate Theory
IPR	In-plane Poisson's Ratio
MPR	Material Poisson's Ratio

Symbols

Symbol	Definition	Unit
ϵ	Strain	-
ζ	Mindlin's ratio	-
θ	Angle in unit-cell	rad
κ	Curvature	rad
ν	Poisson's ratio	-
σ	Stress	Pa
ϕ	load direction	rad

1

Introduction

Metamaterials are a special type of architected materials that are able to achieve properties not commonly found in nature or from standard engineering materials[1]. Metamaterials make use of the geometry of their unit-cells to attain these unique properties. In this context, the unit-cell is a (compliant) mechanism that is tesselated to create the metamaterial. Here, tesselation refers to the operation of repeating a pattern. A tile for example, could be Tesselated to create a tiled floor. Tesselation of a unit-cell can be done in one, two or three perpendicular directions, which will determine in which dimensions the metamaterial will actually exhibit this unique property. A unit-cell tesselated in 2 perpendicular directions should behave like a two dimensional metamaterial.

Metamaterials can be divided into wave-based metamaterials and mechanical metamaterials. Wave-based metamaterials display unique properties related to optics, acoustics and thermics, while mechanical metamaterials display unique properties related to motion, deformation, stresses and mechanical energy[1]. For the scope of this literature review only mechanical metamaterials are of interest. A prominent type of mechanical metamaterials are metamaterials with a negative Poisson's ratio, which Soest's literature review[2] stated was the most researched type of mechnanical metamaterial. Negative Poisson's ratio metamaterials are prevelant in literature (as can also be seen in several overview papers[1][3][4]), but there are still a lot of gaps in the knowledge about these metamaterials.

In studies about negative Poisson's ratio metamaterials, the out-of-plane bending is often not taken into consideration, as it falls outside the scope of their research. Literature about this aspect is therefore limited[5] and mostly concentrated around a few negative Poisson's ratio metamaterial designs like the auxetic honeycomb pattern. The out-of-plane bending of metamaterials can be analysed by looking at a plate shaped metamaterial (metaplate), where the length and width are much greater than the height. Here, the unit-cells of the metamaterial only have to be tesselated along the length and width of the plate as the height is negligibly small.

This literature review focusses on the double curvature that negative Poisson's ratio metaplates exhibit when they are bent out-of-plane. This is of interest, because for continuous materials the Poisson's ratio is related to the bending-induced double curvature. If this is also applicable to metaplates, then complexly curved metaplates could be made by varying the Poisson's ratio in the metaplate[2]. As this literature review focusses specifically on negative Poisson's ratio and zero Poisson's ratio mechanical metamaterial plates, these will be referred to as metaplates.

An important goal for metamaterials is their usage in the design process like regular materials. Generalised properties should define the behaviour and knowledge of the underlying microstructure of the metamaterial should not be required. If a metamaterial can be modelled as a continuous material that approximately has the same properties, then the metamaterial could be used in the design process and finite element analysis (FEA) like any other material. A central question about this is:

Is it possible to model current metaplates as continuous plates? If not in general, are there conditions for which this could be possible?

Here it is also of interest if a type of plate theory could be applied, as plate theory is often used for continuous materials to simplify the calculations or modelling. Other possible applications for the bending of metaplates are in areas like shape-fitting, sandwich structure reinforcement and deployable structures. Here the architected nature of metamaterials is of interest to design complex desired shapes. For this it is crucial to find out:

What types and amounts of bending-induced double curvature are currently obtainable using metaplates?

This literature review aims to answer these questions and present possible areas of interest for future research. The process and the findings of the literature retrieval are described in chapter 2. Based on the reviewed literature, the research questions and areas for future research are discussed in chapter 3. Import aspects of the literature review will be summarised in chapter 4.

2

Literature

In the literature section, first the general search strategy is briefly explained in section 2.1. Second, some background principles central to the state of the art are discussed in section 2.2. Third, the current state of the art is presented in section 2.3.

2.1. Search Strategy

The starting point of this literature review were two papers written at the TU Delft by Mirzaali et al.[6] and Soest[2]. Relevant papers referenced by one or both of these papers were analysed to get more insight into the field. The paper written by Mirzaali et al. was published in 2021, so all papers that referenced Mirzaali et al. since then could be looked up. This returned 25 papers, from which papers deemed relevant based on the title and abstract were analysed.

Two of these papers presented novel theories of interest[5][7]. These papers were published in 2023 and 2024 respectively. In one of these recent papers homogenisation was an important aspect of the methodology[7], so additional research into homogenisation methods was done. In the other recent paper Cosserat theory was an important aspect of the methodology[5], so additional research into Cosserat (plate) theory was also done. Only four papers were found that referenced one of these two recent papers. One of these four papers presented a design and categorisation method for metamaterial unit-cells[8] .

In summary, because this literature review is a continuation of previous works, the foundation of this literature review is similar to the literature used in these previous works, namely Soest[2] and Mirzaali et al.[6]. In addition to these, two recently published papers were found[5][7], which introduced additional literature and topics of interest to analyse.

2.2. Background

Here, principles central to metaplates are introduced. First, Poisson's ratio will be explained in subsection 2.2.1, as this is a fundamental concept for everything discussed in this literature review. Next, metamaterials relevant to the state of the art are introduced in subsection 2.2.2. Lastly, a few aspects of plate theory are explained.

2.2.1. Poisson's ratio

A fundamental part of this literature study is Poisson's ratio. Poisson's ratio describes the relation between the deformation in the loading direction (ϵ_{11}) and the deformation perpendicular to this (ϵ_{22}), which can be seen in Equation 2.1 and Figure 2.1[2]. When a beam is compressed in one direction, it tends to expand in the other direction to preserve its volume. Most materials behave like this and therefore have a positive Poisson's ratio (notice the minus sign in Equation 2.1). A beam has a negative Poisson's ratio if it shrinks when it is compressed in a perpendicular direction. Materials with a negative Poisson's ratio are not usually found in nature, but they can be of great use for various (engineering)

applications. For instance, cork is used to seal wine bottles due to its Poisson's ratio of roughly zero[1].

The in-plane behaviour of Poisson's ratio also influences the bending-induced curvature. When a beam is subject to pure bending at two sides, part of the beam will be loaded under compression and the other part will be loaded under tension (see Figure 2.1).For a beam with a positive Poisson's ratio this means that the part loaded under compression will get thicker, and the part loaded under tension will get thinner. This creates a saddle shaped curvature as can be seen in Figure 2.1. For small linear elastic deformations, Poisson's ratio can therefore be used as the ratio of curvature in the direction perpendicular to the applied bending(κ_{22}) and the curvature in the direction bending(κ_{11}) (see Equation 2.1). This means that for a beam or a plate, its Poisson's ratio could be measured in two ways, which should both return the same value.

$$\nu_{12} = -\frac{\epsilon_{22}}{\epsilon_{11}} = -\frac{\kappa_{22}}{\kappa_{11}} \tag{2.1}$$

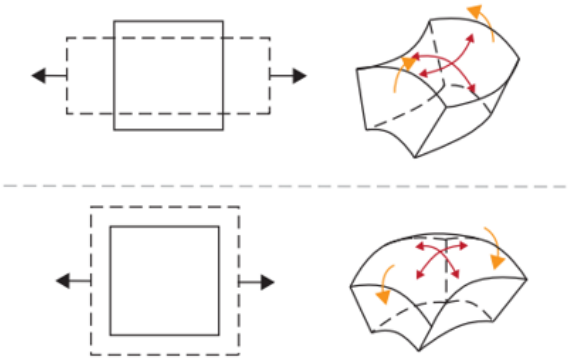

Figure 2.1: Effect of Poisson's ratio in-plane (left) and out of plane (right), for both positive Poisson's ratio (top) and negative Poisson's ratio (bottom)[2]

Materials with a positive Poisson's ratio exhibit anticlastic or saddle shaped curvature, while materials with a negative Poisson ratio exhibit synclastic or dome shaped curvature. Furthermore, materials with zero Poisson's ratio exhibit monoclastic curvature, which all can be seen in Figure 2.2. A more elaborate explanation of this behaviour can be found in the work of van de Sande[9].

Figure 2.2: Possible types of double curvature, from left to right: monoclastic, synclastic and anticlastic[9]

2.2.2. Metamaterials

Metamaterials are a fusion of mechanism and material where the mechanism of the unit-cell gives the metamaterial unusual but desirable bulk properties like a negative Poisson's ratio. With the introduction of metamaterials, the range of attainable Poisson's ratios increased drastically. For negative Poisson's ratio metamaterials the material properties no longer define the Poisson's ratio, but the geometry of the unit-cell does. Here, a unit-cell is a compliant mechanism that can be tesselated in one or multiple dimensions to create a metamaterial. This means that metamaterials can be designed for specific desired Poisson's ratios. To differentiate between the Poisson's ratio of the material and the resulting

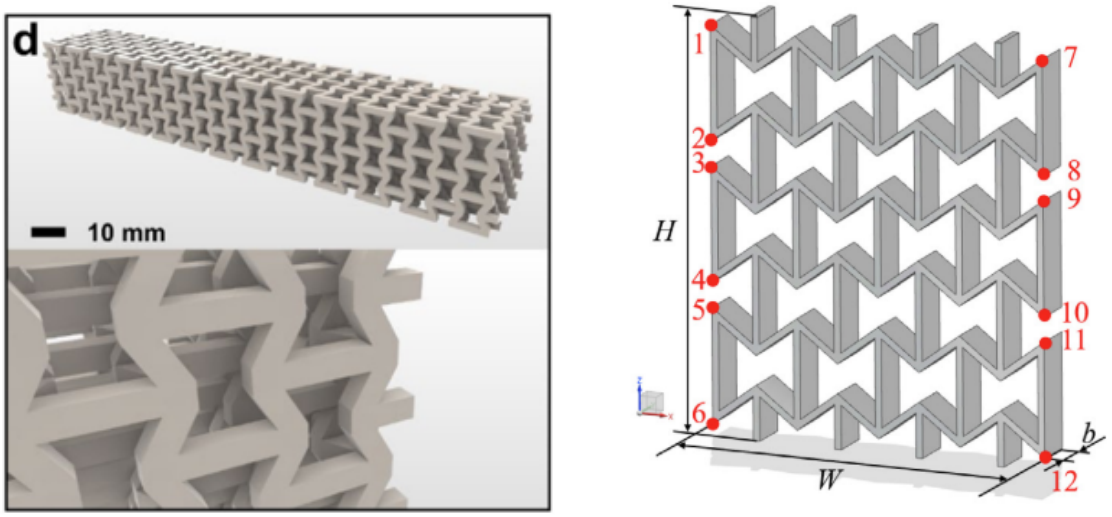

(a) three dimensional auxetic honeycomb metamaterial[10] **(b)** two dimensional auxetic honeycomb metaplate[12]

Figure 2.3: Auxetic honeycomb

metamaterial Poisson's ratio, the Poisson's ratio of the materials was named the Material Poisson's Ratio (MPR) in this literature review.

As previously mentioned, a unit-cell can be tesselated in one to three directions ([10][11] for example). In Figure 2.3a a metamaterial tesselated in three directions is presented. The negative Poisson's ratio of the metamaterial can be observed by compressing the metamaterial in any direction. It can be easily understood that the manufacturing of such a metamaterial is complex, for which modern 3D printing methods are required. Also it is prevalent that Finite Element Analysis (FEA) on such a metamaterial is computationally heavy, if all the individual features in Figure 2.3a are taken into account. If this metamaterial could be modelled as a continuous beam with a negative Poisson's ratio, the FEA would be significantly less computationally heavy.

As previously mentioned, for this literature review the interest lies in so called metamaterial-plates (metaplates), where the unit-cell is tesselated in 2 directions. To make the metaplate three-dimensional the 2D geometry is given a thickness by extruding this geometry, as can be seen in Figure 2.3b. This approach is of interest when the metamaterial is plate shaped, where the size of the tesselated dimensions are far greater than the size of the non-tesselated dimension. Metaplates are made to act like metamaterials in-plane and for bending out-of-plane. While for other out of plane deformations the metaplate does not act like a metamaterial. For instance the metaplate does not act like a metamaterial when the metaplate is compressed from the top and bottom, which is the non-tesselated dimension. This approach can be combined with plate theory, which has often been used for metaplates [6][7]. Plate theory will be discussed in more detail in subsection 2.2.3.

Some interesting unit-cell designs that are relevant when looking at bending-induced curvature are briefly explained. These unit-cells are depicted in Figure 2.4.

(Re-entrant) Honeycomb

Different types of metaplates can have a negative Poisson's ratio. The most famous unit-cell type to achieve this is the re-entrant or auxetic honeycomb (see (b) in Figure 2.4) also sometimes referred to as the bow-tie, which is a variation on the honeycomb design (see (a) in Figure 2.4). The auxetic honeycomb is also depicted Figure 2.3, which was mentioned previously. By enlarging the angle θ of the beams in the honeycomb unit-cell, the honeycomb's Poisson's ratio starts to decrease. The Poisson's ratio approaches zero when the angle approaches $\theta = 90°$ (as it turns into a rectangular unit-cell) and beyond $\theta = 90°$ the Poisson's ratio becomes negative. When the re-entrant honeycomb is compressed from the top and bottom, the angled beams will fold inwards i.e. towards the center of the unit-cell. At $\theta = 90°$ the unit-cell will display buckling, where the direction of buckling will be based on small manufacturing inconsistencies. Because of this, the $\theta = 90°$ geometry is not of interest for this literature

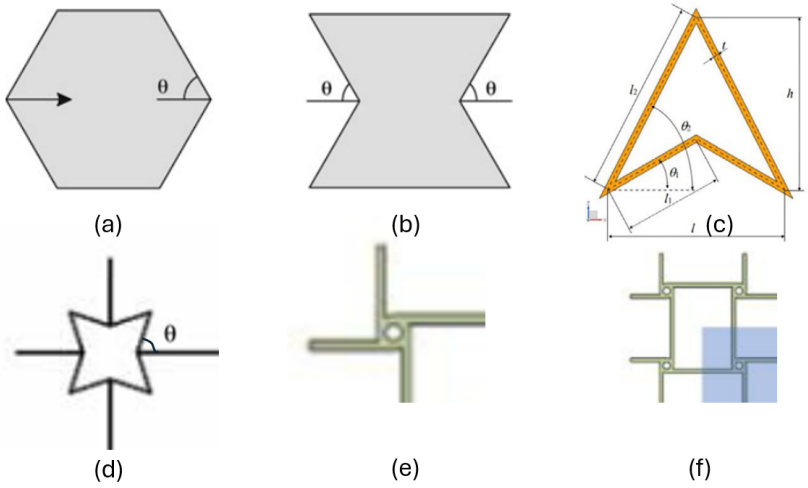

Figure 2.4: Unit-cell designs, (a) honeycomb[13], (b) re-entrant honeycomb[13], (c) Arrow[14], (d) star shape[15], (e) tetra-chiral[16], (f) anti-tetra-chiral[16]

review. Every (re-entrant) honeycomb unit-cell is connected to six other unit-cells, which makes the unit-cell hexagonal. The In-plane behaviour of re-entrant honeycomb metaplates is presented by Jiang et al.[12] and numerous others. Bending-induced curvature of the re-entrant honeycomb has been analysed and tested numerous times [13][17][18][19][20][6]. These papers conclude that the bending behaviour of honeycomb metaplates is in line with plate theory (Kirchhoff-Love for [13][17] and Reissner-Mindlin for [6]), and therefore that by changing the Poisson's ratio the bending-induced curvature can be altered. To utilise and visualise this, honeycomb metaplates were designed which bent around specified shapes by La Magna et al.[13]. Huang et al. presented a re-entrant honeycomb metaplate with zero Poisson's ratio[21]. In 2021 Mirzaali et al. published a paper in which rigorous analysis and testing was performed to evaluate how parameters like the thickness, width, internal angles and wall thickness influenced the bending behaviour of (re-entrant) honeycomb metaplates[6]. This was expanded upon by Eskandari et al. in 2024[7]. In section 2.3 the content of these papers are described in more detail.

Arrow

The auxetic triangle or arrow unit-cell is another type of metaplate that has a negative Poisson's ratio (see (c) in Figure 2.4). The arrow unit-cell works in a similar way as the re-entrant honeycomb, only instead of two sets of angled flexures folding inwards only one set of angled flexure folds inwards. This alters the angles of the 2 flexures connected to the ends of the angled flexures and these flexures connect together at the center of the next set of angled flexures. This means that the arrow unit-cell has less symmetry than the re-entrant honeycomb. The arrow unit-cell is tetragonal, as every unit-cell connects to four other unit-cells. In-plane behaviour has been presented by Jiang et al.[14]. Research into bending-induced curvature of auxetic triange metaplates has been done by Sakai et al.[18].

Star shape

The next unit-cell type of interest is the (tetragonal) star-shaped unit-cell, originally presented by Grima et al.[15]. The star-shaped unit-cell can be seen as a variation on the re-entrant honeycomb unit-cell, adding symmetry in a way that the unit-cell is identical to its 90 degree rotated version. Because of this the Poisson's ratio of the star-shaped metaplate will be identical to the Poisson's ratio measured perpendicularly to it. This relation to the re-entrant honeycomb is detailed by Roberjot et al.[8]. An interesting property of the star-shaped unit-cell is that while it seems auxetic, the Poisson's ratio can be both positive and negative based on the internal angle θ. Yao et al. also presented a variation on the star-shape that is hexagonal[5]. Bending analysis of the star-shaped metaplate has been perfomed by Yao et al.[5], which will be handled in the state of the art section. Variations of the star-shaped unit-cell exist and are shown in [5][8]. The variation most of interest is one where every unit-cell is connected to six other unit-cells instead of four like the unit-cell in Figure 2.4 (d). This variation of the star-shaped unit-cell is more similar to the (re-entrant) honeycomb as it is also hexagonal.

Chiral

Another type of metaplate that can have a negative Poisson's ratio is the chiral metaplate. Chiral unit-cells utilise their asymmetry to rotate under load, which makes their flexures coil around a central cylinder, like a wire around a coil. Due to this asymmetry, chiral unit-cells are either left or right rotating (left or right handed in other words). The main type of chiral unit-cells regarded in this literature is Chiral unit-cells consisting of a cylinder from which multiple flexures point outwards (see (e) of Figure 2.4). A chiral metaplate can have a negative Poisson's ratio, while another chiral metaplate with slightly rotated unit-cells can have a positive Poisson's ratio due to internal couplings[7]. Various papers have analysed and tested the bending-induced curvature of chiral metaplates[22][21] and recently by Eskandari et al.[7]. The results of this will be discussed in more detail in section 2.3. The cylinder at the center of the chiral unit-cell could also be replaced with flexures joined at the center, which was done by Attard et al.[23]. This paper does not present the influence this variation has on the bending-induced curvature.

A variation of a chiral unit-cell is an anti-chiral unit-cell, where every chiral unit-cell is connected with its mirror image. Like mentioned previously, the unit-cell is the smallest 'section' that can be tesselated to create the metaplate. Mirroring is not an operation of tesselation, so a single anti-chiral unit-cell is comprised of multiple mirrored chiral unit-cells. An example of an anti-chiral unit-cell can be seen in Figure 2.4 (f), which is based on the chiral unit-cell in Figure 2.4 (e). Here the unit-cell consists of four chiral unit-cells. Anti-chiral unit-cells are therefor not directional, but consist out of smaller directional sections. Some testing of bending-induced curvature of anti-chiral metaplates has been done[22][21].

The Poisson's ratio of chiral metaplates varies based on the the type of chiral unit-cell and the relation of the length of the flexures relative to the size of the central cylinder (noted as α). Alderson et al.[22] presented a graph which can be seen in Figure 2.5, where some Poisson's ratio values of chiral metaplates are shown. It is interesting to note that some chiral unit-cells can have a positive or negative Poisson's ratio based on α. This clearly shows that chiral unit-cells can have both an auxetic mechanism as well as a non-auxetic mechanism. This is logical because the central cylinder that creates the chiral behaviour can be made negligibly small, so that the chiral unit-cells lose their rotating/chiral behaviour.

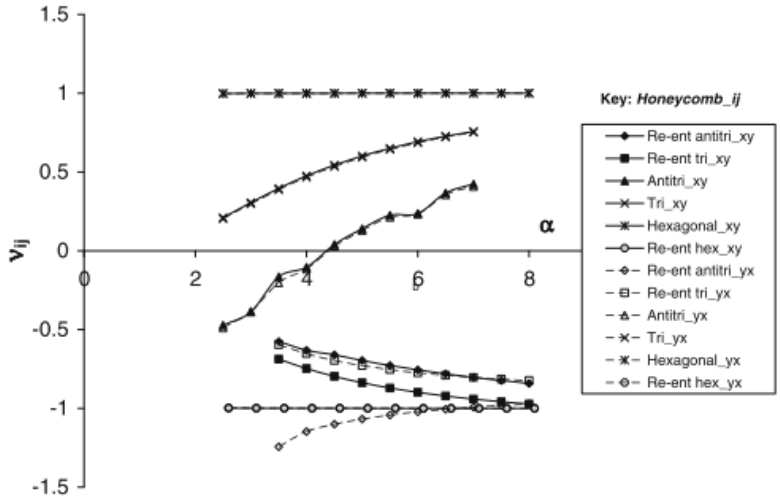

Figure 2.5: Poisson's ratio as a function of α for different chiral and anti-chiral unit-cells[22], where α is the relation between flexure and cylinder lengths

Unit-cells that are not chiral, are called achiral[8]. Anti-chiral unit-cells and all other unit-cells discussed outside the chiral section are classified as achiral.

Categorisation

Different types of categorisation have been performed by Soest, Roberjot et al. and Eskandari et al. [2][8][7]. Soest used Bravais lattice groups based on crystallography, which made distinction of seven crystal types[2]. Roberjot et al. made a system based on how the unit-cell is constructed. Here

the chirality or lack of chirality was a central point of interest[8]. Eskandari et al. also used crystal types, but based on the symmetry of the unit-cell (Curie groups). This resulted in the distinction of 32 crystal classes[7]. For this literature review, the major interest lies in the bending behaviour of the metaplates and not in the design categorisation of the unit-cells itself. However, it is possible that unit-cells categorised in similar groups bend in a similar manner, and therefore these categorisations might help explain results from literature or novel results made during novel research. In the case of Eskandari et al., categorisation into crystal types was used to determine how many unknown parameters should be solved for in his two-dimensional asymptotic homogenisation (2D AAH) method. The relevance of this and further elaboration will be done in subsection 2.3.4.

It is important to note that unit-cells can be depicted in different ways, meaning different looking unit-cells could be tesselated to create the same metamaterial. A widely used definition for the unit-cell is that it represents the smallest geometry that can be tesselated to create the metamaterial or metaplate. However, following this definition the unit-cell of a honeycomb would be a set of 3 flexures pointing outward from a center. For this literature review an attempt was made to depict unit-cells in an intuitive manner based on the depictions in literature and the functioning of the unit-cell. The distinction between tetragonal and hexagonal unit-cells is useful to keep in mind, which simply refers to how many unit-cells are connected to every unit-cell (four in the case of tetragonal and six in the case of hexagonal). This is relevant, because hexagonal unit-cells can be depicted as tetragonal unit-cells. Often this is done for ease of modelling, as a tetragonal unit-cell can be tesselated in two directions to get a rectangluar plate. By keeping in mind that the original unit-cell is hexagonal, oversights about the symmetry properties of the unit-cell can be prevented.

2.2.3. Relevant plate theory

In the analysed literature, multiple aspects of plate and beam theory are used. Plate and beam theory can be applied both to the behaviour of the metaplate as a whole, and to the behaviour of the flexures inside the unit-cells of the metaplate. In the design process to turn a rigid body model into a compliant mechanism, thin flexures are often used to replace rigid joints. Metaplate unit-cells, which are compliant mechanism themselves are therefore often based on thin-walled structures. For small thicknesses of flexures, Euler-Bernoulli beam theory could be used, which Yao et al. apply in their paper[5].

When working with plates where the length and width are much greater than the thickness, plate theory might be desired to simplify calculations. For thin plates Kirchhoff-Love i.e. classical plate theory can be used. This is a two-dimensional version of Euler-Bernoulli i.e. classical beam theory, where some effects of thickness in the plate are neglected. In Kirchhoff-Love plate theory shear deformations and stress in the thickness direction are neglected, also it is assumed that parallel lines before deformation remain parallel after deformation. As plates become thicker, the shear deformation becomes more important. So for thick plates Reissner-Mindlin plate theory should be used, which is an extension of Kirchhoff-Love theory that does not neglect the shear deformation in the plate. For all of the previously mentioned plate theories, the material is assumed to be a Cauchy continuum i.e. classical continuum. About this Steinberg and Kvasov state: “The Classical Theory of Elasticity is based on the idealized model of elastic continuum, where the body forces acting on the surface element are described by the force vector. This assumption leads to the introduction of the symmetric stress and strain tensors.”[24].

In literature, metaplates are often modelled as plates using plate theory. This started with La Magna et al.[13] and Evans et al.[17] who modelled (re-entrant) honeycomb lattices as Kirchhoff-Love plates. More recently Reissner-Mindlin plate theory has also been applied to metaplates by Mirzaali et al.[6] and Steinberg and Kvasov[24] who actually used a variation of Reissner Mindlin based on a Cosserat continuum. The Cosserat continuum is further elaborated upon in subsection 2.3.3.

2.3. State of the art

In the previous subsection, Poisson’s ratio, its relation to bending-induced curvature and metamaterials were discussed. Now the interaction between these concepts, namely the bending-induced double curvature of metaplates, which is the main focus of this literature review, is presented in subsection 2.3.1 and subsection 2.3.2. Some important concepts from the state of the art will be further explained in subsection 2.3.3 and subsection 2.3.4.

2.3.1. Bending-induced double curvature in literature

As mentioned previously, the bending-induced double curvature of (re-entrant) honeycomb metaplates seems in-line with continuous plates based on the found literature. For three different Poisson's ratios the bending-induced double curvature is shown in Figure 2.6. Here, it can be seen that the type of double curvature depends on the Poisson's ratio of the metaplate.

However, in other literature results are presented that do not coincide with the previous conclusion where the double curvature of a metaplate simply depends on the Poisson's ratio of the metaplate. Yao et al. stated that the bending-induced double curvature of a metaplate is not defined by Poisson's ratio, but rather by the "competitive interaction between axial torision and out-of-plane bending"[5]. This observation is actually quite logical when looking at the unit-cell geometry up close, because a unit-cell is more than simply its designed Poisson's ratio. Inconsistencies were observed when unit-cells other than the (re-entrant) honeycomb were considered. Alderson et al. analysed various chiral and anti-chiral metaplates[22]. The anti-tri-chiral metaplate, which can be seen in Figure 2.8, is of special interest here. Alderson et al.[22] hypothesized the bending-induced curvature of an anti-tri-chiral metaplate to be synclastic, which is in accordance with continuous plate theory for a negative Poisson's ratio. When the bending-induced curvature turned out to be anticlastic, Alderson et al. stated: "Since the cylinder rotation mechanism is, then, redundant for out of-plane bending, the in-plane Poisson's ratio of the system will tend towards that given by Eq. (4) [i.e.$\nu_{xy} = \nu_{yx} -> +1$] and hence the predicted anticlastic curvature"[22]. This is an example of a metaplate where the Poisson's ratio does not determine the bending-induced double curvature, so continuous plate theory can not be applied. More examples like this can be found like [19][20] where the usage of plate theory also does not accurately describe the behaviour of metaplates. Mirzaali et al.[6] analysed (re-entrant) honeycomb metaplates using FEA and found that the thickness of the metaplate influences the bending-induced double curvature, while changing the thickness does not change the in-plane Poisson's ratio. The results of this can be seen in Figure 2.8.

As mentioned previously, metaplates are a special type of architected plates. The methods of modelling architected plates and metaplates are often similar, as the internal mechanisms overlap greatly. Strictly speaking, a honeycomb plate is an architected plate and a re-entrant honeycomb plate is an architected plate and also a metaplate, as this re-entrant honeycomb plate has a negative Poisson's ratio. If the bending-induced double curvature of metaplates depends on more than just the Poisson's ratio, then architected plates in general might also display different kinds of double curvature. If an architected plate with a positive Poisson's ratio displays synclastic bending-induced double curvature, which is associated with a negative Poisson's ratio for continuous plates, then it could be argued that this architected plate could be considered as a metaplate. Therefore, literature about architected plates/cellular solids was looked into for this literature review[25][26][27][28][29]. Shrimali et al. used homogenisation for architected plates to compare the bending of these architected plates to the bending of continuous plates[29]. In the research of Fongsamootr et al.[28] bending experiments were performed on an architected plates and compared to continuous plates. In both these papers no observations about double curvature were made. Fongsamootr et al. used a three-point bending test for its experiments, which could have suppressed the double curvature. This alludes to the general problem of experimentally evaluating pure bending conditions.

Experimental validation is a complex procedure. Both applying a pure moment on a plate and measuring the displacement of a large number of points in three dimensions are difficult to perform. Therefore,

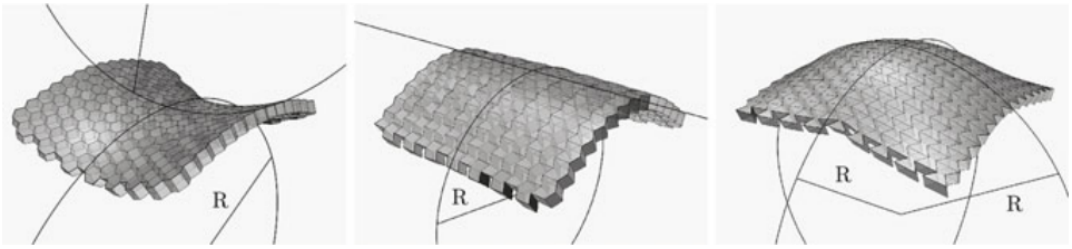

Figure 2.6: Bending-induced double curvature of honeycomb plates with positive, (near) zero and negative Poisson's ratio from left to right[13]

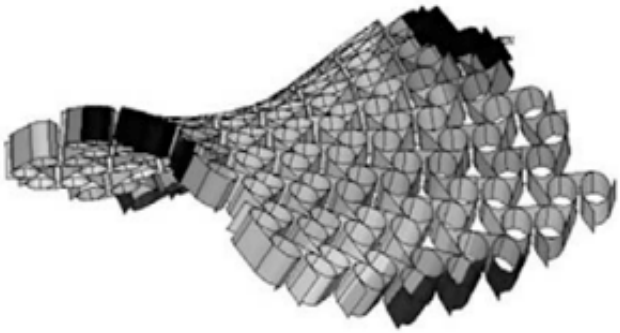

Figure 2.7: Double curvature of an auxetic anti-tri-chiral metaplate[22], the observed curvature is anticlastic

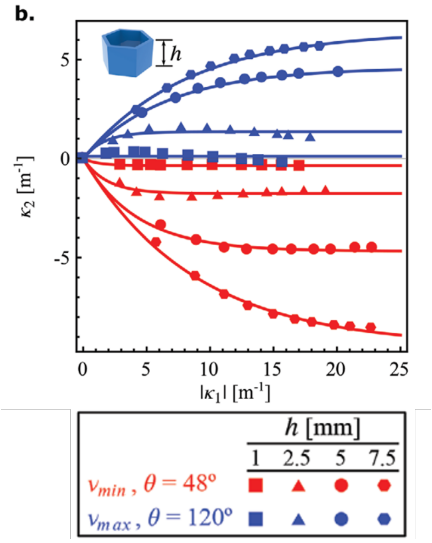

Figure 2.8: Relation between height of the unit-cell and the bending-induced double curvature[6]

Yao et al. simplified this by only validating if the type of double curvature is correct[5]. This could be a useful method, but the possible conclusions from the validation are restricted to: anticlastic bending, roughly cylindrical bending or synclastic bending. To validate the bending behaviour more precisely would require a setup like Mirzaali et al.[6] or Eskandari et al.[7] used. Caution should be taken, when comparing different experimental setups found in literature, because the results of testing could be influenced by the testing method. In the case of metaplates it is important to critically compare the connection method of the metaplate to the test setup. Mirzaali et al. restricted the bending at two sides of the plates, this resulted in a reduced amount of double curvature. In the case of Fongsamootr et al.[28], additionally the bending at the center of the architected plate was also reduced as a line contact only applies force when in contact. Eskandari et al. did not restrict this, but the bending is achieved though applying a force not a moment.

2.3.2. Bending Poisson's ratio

From subsection 2.3.1 it can be concluded that modelling a metaplate as a continuous plate is not always valid, when looking at bending-induced double curvature. Alderson et al.[22] stated that it seemed like the anti-tri-chiral metaplate had a negative Poisson's ratio in-plane and a positive Poisson's ratio for bending out-of-plane. Eskandari et al.[7] and Yao et al.[5] followed up on this idea by splitting the Poisson's ratio into two parameters, the in-plane Poisson's ratio (IPR) and the bending Poisson's ratio (BPR). This is in addition to the material Poisson's ratio (MPR) mentioned previously. Eskandari et al. named the BPR Mindlin's ratio. For this literature study BPR was chosen as a more intuitive name, because it describes the Poisson's ratio for bending-induced double curvature. This means that the bending-induced double curvature can be expressed by the BPR, where negative coincides with synclastic curvature, zero with monoclastic curvature and positive with anticlastic curvature. Distinguishing these two terms meant that Equation 2.1 can no longer be assumed to be automatically correct for metaplates. Equation 2.1 can be split up into two separate equations:

$$IPR = -\frac{\epsilon_{11}}{\epsilon_{22}} \quad \text{and} \quad BPR = -\frac{\kappa_{11}}{\kappa_{22}} \tag{2.2}$$

Eskandari et al. and Yao et al. then analysed different types of metaplates for varying parameters. This revealed how different parameters influenced the IPR and the BPR or both. Yao et al. varied the angle, relative thickness, and loading direction for two different achiral unit-cell designs[5]. Eskandari et al. varied the relative thickness for a variety of achiral and chiral unit-cells at constant IPR[7].

In Figure 2.9 an important graph made by Eskandari et al.[7] is shown. The graph shows how for a fixed IPR, the BPR can vary greatly depending on the relative thickness. Three types of double curvature are shown, which correspond to the previously mentioned double curvatures from Figure 2.2. In Figure 2.9 the difference between synclastic and one-way i.e. monoclastic curvature might seem small, but they do depict different types of double curvature. The data points were generated through 2D-AAH, a homogenisation method constructed by Eskandari et al.[7]. Here, the relative thickness is the metaplate thickness divided by a length element of the unit-cell. This length element is somewhat arbitrarily chosen per unit-cell, but this should not matter for the results. The length element is just one way of representing the in-plane size of a unit-cell.

The graph shows the BPR for increasingly thick unit-cells, for a fixed unit-cell size in-plane and IPR. For the (re-entrant) honeycomb unit-cell it can be seen that the BPR converges to the IPR for greater values of relative thickness. The star-shaped unit-cell and a chiral unit-cell can have both a positive or negative BPR based on the relative thickness. Eskandari et al. state: “Notably, as the relative thickness of the plate approaches infinity, Mindlin’s ratio [which is referred to as BPR in this literature review] tends to Poisson’s ratio, indicating a size depency in CSPT”[7], but in the range presented only the (re-entrant) honeycomb can be confirmed to converge. Similar behaviour of the (re-entrant) honeycomb was also observed by Mirzaali et al. in Figure 2.8[6]. This dependency on relative thickness was not taken into consideration in previous works, because only at small relative thicknesses does the size dependency become significant. Therefore, older works[13][17] could correctly predict the bending-induced curvature of (re-entrant) honeycombs without taking this size dependency into account. In Figure 2.9 it can also be seen that two tetrachiral unit-cells display different IPR and BPR due to how the unit-cell is rotated compared to the direction of induced bending. About the orientation of the tetra-chiral unit-cells Eskandari wrote: “Figure 4a [Figure 2.9] presents the variation of Mindlin’s ratio [or BPR] for each principle orientation versus the relative thickness. It is noteworthy that the principal directions differ at each relative thickness”[7]. Eskandari states that the BPR is given by Equation 2.3[7].

$$\zeta = \frac{\gamma - \eta_b'}{\eta_b' + \gamma} \tag{2.3}$$

Here ζ is the BPR, “η_b and γ are torsional, anticlastic (symmetric) bending, and synclastic (anti-symmetric) bending moduli, respectively”[7]. Equation 2.3 can be solved by using the results of the 2D-AAH. In subsection 2.3.4 this is handled in more detail.

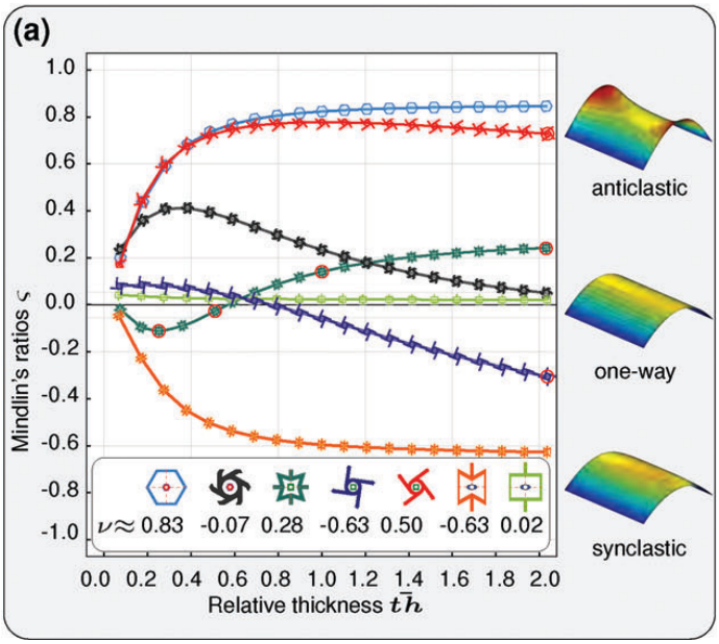

Figure 2.9: BPR for increasing relative thickness, for a fixed IPR[7]

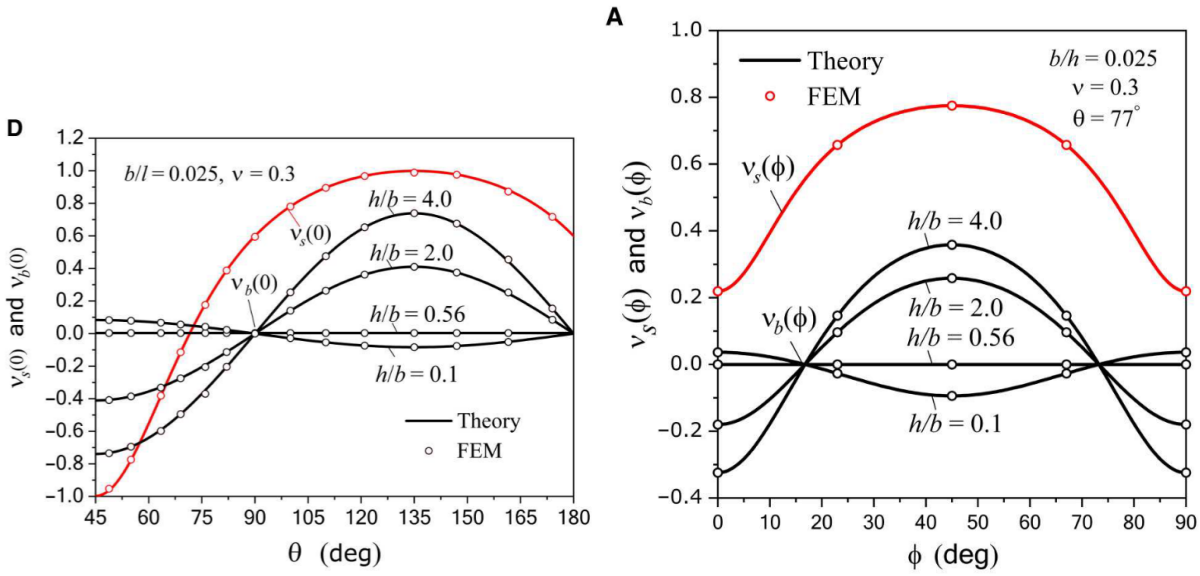

Figure 2.10: BPR and IPR for different relative thicknesses, left varying internal angle, right varying load angle[5]

In Figure 2.10 two graphs about (tetragonal) star shaped metaplates made by Yao et al.[5] are shown. Here θ represents the angle between the flexures in the unit-cell, while ϕ represents the angle in which the bending is applied. In both graphs red lines indicate the IPR an black lines indicate the BPR. While the graphs look different from Figure 2.9, a similar size dependency is visualised by the black lines that represent relative thicknesses. By looking at a certain angle, $\theta = 135°$ for instance, it can be seen that there are four values of BPR possible. These four BPR values all correspond to the same IPR value, which is the point on the red line at $\theta = 135°$. The relative thickness is the thickness of the metaplate divided by the width of the flexures. This could also be expressed as the thickness of the metaplate divided by a length element (which in this case is the flexure length), because the width and length of the flexures have a fixed relation $b/l = 0.025$. So Figure 2.9 and Figure 2.10 present the same relatation, where different BPR values can be attained for one IPR value. In addition to the size dependency, the influence of θ (left graph) and ϕ (right graph) on both the IPR and BPR are also given. This reveals the interesting behaviour that the size dependency is not constant for different angles, even disappearing for $\theta = 90°$. For certain angles like $\theta = 135°$ and $\phi = 45°$ it seems like the IPR and BPR start to tend towards each other just as was observed in Figure 2.9. However, this expected behaviour can not be concluded from the paper itself and was not claimed by Yao et al.

Yao et al. derived the formulas for both the IPR and BPR of the (tegragonal) star shaped metaplate, and presented these in the paper[5]. The bending Poisson ratio of a (tetragonal) star shaped metaplate is:

$$\nu_b(0) = \frac{\lambda - 1}{3\lambda + 1} \sin(2\theta) \tag{2.4}$$

where λ is the torsion to bending stiffness ratio. The first 1000 terms are used, given by:

$$\lambda = \frac{6b^2}{(1+\nu)}\left(\frac{1}{3} - \frac{64b}{\pi^5 h}\sum \frac{1}{n^5}\tanh\left(\frac{n\pi h}{2b}\right)\right) \tag{2.5}$$

The direction of the bending-induced curvature can be added to this formula through ϕ. The BPR as a function of ϕ is:

$$\nu(\phi) = \frac{(\lambda - 1)[f^2(\theta)\cos^2(2\phi) - 1]}{3\lambda + 1 - (\lambda - 1)f^2(\theta)\sin^2(2\phi)} \tag{2.6}$$

These formulas were constructed by using a Cosserat continuum model, because like mentioned previously continuous (Cauchy) plate theory will always state that $IPR = BPR$. The star shaped metaplate is therefore modelled as a Cosserat plate, where the deformation of the beams is used to express the IPR and from that the BPR was determined. The Cosserat continuum model has a size dependency,

which Eskandari[7] also mentioned as important for his 2D-AAH model. Euler-Bernoulli beam theory is used for the flexures inside the unit-cell, as the flexures are slender[5]. The relation between the length and width of the flexures (b/l) is fixed to ensure the validity of Euler-Bernoulli beam theory. In section subsection 2.3.3, Cosserat theory is handled in more detail.

2.3.3. Cosserat theory and Couple-Stress Plate Theory (CSPT)

In a Cauchy continuum or in other words a classical continuum, two material moduli are required to model the material if the model is isotropic. This is an idealisation that can often be applied to engineering materials as the imperfections present in the material average out and the observed properties are isotropic. However, if the material is non-isotropic, more than two material moduli are required to model the material. In areas like this literature review about metamaterials, but also subjects like sandwich structures, reinforced concrete and more, a size dependency should also be taken into consideration. Small features are present in these structures and based on the size of these features relative to the size of the structure, the behaviour of the structure might be significantly different. This size dependency cannot be taken into consideration in a Cauchy continuum model and therefore other approaches are of interest that are able to take these size dependencies into consideration. If a size dependency is present in a material, additional material moduli are required to correctly model the behaviour. Also a model is required that is able to use these additional material moduli, to make an accurate representation of the material.

The methods used by Yao et al.[5] and Eskandari et al.[7] are different, as Yao et al. use a Cosserat continuum and Eskandari et al. use Couple-Stress Plate Theory (CSPT). However, in both papers the same shortcoming of earlier research is identified, being the use of a Cauchy continuum. Both Cosserat theory and CSPT can be viewed as extensions to a Cauchy continuum model, that are able to take microstructure into consideration[5][7]. In the context of metaplates this size dependency relates to the size of the unit-cells relative to the size of the metaplate. In other words, for a fixed plate shape how many unit-cells the metaplate is comprised of. Here it is important to note that the thickness i.e. height of the unit-cell is always identical to that of the metaplate, as the tesselation only happens in the length and width direction. This relation could also be represented by varying the height of a metaplate, for a fixed surface area. In earlier research, Mirzaali et al.[6] already showed through FEA that increasing the height of a unit-cell could influence the amount of bending-induced curvature. Both Yao et al.[5] and Eskandari et al.[7] showed this relation with their methods as well. It is important to note that changing the height of the metaplate for a fixed surface area could influence the validity of (thin) plate theory.

It is theorised that a Cosserat continuum will converge to a Cauchy continuum when the size of the microstructure becomes negligibly small[7][24][30]. Steinberg and Ksavov. stated: “As the Cosserat Elasticity parameters tend to zero the solution of the Cosserat plate was shown to converge to the Mindlin-Reissner plate. This implies that the Cosserat Plate Theory is a generalization of the classic Mindlin Reissner Plate Theory”[24]. In research about architected plates Shrimali et al. analysed the convergence of perforated plates to continuous plates for varying heights and unit-cells sizes. From the research it was concluded that: “thin perforated plates can be effectively modeled as 2D structures made of a homogeneous elastic material already when their thicknesses and hole sizes are only 4-to −5 times smaller than their in-plane dimensions”[29]. This indicates a size dependency that might be similar to the size dependency mentioned by Steinberg and Ksavov.

A paper about applying a Cosserat continuum to model cylindrical rods in COMSOL was found, including a tutorial on how to set this up[30]. This research used six material moduli to represent the isotropic elastic material behaviour. The obtained stress and strain tensors were both not symmetric and the microrotation term was part of the strain tensor[30]. The research also explicitly mentions that a Cosserat continuum was used to take “size effects” into consideration[30]. Research about the computation of Cosserat continua for two dimensional geometries was also found in literature[31].

2.3.4. Homogenisation

Homogenisation can be used as a method to model a heterogeneous material as an equivalent homogeneous material[32]. In the case of metamaterials and other architected materials that have a repeating pattern, a respective volume element (RVE) is selected and solved for. This homogenised result can then be extrapolated to the entire material. On the RVE, load cases can be applied to determine the

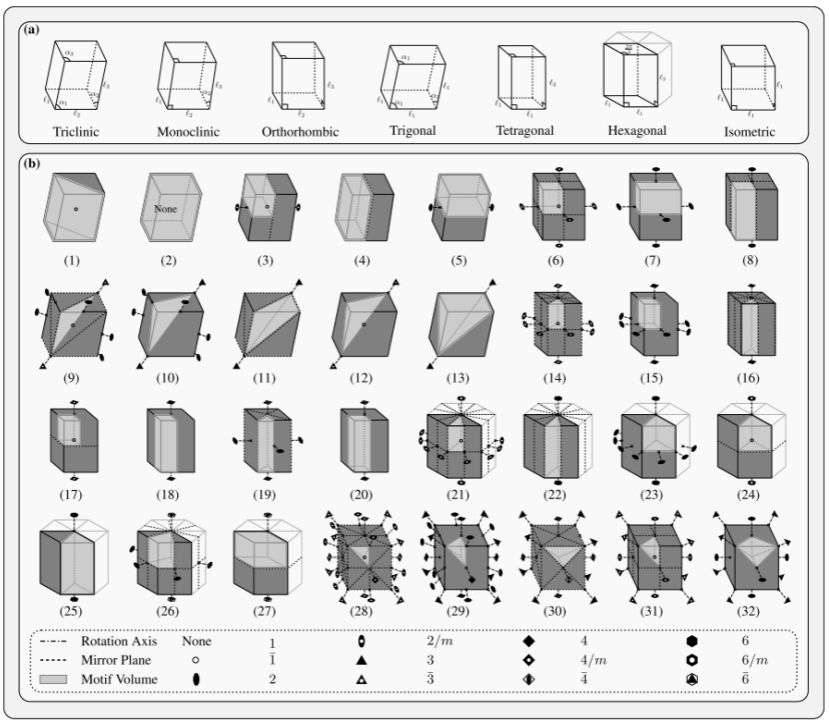

Figure 2.11: The 32 crystal classes used by Eskandari et al.[7]

equivalent material moduli, i.e. the required parameters to accurately model the behaviour of the RVE. The RVE could be chosen as the unit-cell of the metamaterial. By also analysing larger RVE's it can be checked if correct boundary conditions are applied, as different sizes of RVE should return the same equivalent material moduli. If a small error is present in the unit-cell or in one of the load cases, then this error will be extrapolated to the entire material. Also like mentioned in subsection 2.2.2, unit-cells can be depicted in multiple ways. Eskandari et al.[7] converts his unit-cells to cuboid RVE's, which makes the procedure of applying the load cases more generalised.

Using homogenisation on its own to obtain a continuous plate approximation of metaplate has been attempted[33]. Here it was observed that a continuum limit is present where homogenisation is accurate due to a size dependency, which has already been mentioned in subsection 2.3.3 as an important factor of analysing metamaterials. Therefore Eskandari et al. used homogenisation as a part of their 2D-AAH that is able to take this size dependency into account[7].

The process that Eskandari et al. used to obtain their models is quite elaborate so in this section a few aspects of this process are discussed. Because this method could be a promising tool to analyse metaplates, some further research was done into homogenisation in general[34] [32] [29][35][33]. Eskandari et al. presented an augmented asymptotic homogenization method (AAH)[7]. Eskandari et al. also presented three-, two-, and one-dimensional couple-stress theories that use this AAH[7].

For research regarding metaplates the 2D-AAH is relevant in combination with the couple-stress plate theory (CSPT). In subsection 2.3.3 it was mentioned that the amount of required equivalent material moduli depends on the degree of isotropy and the presence of a size dependency. By evaluating the crystal class of the unit-cell of interest, the required number of equivalent material moduli can be determined to accurately model the metaplate[7]. An image containing the crystal classes used by Eskandari et al. can be seen in Figure 2.11.

For instance, a honeycomb unit-cell, which has a hexagonal crystal class can be classified as number 21 in Figure 2.11[7]. Equation 2.3 can be expressed in terms of the general elasticity tensor. Five material parameters are required for the honeycomb unit-cell[7]. The formula for the BPR of a honeycomb unit-cell becomes:

$$\zeta = \frac{2D_{44} - 3D_{11} + 3\frac{B_{11}}{C_{11}-C_{12}}}{2D_{44} - 3\frac{B_{11}}{C_{11}C_{12}}} \tag{2.7}$$

Here $B, C, D's$ are entries from the homogenised material properties tensor, which was determined by the 2D-AAH[7]. This formula can then be used to calculate the BPR, which defined as ζ by Eskandari et al.[7]. By using the framework laid out by Eskandari et al., other unit-cells could also be analysed in a similar way. The results of the 2D-AAH were visualised by Eskandari et al., which can be seen in Figure 2.12. Going into more detail about the 2D-AAH process would lengthen this literature review significantly. Therefore it is presumed that for additional information about this process, the paper of Eskandari et al.[7] and its supporting material themselves are consulted.

An anti-tri-chiral unit-cell should correspond to the ditrigonal-dipyramidal ($\bar{6}m2$). There is a great dependence on the direction of the load so more material moduli are required than the honeycomb. As the relative cylinder size compared to the flexure length of the anti-tri-chiral unit-cell becomes smaller. The unit-cell will start to look more like a honeycomb. Therefore the additional required material moduli should have a dependence on this relation. Eskandari et al.'s research does not include information about this symmetry type, only calculations for the symmetry types used by Eskandari et al[7] are presented.

The tetragonal star-shaped unit-cell requires seven material parameters[7]. Yao et al. state that the tetragonal star-shaped unit-cell is transversely isotropic[5]. The other unit-cells analysed by Eskandari et al. require nine material parameters[7].

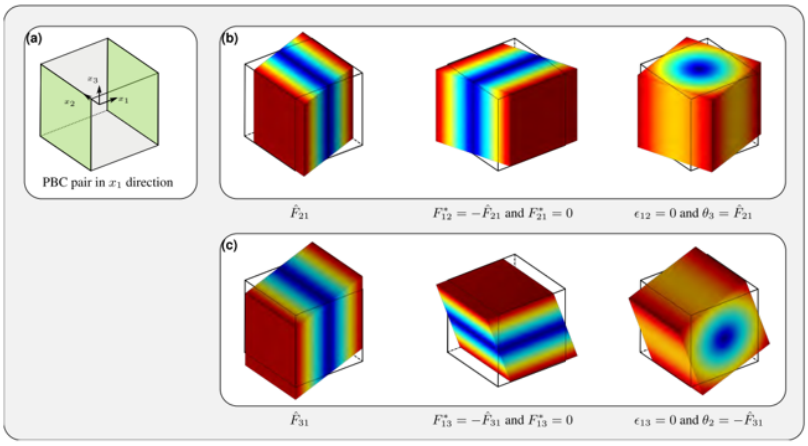

Figure 2.12: Homogenised continuum used by Eskandari et al.[7]

3

Discussion

In the introduction two main questions of interest were stated. The first question was:

Is it possible to model current metaplates as continuous plates? If not in general, are there conditions for which this could be possible?

A criterion that could be used to answer this question for a Cauchy continuum, is how similar the IPR and BPR are. This means that the IPR would determine the bending-induced curvature. If $IPR \approx BPR$, then the previously mentioned relation for the Poisson's ratio in Equation 2.1 holds for these metaplates. Based on the literature this is shown to be the case for a few unit-cell designs, specifically honeycombs and re-entrant honeycombs [13][17][6][7]. In Figure 2.9 from Eskandari et al.[7] it was shown that for these designs the BPR quickly converges to the IPR, which explains why earlier papers that did not differentiate between IPR and BPR were still able to design for specified curvatures in their metaplates. For the star-shaped unit-cell there are a few specific values of relative thickness and angle where the BPR also starts to approach the IPR, which can be seen in Figure 2.10[5]. For other unit-cell designs there seems to be a trend where as the relative thickness increases, the difference between the BPR and IPR decreases. Theoretically it is assumed that as the relative thickness increases i.e. the unit-cells become smaller relative to the plate size, that the BPR will converge to the IPR[7][24]. However, this has not been validated.

Eskandari et al.[7] and Yao et al.[5] have shown that by that by using a size dependent continuum, like a Cosserat continuum or a continuum based on the 2D-AAH results, it is possible to model metaplates as continuous plates. However, the amount of unit-cells that have been analysed using these methods is limited.

Another criterion of importance is the understanding of the underlying mechanisms of the metaplate. The interaction of bending stiffness and torsional stiffness is captured in the relative thickness, and therefore it is suspected that this parameter is influential for the BPR. Changing the internal angles of the unit-cell of a metaplate also influences the BPR, but this also changes the IPR [5]. Another property that is highly likely to influence the BPR is the length relative to the width of the flexures. No literature was found that analysed this relation for the bending of metaplates. However similar research was found about perforated plates [29]. This property is of interest for miniturisation purposes, as the size of the unit-cell will often be determined by the thinnest detail a machine is able to produce. So when the minimum thickness is reached, the relative length to width ratio determines how many unit-cells fit in a metaplate. This relation also influences if thin-walled approximations are valid, becoming less valid as the relative length to thickness becomes smaller[5]. The IPR is also suspected to be influenced by varying this relation, as the flexures in the unit-cell will start to look more like thick beams rather than thin flexures for lower values of relative length to thickness. Another parameter of interest is the direction in which the bending is applied. This has been done for the star-shaped unit-cell and for some chiral unit-cells [5] [7]. The star-shaped unit-cell at $\theta = 77^\circ$ had a positive IPR in all directions of applied load. However, the BPR switches from negative to positive. At roughly $\phi = 17^\circ$ the BPR becomes zero

and at $\phi = 45^\circ$ the BPR has the greatest positive value Figure 2.10. Additional knowledge about these underlying mechanisms could be crucial for constructing an accurate model.

The second question of interest, mentioned in the introduction was:

What types and amounts of double curvature are currently obtainable using metaplates?

The type and amount of double curvature can be expressed by the Bending Poisson's ratio (BPR) found in literature[5][7]. Here a positive BPR indicates anticlastic curvature and a negative BPR indicates synclastic curvature. From literature it can be concluded that while the IPR and BPR are related, it is possible to obtain synclastic and anticlastic curvature for both positive and negative IPR, by varying relative thickness, internal angles, load angles and type of unit-cells[5][7]. By using Cosserat theory or Couple Stress Plate Theory (CSPT) that regard the unit-cell geometry and are size-dependent, it should be possible to accurately predict the type of double curvature for metaplates.

The recent discovery that the IPR does not define the type of double curvature for metaplates, opens up a lot of new possibilities. One of these is for the application of shape-fitting. Previously, in research regarding shape-fitting the focus was on varying the Poisson ratio to achieve complex shapes[2]. With the new method as presented by [5][7], varying other parameters like thickness, height, internal angles and unit-cell type could be used as additional tools for shape-fitting.

In addition to the two questions from the introduction, another question of interest is:

Based on literature, what kind of follow-up research would be relevant?

By looking at the obtained results from Yao et al.[5] and Eskandari et al.[7] and expanding these findings by repeating the process for other potentially interesting unit-cells, the overview of the state of the art of possible BPR values in metaplates could be expanded.

The amount of research into the bending-induced curvature differs greatly per unit-cell design, so further research into lesser analysed unit-cells could give the most interesting and novel results. The (re-entrant) honeycomb unit-cell seems to be well explained by Mirzaali et al.[6] and Eskandari et al.[7] in combination with earlier papers that already achieved specified double curvatures by varying the Poisson's ratio. The IPR and BPR of the star shaped unit-cell have been described by both Yao et al.[5] and Eskandari et al.[7] Research into the bending of arrow unit-cells was limited, but due to the similar deformation mechanics to the re-entrant honeycomb and star shape, it is suspected that further research might not uncover novel insights. Chiral unit-cells were already analysed by Eskandari et al.[7], but this was limited to hexa-chiral and tetra-chiral unit-cells. Analysis on tri-chiral unit-cells and anti-chiral unit-cells has been done by Alderson[22], but without the distinction between IPR and BPR and a size dependent model. Only specified geometries were analysed, without varying parameters. Therefore, these could be interesting unit-cells to do further research on. The anti-tri-chiral unit-cell is of particular interest because of its symmetry and range of possible IPR values.

Also, Additional research is required to find out to which extend the BPR approaches the IPR for increasing relative thickness, which Eskandari et al.[7] already alluded to. This could have the practical application that it could be used as a condition in which the BPR could be ignored, similar to a continuum limit mentioned by Ariza et al.[33].

To correctly model the behaviour of metaplates (parts of) asymptotic homogenisation in combination with Cosserat continuum could be used. The goal in mind is to be able to model metaplates as continuous plates. Multiple types of plate theories could be used depending on the type of plate, but in literature a Cauchy continuum is often used for these plate theories. Based on Eskandari et al.[7] and Yao et al.[5] the reason that theoretical and experimental or FEA results for bending-induced double curvature sometimes do not coincide, is the usage of Cauchy continuum which does not account for couples that could be present in the material. By taking these couples into consideration a continuum material/plate could be made that correctly models the behaviour of metaplates. Eskandari et al. proposed a novel couple-stress theory to implement these couples into a Cauchy continuum[7], while Yao et al. used a Cosserat continuum to achieve the same effect[5].

For a proposed study a Cosserat continuum could be used as to keep the methodology as generic as possible. Using a Cosserat continuum to model materials with a non-negligible microstructure has

been widely used in literature. For in-plane metamaterials some literature exists mainly about chiral metamaterials. For the bending of metaplates, Yao et al.[5] were the only ones that applied this.

To accurately model metaplates as continuous Cosserat plates, information about the metaplate unit-cell is required. Yao et al.[5] solved this analytically by calculating the required information based on the geometry consisting of thin-walled beams. To acquire the relevant information homogenisation could also be (partially) used like Eskandari et al. did. Of interest in particular are so called load cases where a respective volume element (RVE, unit-cell or small metaplate) is loaded in a few specific ways, and from this the required information can be obtained that as stated previously is needed to characterise the continuous Cosserat plate. For this research, considering load cases was seen as the more viable option to allow for more different types of unit-cells and to not have to consider the validity of thin-walled approximations of the flexures in the unit-cells.

Homogenisation methods combined with Cosserat plate theory could be applied to create a similar model to Eskandari et al.[7], with which the behaviour and BPR of metaplates can be evaluated. The application of Cosserat theory in COMSOL has been found in the literature[30]. This could be expanded upon by modelling Cosserat plates in COMSOL.

Metaplates could also be analysed with FEA, where parameters of interest could be varied to evaluate if this influences the double curvature of the metaplate in the predicted way. Regions of intrest could also be looked for so a geometry can be selected where the metaplate is predicted to switch between synclastic and anticlastic curvature. Experimentally testing the double curvature of metaplates is quite complex. Both applying a pure bending moment on the metaplate and accurately measuring the resulting curvature are hard to integrate in a experimental setup [5]. Creating an proper test-setup for this would be a study on its own, so validating precise BPR values experimentally will be outside the scope of this study. Prototypes could be made as reference models, which could be used to validate if the type of double curvature seems correct.

4

Conclusion

In this literature review, an overview has been given of the state of the art regarding the bending-induced double curvature of negative Poisson's ratio metamaterial-plates. While the in-plane Poisson's ratio of these metaplates is well understood, research about their bending-induced double curvature still has a lot of unexplored areas, in which further research could be done. A widely used method of modelling metaplates as Cauchy continuous plates was found to only be accurate for specific conditions. Because of this, the assumption that the in-plane Poisson's ratio could be utilised to determine the bending-induced curvature is no longer valid.

Recent studies have made great progress by analysing the bending-induced double curvature of metaplates for varying parameters, like Mirzaali et al.[6], Eskandari et al.[7] and Yao et al.[5]. This knowledge can be expanded upon by doing similar research on different types of unit-cells. This would entail analysis of the geometry, the usage of homogenisation techniques/FEA (which should be able to include a size-dependency [7][5]), and using Cosserat (plate) theory to model the metaplates. The results of this research could introduce novel insights about metaplates, as the discrepancy between the in-plane Poisson's ratio and bending-induced double curvature itself became apparent through the research into different unit-cell designs for metaplates.

Based on observations from literature and assessment based on literature, using Cosserat plate theory in combination with homogenisation and doing further research about the bending-induced curvature of specifically anti-chiral metaplates could reveal new insights and expand the existing knowledge regarding the bending of metaplates.

References

[1] K. Bertoldi, V. Vitelli, J. Christensen, and M. V. Hecke, "Flexible mechanical metamaterials," *Nature Reviews Materials 2017 2:11*, vol. 2, pp. 1–11, 11 Oct. 2017, ISSN: 2058-8437. DOI: 10.1038/natrevmats.2017.66. [Online]. Available: https://www.nature.com/articles/natrevmats201766.

[2] A. M. J. V. Soest, "Analyzing out-of-plane deformations caused by varying poisson ratio distributions in a metamaterial," M.S. thesis, Delft University of Technology, 2023. [Online]. Available: http://repository.tudelft.nl/..

[3] C. Qi, F. Jiang, and S. Yang, "Advanced honeycomb designs for improving mechanical properties: A review," *Composites Part B: Engineering*, vol. 227, p. 109 393, Dec. 2021, ISSN: 13598368. DOI: 10.1016/j.compositesb.2021.109393.

[4] A. A. Zadpoor, M. J. Mirzaali, L. Valdevit, and J. B. Hopkins, "Design, material, function, and fabrication of metamaterials," *APL Materials*, vol. 11, p. 020 401, 2 Feb. 2023, ISSN: 2166532X. DOI: 10.1063/5.0144454.

[5] Y. Yao, Y. Ni, and L. He, "Unexpected bending behavior of architected 2d lattice materials," *Science Advances*, vol. 9, 25 2023, ISSN: 23752548. DOI: 10.1126/SCIADV.ADG3499/SUPPL_FILE/SCIADV.ADG3499_SM.PDF. [Online]. Available: https://www.science.org/doi/10.1126/sciadv.adg3499.

[6] M. J. Mirzaali, A. Ghorbani, K. Nakatani, *et al.*, "Curvature induced by deflection in thick metaplates," *Advanced Materials*, vol. 33, 30 Jul. 2021, ISSN: 15214095. DOI: 10.1002/adma.202008082.

[7] S. Eskandari, B. shahryari, and A. Akbarzadeh, "Unravelling size-dependent and coupled properties in mechanical metamaterials: A couple-stress theory perspective," *Advanced Science*, vol. 11, p. 2 305 113, 13 Apr. 2024, ISSN: 2198-3844. DOI: 10.1002/ADVS.202305113. [Online]. Available: https://onlinelibrary.wiley.com/doi/full/10.1002/advs.202305113%20https://onlinelibrary.wiley.com/doi/abs/10.1002/advs.202305113%20https://onlinelibrary.wiley.com/doi/10.1002/advs.202305113.

[8] P. Roberjot and J. L. Herder, "A unified design method for 2d auxetic metamaterials based on a minimal auxetic structure," *International Journal of Solids and Structures*, vol. 295, p. 112 777, Jun. 2024, ISSN: 0020-7683. DOI: 10.1016/J.IJSOLSTR.2024.112777.

[9] W. W. P. J. V. D. Sande, "Analysis and synthesis of shell flexures," *Citation*, 2024. DOI: 10.4233/uuid:03dae8b4-4b3e-49af-8783-807882c62338.

[10] X. G. Zhang, W. Jiang, Y. Zhang, *et al.*, "Bending performance of 3d re-entrant and hexagonal metamaterials," *Thin-Walled Structures*, vol. 188, p. 110 829, Jul. 2023, ISSN: 0263-8231. DOI: 10.1016/J.TWS.2023.110829.

[11] A. Farzaneh, N. Pawar, C. M. Portela, and J. B. Hopkins, "Sequential metamaterials with alternating poisson's ratios," *Nature Communications*, vol. 13, 1 Dec. 2022, ISSN: 20411723. DOI: 10.1038/s41467-022-28696-9.

[12] F. Jiang, S. Yang, C. Qi, and H. T. Liu, "Two plateau characteristics of re-entrant auxetic honeycomb along concave direction," *Thin-Walled Structures*, vol. 179, p. 109 665, Oct. 2022, ISSN: 0263-8231. DOI: 10.1016/J.TWS.2022.109665.

[13] R. L. Magna and J. Knippers, "Tailoring the bending behaviour of material patterns for the induction of double curvature," *Humanizing Digital Reality*, pp. 441–452, 2018. DOI: 10.1007/978-981-10-6611-5_38.

[14] F. Jiang, S. Yang, C. Ding, and C. Qi, "Quasi-static crushing behavior of novel circular double arrowed auxetic honeycombs: Experimental test and numerical simulation," *Thin-Walled Structures*, vol. 177, p. 109 434, Aug. 2022, ISSN: 02638231. DOI: 10.1016/j.tws.2022.109434.

[15] J. N. Grima, R. Gatt, A. Alderson, and K. E. Evans, "On the potential of connected stars as auxetic systems," *Molecular Simulation*, 2005. DOI: 10.1080/08927020500401139. [Online]. Available: http://home.um.edu.mt/auxetic.

[16] L. Kai, C. Xiaofei, Z. Peng, W. WenWang, and L. Ying, "Dynamic mechanical performances of enhanced anti-tetra-chiral structure with rolled cross-section ligaments under impact loading," *International Journal of Impact Engineering*, vol. 166, p. 104 204, Aug. 2022, ISSN: 0734-743X. DOI: 10.1016/J.IJIMPENG.2022.104204.

[17] K. E. Evans, "The design of doubly curved sandwich panels with honeycomb cores," *Composite Structures*, vol. 17, pp. 95–111, 2 Jan. 1991, ISSN: 0263-8223. DOI: 10.1016/0263-8223(91)90064-6.

[18] Y. Sakai and M. Ohsaki, "Optimization method for shape design of auxetic bending-active gridshells using discrete differential geometry," *Structures*, vol. 34, pp. 1589–1602, Dec. 2021, ISSN: 2352-0124. DOI: 10.1016/J.ISTRUC.2021.08.067.

[19] D. H. Chen, "Bending deformation of honeycomb consisting of regular hexagonal cells," *Composite Structures*, vol. 93, pp. 736–746, 2 Jan. 2011, ISSN: 0263-8223. DOI: 10.1016/J.COMPSTRUCT.2010.08.006.

[20] D. H. Chen, "Equivalent flexural and torsional rigidity of hexagonal honeycomb," *Composite Structures*, vol. 93, pp. 1910–1917, 7 Jun. 2011, ISSN: 0263-8223. DOI: 10.1016/J.COMPSTRUCT.2011.02.009.

[21] J. Huang, Q. Zhang, F. Scarpa, Y. Liu, and J. Leng, "Bending and benchmark of zero poisson's ratio cellular structures," *Composite Structures*, vol. 152, pp. 729–736, Sep. 2016, ISSN: 0263-8223. DOI: 10.1016/J.COMPSTRUCT.2016.05.078.

[22] A. Alderson, K. L. Alderson, G. Chirima, N. Ravirala, and K. M. Zied, "The in-plane linear elastic constants and out-of-plane bending of 3-coordinated ligament and cylinder-ligament honeycombs," *Composites Science and Technology*, vol. 70, pp. 1034–1041, 7 Jul. 2010, ISSN: 0266-3538. DOI: 10.1016/J.COMPSCITECH.2009.07.010.

[23] D. Attard, P. S. Farrugia, R. Gatt, and J. N. Grima, "Starchirals–a novel class of auxetic hierarchal structures," *International Journal of Mechanical Sciences*, vol. 179, p. 105 631, Aug. 2020, ISSN: 0020-7403. DOI: 10.1016/J.IJMECSCI.2020.105631.

[24] L. Steinberg and R. Kvasov, *Cosserat Plate Theory*. CRC Press, 2023.

[25] C. Baek, A. O. Sageman-Furnas, M. K. Jawed, and P. M. Reis, "Form finding in elastic gridshells," *Proceedings of the National Academy of Sciences of the United States of America*, vol. 115, pp. 75–80, 1 Jan. 2018, ISSN: 10916490. DOI: 10.1073/PNAS.1713841115/SUPPL_FILE/PNAS.1713841115.SM05.MP4. [Online]. Available: https://www.pnas.org/doi/abs/10.1073/pnas.1713841115.

[26] R. S. Kumar and D. L. McDowell, "Generalized continuum modeling of 2-d periodic cellular solids," *International Journal of Solids and Structures*, vol. 41, pp. 7399–7422, 26 Dec. 2004, ISSN: 0020-7683. DOI: 10.1016/J.IJSOLSTR.2004.06.038.

[27] F. Zhang, F. Pan, and Y. Chen, "Revisiting the stiffness of lattice plates with micromechanics modeling," *Composite Structures*, vol. 286, p. 115 276, Apr. 2022, ISSN: 0263-8223. DOI: 10.1016/J.COMPSTRUCT.2022.115276.

[28] T. Fongsamootr, P. Suttakul, N. Tippayawong, P. Nanakorn, and C. Cappellini, "Bending behavior of 2d periodic plates with different unit cells: Numerical and experimental investigations," *Materials Today Communications*, vol. 31, p. 103 774, Jun. 2022, ISSN: 2352-4928. DOI: 10.1016/J.MTCOMM.2022.103774.

[29] B. Shrimali, M. Pezzulla, S. Poincloux, P. M. Reis, and O. Lopez-Pamies, "The remarkable bending properties of perforated plates," *Journal of the Mechanics and Physics of Solids*, vol. 154, p. 104 514, Sep. 2021, ISSN: 0022-5096. DOI: 10.1016/J.JMPS.2021.104514.

[30] J. Jeong, H. Ramezani, and E. Spéciale, *Implementation of the finite isotropic linear cosserat models based on the weak form*, 2008. [Online]. Available: http://www.ce.berkeley.edu/.

[31] E. Sharbati and R. Naghdabadi, "Computational aspects of the cosserat finite element analysis of localization phenomena," *Computational Materials Science*, vol. 38, pp. 303–315, 2 Dec. 2006, ISSN: 0927-0256. DOI: 10.1016/J.COMMATSCI.2006.03.003.

[32] A. L. Kalamkarov, I. V. Andrianov, and V. V. Danishevs'kyy, *Asymptotic homogenization of composite materials and structures*, May 2009. DOI: 10.1115/1.3090830.

[33] M. P. Ariza, S. Conti, and M. Ortiz, "Homogenization and continuum limit of mechanical metamaterials," *Mechanics of Materials*, vol. 196, p. 105 073, Sep. 2024, ISSN: 0167-6636. DOI: 10.1016/J.MECHMAT.2024.105073.

[34] S. Arabnejad and D. Pasini, “Mechanical properties of lattice materials via asymptotic homogenization and comparison with alternative homogenization methods,” *International Journal of Mechanical Sciences*, vol. 77, pp. 249–262, Dec. 2013, ISSN: 0020-7403. DOI: 10.1016/J.IJMECSCI.2013.10.003.

[35] S. P. Vasudevan and P. P. Pratapa, “Homogenization of non-rigid origami metamaterials as kirchhoff–love plates,” *International Journal of Solids and Structures*, vol. 300, p. 112 929, Aug. 2024, ISSN: 0020-7683. DOI: 10.1016/J.IJSOLSTR.2024.112929.